10-19-2015

Erosion Resistance of High Velocity Oxy-Fuel WC-Co-Cr Thermal Spray Coatings

Chris Imeson
University of Windsor

Erosion Resistance of High Velocity Oxy-Fuel WC-Co-Cr Thermal Spray Coatings

By

Chris Imeson

A Thesis

Submitted to Faculty of Graduate Studies through the

Department of Mechanical, Automotive and Materials Engineering

in Partial Fulfillment of the Requirements for

the Degree of Master of Applied Science at the

University of Windsor

Windsor, Ontario, Canada

Erosion Resistance of High Velocity Oxy-Fuel WC-Co-Cr Thermal Spray Coatings

By

Chris Imeson

APPROVED BY:

Dr. D. Green, Department Reader
Department of Mechanical, Automotive and Materials Engineering

---

Dr. J. Johrendt, Outside Program Reader
Department of Mechanical, Automotive and Materials Engineering

---

Dr. A. Edrisy, Advisor
Department of Mechanical, Automotive and Materials Engineering

September 18, 2015

Declaration of Co-Authorship

I hereby declare that this thesis incorporates material, which is an outcome of a joint venture undertaken in collaboration with Dennis Sheffer from SharkSkin Coatings and Surface Techniques ltd. and the University of Windsor's Department of Mechanical, Automotive and Materials Engineering, under the supervision of Dr. A. Edrisy. The collaboration is covered in Chapters 3, 4, and 5 of this thesis.

I am aware of the University of Windsor Senate Policy on Authorship and I certify that I have properly acknowledged the contribution of other researchers to my thesis, and have obtained written permission from each of the co-author(s) to include the above material(s) in my thesis.

I certify that, with the above qualification, this thesis, and the research to which it refers, is the product of my own work.

I declare that, to the best of my knowledge, my thesis does not infringe upon anyone's copyright nor violate any proprietary rights and that any ideas, techniques, quotations, or any other material from the work of other people included in my thesis, published or otherwise, are fully acknowledged in accordance with the standard referencing practices. Furthermore, to the extent that I have included copyrighted material that surpasses the bounds of fair dealing within the meaning of the Canada Copyright Act, I certify that I have obtained a written permission from the copyright owner(s) to include such material(s) in my thesis.

I declare that this is a true copy of my thesis, including any final revisions, as approved by my thesis committee and the Graduate Studies office, and that this thesis has not been submitted for a higher degree to any other University or Institution.

Abstract

Thermal spray coatings have been incorporated in oil and gas extraction efforts for many years. Recently, High Velocity Oxy-Fuel (HVOF) has become increasingly incorporated where erosive environments are present. This study investigates the microstructural and mechanical properties of HVOF WC-Co-Cr coatings deposited at SharkSkin Coatings ltd. The deposited coatings exhibited a low porosity with high adhesion strength, hardness, and superior erosion resistance. In this study, a recirculating solid particle erosion testing machine was designed and fabricated to simulate an erosive environment on a laboratory scale. This study was also aimed at improving microstructures and mechanical properties of the coatings by modifying the two coating deposition parameters e.g. standoff and pre-cycle heating. It was determined that pre-spray substrate heating negatively affected the coatings microstructures e.g. porosity, while reducing the stand-off distance positively influenced the coating microstructures and mechanical properties, e.g. erosion resistance.

Acknowledgements

First I would like to thank my advisor Dr. A. Edrisy for her supervision throughout the entirety of this project and for her consistent guidance through this endeavor. Additionally, Dr. K. Farokhzadeh for assisting in the evaluation process of this research as well as beneficial feedback throughout the entirety of this endeavor.

I would also like to thank my committee members Dr. J. Johrent and Dr. D. Green for being committed to attending my presentations and reviewing my thesis. Additionally, their beneficial input directly correlates to the caliber of work completed during my graduate studies.

Gratitude is also expressed to Dennis Sheffer and the employees of SharkSkin Coatings ltd. for providing a state of the art coating facility to apply TS coatings required for the bulk of this research.

Table of Contents

Declaration of Co-Authorship iii

Abstract iv

Acknowledgements v

List of Figures xi

List of Tables xx

Nomenclature xxiii

List of Abbreviations xxiii

List of Symbols xxiv

Chapter 1: Introduction 1

1.1. Organization of Thesis 3

Chapter 2: Literature Survey 4

2.1 Introduction to Thermal Spray Processes 4

2.1.1 Major Components of HVOF Equipment 5

2.1.2 Application Process of HVOF Coatings 7

2.1.3 HVOF Substrates 8

2.1.4 HVOF Coatings 9

2.2 Spray Parameters and the Influence on Coating Performance 9

2.2.1 Feedstock Particles 9

2.2.2 Pre-Spray Treatment 11
2.2.3 Flame Fuel 13
2.2.4 Particle Temperature 15
2.2.5 Particle Velocity 19
2.2.6 Stand-off distance 19
2.2.7 Deposition Rate 21
2.2.8 Post Coating Heat Treatment 23
2.3 Surface Engineering to Improve Erosion Resistance 24
2.4 Thermal Spray Required Properties 27
2.4.1 Microstructural Properties 27
2.4.2 Physical Properties 28
2.4.3 Thermal Properties 29
2.4.4 Magnetic Properties 29
2.4.5 Chemical Properties 30
2.5 Testing Methods of Thermal Spray Coatings 30
2.5.1 Coating Porosity 30
2.5.2 Coating Density 31
2.5.3 Hardness Testing 32
2.5.4 Adhesion Testing 32
2.5.5 Erosion Testing 33

Chapter 3: Material and Experimental Methods 53

3.1 Coating Feedstock 53

3.2 Sample Substrate 53

3.3 Coating deposition 54

3.3.1 Deposition Equipment 54

3.3.2 Deposition Procedure 55

3.3.3 Standard Deposition Parameters 55

3.3.4 Modified Deposition Parameter Procedure 55

3.4 Cross-Sectional Preparation and Microstructural Observation 56

3.5 Coating Characterization Testing Procedure 57

3.5.1 Coating Thickness 57

3.5.2 Coating Porosity 58

3.5.3 Coating Density 58

3.5.4. Surface Roughness 59

3.5.5 Hardness Testing 60

3.5.6 Adhesion testing 60

3.6 Erosion Testing 61

3.6.1 Erosion Resistance Measuring Method 61

3.6.2 Design and Fabrication of Solid Particle Erosion Testing Rig 63

3.6.3 Solid Particle Erosion Testing Procedure 64

Chapter 4: Experimental Results 73

4.1 Coating Feedstock Characterization Results 73

4.1.1 Feedstock Size Distribution 73

4.1.2 Feedstock Composition 74

4.1.3 Feedstock Morphology 75

4.1.4 Surface Temperature During Coating Deposition 75

4.2 Microstructural Characterization of Pre-Spray Treated Toughmet 76

4.2.1 Surface Roughness 76

4.2.2 Observation of Grit Blasted Surface 76

4.3 Microstructural Characterisation of The Coating 77

4.3.1 Coating Cross-sectional Microstructure 77

4.3.2 Coating Porosity 78

4.3.3 Coating Density 79

4.3.4 Coating Surface Roughness 81

4.4 Hardness Results 81

4.4.1 Standard Coating 82

4.4.2 Modified Pre-Spray Surface Temperature 82

4.4.3 Modified Stand-off Distance 83

4.5 Coating Adhesion Results 83

4.6 Solid Particle Erosion Results 85

Chapter 5: Discussion 129

5.1 Feedstock Characterization 129

5.2 Characterization of Standard Coating 131

5.3 Effect of Pre-spray Heating Cycles 136

5.4 Effect of Stand-off Distance 138

Chapter 6: Conclusions 142

Chapter 7: Recommendations 144

References 145

Appendix: Recirculating SPE Machine Operating Manual 150

Machine Limitations and Adjustments 150

Erosion Tester Design Considerations 150

General Operating Procedure 151

Vita Auctoris 156

List of Figures

Figure 1 - Typical flame temperature and particle velocity operation ranges for various TS systems [1]. 35

Figure 2 - Progression of particle temperature and velocity capabilities of HVOF generations [1]. 36

Figure 3 - HVOF spray torch schematic [53]. 36

Figure 4 - Polished cross-section of grit blast roughened Mar-M 509 coated with MCrAlY, where grit inclusions are observed at the interface [19]. 37

Figure 5 - Polished cross-section of waterjet roughened Mar-M 509 coated with MCrAlY [19]. 37

Figure 6 - Evolution of particle temperatures and velocities for two different fuel/oxygen mixtures [21]. 38

Figure 7 - Process diagnostic data for different spray parameter combinations for Propylene-Oxygen flame and Hydrogen-Oxygen flame [22]. 38

Figure 8 - Influence of deposition parameters on hardness of WC-Cr-C-Ni coating [54]. 39

Figure 9 - Effect of particle size on the oxygen content in HVOF Ni-Cr-AL-Y coatings [28]. 39

Figure 10 - Evolution of particle temperature vs. the stoichiometric factor (spray distance: 300mm, Fuel: Natural gas) [30]. 40

Figure 11- Schematic diagram of dependency of oxygen content in the coating on spray distance in two oxidation mechanisms. (a) effect of a single mechanism and (b) combined effect of two oxidation mechanisms [28]..... 40

Figure 12 - In-flight particle properties as a function of spray distance and particle size [15]..... 41

Figure 13 - Evolution of particle velocity vs. the stoichiometric factor (spray distance: 300 mm, Fuel: Natural gas) [30]..... 41

Figure 14 - In-flight particle properties as a function of spray distance and fuel gas [15]. 42

Figure 15 - Quenching, cooling, and residual surface stresses as a function of deposit thickness, with forced cooling [32]..... 42

Figure 16 - Quenching, cooling, and residual surface stresses as a function of deposit thickness, without forced cooling [32]..... 43

Figure 17 - SEM micrographs of single Wc-CoCr splats on Al and steel surfaces: (a) splats on Al surface; (b) FIB section of feedstock splat on AL surface, highlighting small defects (circle); (c) splat on steel surface; (d) FIB section of the splat on steel surface [33]. 43

Figure 18 - Plot of coating hardness against heat treatment temperature (error bars represent one standard deviation) [34]. 44

Figure 19 - Plot of coating steady-state wear rate against heat treatment temperatures for two applied loads, along with wear rates for sintered cermets using a modified dry sand rubber wheel technique [34]. 44

Figure 20 - Variation of the weight losses of the coated samples vs. the heat treatment temperature using a pin on disk tribometer (sliding speed 0.1 m/s, load 5 N, and sliding distance of 100m) [36]. 45

Figure 21 - Typical dependence of erosion on impact angle θ (defined as the angle between impact direction and the surface) [39]. 45

Figure 22 - Solid particle erosion wear mechanisms. 46

Figure 23 - Relative erosion factors for selected metals and ceramics [40]. 46

Figure 24 – Erosion test results (low energy sand slurry jet impingement using 135 µm sand at 2.25 wt.% concentration in water at 16.5 m/s and 90° impingement angle) of coated carbon steel with tungsten carbide compared with bulk erosion resistant materials [55]. 47

Figure 25 - Pressure and temperature categories of drilling environments, where LPLT stand for low pressure low temperature and HPHT represents high pressure high temperature [56]. 47

Figure 26 - Example of binary mask of coating cross-section containing 1.0 % porosity by area [57]. 48

Figure 27 – Beaker support above balance pan schematic, according to ASTM B962 [58]. 48

Figure 28 - Schematic of self-aligning adhesion testing fixture [18]. 50

Figure 29 - Typical erosion-time pattern and parameters used to quantify SPE erosion[48]. 50

Figure 30 – Schematic of high-velocity recirculating slurry testing rig [52]. 51

Figure 31 – Schematic of high velocity semi recirculating slurry testing rig [52]. 51

Figure 32 – Schematic of high velocity non recirculating slurry testing rig [52]. 52

Figure 33 - HVOF coating deposition of directional drilling component, applied at SharkSkin coatings ltd. Facility [60]. 66

Figure 34 – Standard HVOF coated Toughmet coupon in the as-sprayed condition. 66

Figure 35 – SEM BSE image of standard coating cross-section at 250 X. 68

Figure 36 - Coating density measurement test setup. 68

Figure 37 - Mitutoyo Rockwell hardness testing machine. 69

Figure 38 - Adhesion sample mounted to loading fixture and secured into tensile testing grips..... 69

Figure 39 - Digital image of fabricated erosion tester overview. 70

Figure 40 - Schematic structure of erosion tester slurry pumping system. 70

Figure 41 – Schematic structure of erosion chamber..... 71

Figure 42 - Schematic structure of erosion sample holder. 71

Figure 43 - SEM observation of Amperit 558 feedstock. 89

Figure 44 - Processed image of Amperit 558 feedstock using ImageJ. 90

Figure 45 - Relative frequency (%) of particle diameter (um) of Amperit 558..... 90

Figure 46- SEM image of amperit 558 prior to EDS analysis. 91

Figure 47 - EDS composition map colour coded based on detected compositions (Table 7). 91

Figure 48 - Overall composition of amperit 558 feedstock in percent weight. 92

Figure 49 - SEM image of densely packed solid particle at 3000 X magnification. 93

Figure 50 – EDS line scan of densely packed solid particle composition at 300 X (indicated by red line on previous image)..... 93

Figure 51- SEM image of porous solid particle at 3000 X. 94

Figure 52 – EDS line scan of porous solid particle composition at 3000 x (indicated by red line on previous image)..... 94
Figure 53- SEM image of porous hollow particle at 3000 X..... 95
Figure 54 – EDS line scan of porous hollow particle composition at 3000 x (indicated by red line on previous image)..... 95
Figure 55 – Effect of pre-heating cycles on surface temperature, measured using a mounted infrared thermometer aimed at the center of the work-piece after the completion of each deposition cycle, coated using the standard deposition parameters with a stand-off distance of ten inches. 96
Figure 56 - Effect of stand-off distance on surface temperature, measured using a mounted infrared thermometer aimed at the center of the work-piece after the completion of each deposition cycle, coated using the standard deposition parameters..... 96
Figure 57 - Three-dimensional topography of grit blasted toughmet at 20 X. 97
Figure 58 - SEM image of grit blasted substrate at 200 X (top view). 97
Figure 59 - EDS map of grit blasted substrate at 200 X colour coded based on detected composition (Table 9), where the blue region represents embedded blasting media in the substrate 98
Figure 60 - SEM image of blasting media particles embedded into substrate due to mechanical roughening prior to coating application at 2000 X. 99
Figure 61 – EDS spectrum of embedded blasting media particle (one) from Figure 60.. 99
Figure 62 - EDS spectrum of embedded blasting media particle (two) from Figure 60. 100
Figure 63 – SEM image of coating cross-section at 250 X. 100
Figure 64 - EDS map of coating cross-section (Figure 63). 101

Figure 65 - SEM image of coating cross-sectional interface at 400 X. 102
Figure 66 – EDS spectrum of location embedded blasting media particle (indicating Al_2O_3 particle) of SEM coating interface. 102
Figure 67 – EDS spectrum of location 2 (indicating WC particle) of SEM coating interface. 103
Figure 68 - EDS spectrum of dark grey region surrounding WC particles. 103
Figure 69 – SEM image of coating cross-section depicting inter-splat microcracks and a cracked WC particle at 8000 X. 104
Figure 70 - Optical image of coating cross-section of coating with standard deposition techniques (stand-off distance: 10”) at 20 X..... 104
Figure 71 – Processed image of optical image of standard coating cross-section (Figure 70), black pixels represent voids and or pores within the coating cross-section. 105
Figure 72 - Optical image of coating cross-section with one pre heating cycle at a stand-off distance on 10” at 20 X. 105
Figure 73 – Processed image of optical image of coating with one pre heating cycle (Figure 72), black pixels represent voids and or pores within the coating cross-section. 106
Figure 74- Optical image of coating cross-section with two pre heating cycle at a stand-off distance on 10” at 20 X. 106
Figure 75– Processed image of optical image of coating with two pre heating cycles (Figure 74), black pixels represent voids and or pores within the coating cross-section. 107
Figure 76 - Effect of pre-heating cycles on coating porosity, calculated using Image J from optical images of coating cross-section (red line indicates the desired minimum porosity of 1 (% area))..... 108

Figure 77 - Optical image of coating cross-section with modified stand-off distance (12”) at 20 X. 108

Figure 78 – Processed image of optical image of coating cross-section with a modified stand-off distance of 12 inches (Figure 77), black pixels represent voids and or pores within the coating cross-section. 109

Figure 79 - Optical image of coating cross-section with a modified stand-off distance (8”) at 20 X. 109

Figure 80 – Processed image of optical image of coating cross-section with a modified stand-off distance of 8 inches (Figure 79), black pixels represent voids and or pores within the coating cross-section. 110

Figure 81 - Optical image of coating cross-section with modified stand-off distance (6”) at 20 X. 110

Figure 82– Processed image of optical image of coating cross-section with a modified stand-off distance of 6 inches (Figure 81), black pixels represent voids and or pores within the coating cross-section. 111

Figure 83 - Effect of stand-off distance on coating porosity, calculated using Image J from optical images of coating cross-section (red line indicates the desired minimum porosity of 1 (% area)) 112

Figure 84 – Effect of pre-heating cycles conducted prior to coating deposition on coating density, coating density measured according to ASTM B962 using Archimedes method. 113

Figure 85- Effect of stand-off distance on coating density, coating density measured according to ASTM B962 using Archimedes method. 114

Figure 86 - Three-dimensional topography of WC-Co-Cr TS coating in the as-sprayed condition at 20 X..... 114

Figure 87 - Three dimensional topography of WC-Co-Cr TS coating in the ground condition at 20 X..... 115

Figure 88 – Effect of pre-heating cycles on coating hardness (HRA) of coatings in the as-sprayed condition (red line indicates the desired target hardness of 80 (HRA)). 116

Figure 89 – Effect of stand-off distance on coating hardness (HRA) of coatings in the as-sprayed condition (red line indicates the desired target hardness of 80 (HRA)). 117

Figure 90 – Effect of pre-heating cycles on adhesion strength, conducted according to ASTM C-633 (red line indicates the desired target strength of 69 Mpa, which is the rated strength of FM 1000 adhesive). 118

Figure 91 – Effect of stand-off distance on adhesion strength, conducted according to ASTM C-633 (the red line indicates the desired target strength of 69 Mpa, which is the rated strength of FM 1000 adhesive). 120

Figure 92 - SPE results of reference materials, uncoated toughmet, and coated toughmet in the as-sprayed condition, for a cumulative test duration of 150 minutes. The reference materials are conducted to calibrate the erosion tester as well as to develop a baseline for comparision between various erosion testers..... 121

Figure 93 – SPE erosion results of standard coating in the as-sprayed condition, for a cumulative test duration of 150 minutes. 121

Figure 94 – Maximum erosion and terminal erosion rates of reference materials, uncoated toughmet, and coated toughmet in the as sprayed condition. 122

Figure 95– Maximum erosion and terminal erosion rates normalized to toughmet erosion rates of reference materials, uncoated toughmet, and coated toughmet in the as sprayed condition. 123

Figure 96 - Stereomicroscope image of uncoated toughmet wear scar after 150 minutes of exposure. 123

Figure 97 – Cross-section of erosion scar (right half) of uncoated toughmet after 150 minutes of exposure (maximum depth of 1.72 mm as indicated by vertical line). 124

Figure 98- Stereomicroscope image of coated toughmet in the as-sprayed condition of wear scar after 150 minutes of exposure. 124

Figure 99 - SEM image of uncoated toughmet erosion scar after 150 minutes of exposure at 1000 X. 125

Figure 100 - SEM image of coated toughmet in the as-sprayed condition after 150 minutes of exposure at 1000 X. 125

Figure 101 - SEM image of coated toughmet in the as-sprayed condition after 150 minutes of exposure at 6000 X. 126

Figure 102 – Effect of stand-off distance on SPE, with a cumulative exposure duration of 300 minutes. 126

Figure 103 – Maximum erosion and terminal erosion rates of coatings with modified stand-off distance. 127

Figure 104– Maximum erosion and terminal erosion rates normalized to toughmet erosion rates of coatings with modified stand-off distances 128

List of Tables

Table 1 - Maximum recommended wire diameter for specimen suspension apparatus [58]. 49

Table 2 – Effect of temperature on the density of air-free water [58]. 49

Table 3 – Summary of desired coating mechanical properties target. 52

Table 4 - Standard coating deposition parameters. 67

Table 5 – Semi-automatic grinding/polishing procedure. 67

Table 6 – Surface preparation procedure of erosion samples prior to erosion testing. 72

Table 7- Legend of EDS elemental map for Figure 47. 92

Table 8 – Average surface roughness from three measurements of pre spray treated toughmet. 97

Table 9 – Legend of EDS map of grit blasted substrate for Figure 59. 98

Table 10 - Legend of EDS map for coating cross-section from Figure 64. 101

Table 11 - Effect of pre-heating cycles on coating porosity, calculated using Image J from optical images of coating cross-sections. 107

Table 12 – Effect of stand-off distance on coating porosity, calculated using Image J from optical images of coating cross-section. 111

Table 13 – Effect of pre-heating cycles conducted prior to coating deposition on coating density, the coating density was measured according to ASTM B962 using Archimedes method. 112

Table 14 - Effect of stand-off distance on coating density, the coating density was measured according to ASTM B962 using Archimedes method. 113

Table 15 - Average surface roughness of standard coating, measured by calculating the average of three surface measurements using an optical profilometer. 115

Table 16 – Uncoated toughmet and standard WC-Co-Cr coating hardness measured according to ASTM E-18. 115

Table 17 –Effect of pre-heating cycles on coating hardness in the as-sprayed condition. 116

Table 18 - Effect of stand-off distance on coating hardness in the as-sprayed condition. 116

Table 19 – Adhesion results of standard coating, conducted according to ASTM C-633. 117

Table 20 - Adhesion results of coatings deposited with one pre-heating cycles, conducted according to ASTM C-633. 117

Table 21- Adhesion results of coatings deposited with two pre-heating cycles, conducted according to ASTM C-633. 118

Table 22 - Adhesion results of coatings deposited with a stand-off distance of six inches, conduced according to ASTM C-633. 119

Table 23- Adhesion results of coatings deposited with a stand-off distance of eight inches, conduced according to ASTM C-633. 119

Table 24 - Adhesion results of coatings deposited with a stand-off distance of 12 inches, conduced according to ASTM C-633. 120

Table 25 – Erosion rates and minimum test duration of reference materials, uncoated toughmet, and coated toughmet in the as-sprayed condition. 122

Table 26– Resistance to erosion normalized to uncoated toughmet of reference materials, uncoated toughmet, and coated toughmet in the as-sprayed condition. 122

Table 27– Erosion rates and minimum test duration of coatings with modified stand-off distances. 127

Table 28 – Resistance to erosion normalized to uncoated toughmet of coatings with modified stand-off distances. 128

Nomenclature

List of Abbreviations

APS	Air plasma spraying
ASTM	American society for testing materials
DS	Detonation gun spraying
EDM	Electronic discharge machining
EDS	Energy Dispersive X-ray Spectroscopy
HDD	Horizontal directional drilling
HVOF	High velocity oxy-fuel
kgf	Kilogram-force
R_a	Average surface roughness (um)
R_{RMS}	Root mean squared surface roughness (um)
SPE	Solid particle erosion
SRB	Sulphate reducing bacteria
TS	Thermal spray
SEM	Scanning electron microscope
XRD	X-ray diffraction

List of Symbols

$A_{surface}$	Feedstock particle surface area [m^2]
Bi	Biot number
D	Feedstock particle diameter [m]
D_{of}	Diffusion coefficient of oxygen in the flame
h	Heat transfer coefficient [W/m^2K]
h_m	Mass transfer coefficient between particle surface and environment
h_{fg}	Enthalpy of fusion [J/kg]
K	Thermal conductivity [W/m·K]
L	Torch spray distance [m]
MI	Melting Index
MTD	Minimum test duration (min)
OI	Oxidation index
P_f	Average gas density around the particle
ρ	Density of feedstock particle in liquid state [kg/m^3]
Q_e	Maximum erosion rate (mm^3/min)
Q_{et}	Terminal erosion rate (mm^3/min)
S_e	Normalized erosion resistance

S_{et}	Normalized terminal erosion resistance
S_h	Sherwood number
Δt_{fly}	Feedstock particle in-flight time [s]
Δt_{melt}	Feedstock particle melting time [s]
T	Feedstock particle in-flight surface temperature [K]
T_f	Flame temperature near the in-flight particle [K]
V_{body}	Feedstock particle volume [m^3]
v	Feedstock particle velocity [m/s]
Y_{of}	Oxygen concentration in the gas phase
Y_{oc}	Oxygen concentration in the particle center
W_o	Atomic weight of oxidant
W_{ox}	Atomic weight of oxide product

Chapter 1: Introduction

Since the early 1900s, the abundance of oil and gas is constantly decreasing, creating a higher demand for more efficient extraction methods. The improved extraction methods have allowed companies to drill deeper wells on land and sea, however increasing the drill depth consequently reduces the service life of drill components. During the drilling process a drill head bores a hole of approximately 12 centimeters to 1 meter in diameter into the earth through dirt, shale, limestone, and sandstone. As the drill bit cuts into the earth, a drilling fluid typically consisting mainly of bentonite and water is pumped through the drill collars (shaft attached to the drill head) and expelled from the drill head. The drilling fluid serves two vital processes; to remove thermal energy from the drilling components and to transport drill cuttings to the surface. The resurfaced mud is then filtered and recirculated back downhole. The mud mixed with rock cuttings is extremely abrasive, which can cause excessive wear to vital components downhole. During the drilling process, premature component failure stemming from equipment wear and/or failure can occur, resulting in substational environmental and economic costs are, which has led to comprehensive research and development in wear resistant materials and coatings.

Currently, high velocity oxygen fuel (HVOF) coatings are becoming very popular in the oil and gas industry as well as aerospace and recently the automotive industry to improve the wear resistance of components. HVOF coatings have significant advantages over conventional coatings due to the versatility of application, low coating porosity, and high adhesion between coating and substrate. Although HVOF coatings have a potential to

benefit multiple industries the specific coating material and spray parameters must be optimized for individual applications.

The coating can be evaluated in terms of many parameters including; porosity, adhesion to substrate, hardness, fracture toughness, surface roughness, coating thickness, residual stress condition, wear resistance and corrosive resistance. Many of these coating parameters are interrelated, based on the initial spraying conditions, resulting in a delicate balance between deposition parameters. The primary spray parameters include; feedstock powder, substrate surface condition, fuel gas, fuel gas flow rate, carrier gas, carrier gas pressure, stand-off distance, and dimensions of spray nozzle. The ideal coating exhibits a low porosity, high adhesion to the substrate, high hardness and fracture toughness, as well as high wear resistance and chemical resistance.

As a result, this study investigates the deposition parameters, as well as microstructural and mechanical properties of deposited coatings of Amperit 558 spray powders (feedstock) applied through the HVOF process to be sprayed onto horizontal directional drilling (HDD) components made from spinodally hardened Toughmet (Cu-Ni-Sn). The main goal is to optimize the spray parameters to develop a dense, well adhered, wear resistant coating. To achieve this goal the particle morphology of feedstock powders will be investigated, as well as the coating hardness, adhesion, and wear resistance of the standard coating (Sharkskin's WC-Co-Cr coating deposited using their standard deposition parameters, shown in Table 4) and then compared to coatings applied with varying spray parameters.

1.1.Organization of Thesis

Chapter one provides an introduction to the basic background of the research as well as the organization of this thesis.

Chapter two contains includes a review of literature, introducing the effect of deposition parameters on the mechanical properties of HVOF TS coatings. The literature survey then discusses solid particle erosion (SPE) mechanisms and effects of TS coatings. Additionally, the chapter outlines previous studies conducted on individual deposition parameters and their effect on mechanical properties, as well as solid particle erosion (SPE) erosion testing.

Chapter three provides an outline of the materials and experimental procedures used to characterize the mechanical properties of TS coatings, including hardness, coating adhesion strength, and erosion resistance. As well as the design parameters of the solid particle recirculating slurry erosion tester design built for the purpose of this research. The chapter also elaborates on the coating characterization techniques used in this study.

Chapter four presents the results obtained from the microstructural characterization testing of the coating, as well as the results obtained from hardness testing, coating adhesion testing, and solid particle erosion testing.

Chapter five includes a discussion of the results represented in chapter four, including the erosion mechanisms occurring during the erosion testing and the effect of the modified deposition parameters on the microstructural and mechanical properties.

Chapter six summarizes the conclusions obtained from this project.

Chapter seven represents recommendations for future research.

Chapter 2: Literature Survey

2.1 Introduction to Thermal Spray Processes

Thermal spraying can be considered a general term incorporating various coating techniques, in which materials are heated (possibly melted) and impact the surface. There are various types of TS, which include plasma spraying, detonation spraying, wire arc spraying, flame spraying, warm spraying, cold spraying, and high velocity oxy-fuel (HVOF). Figure 1 represents the flame temperature and particle velocity for the previously mentioned TS processes. These coating techniques have similarities, and typically consist of the following components; spray torch (the main device which contains a combustion chamber required for melting and accelerating coating material), feeder (preheats and supplies the powder, wire or liquid to the torch), media supply (supplies gases or liquids required for combustion and carrying coating material), robot (manipulates the spray torch or substrate), power supply (provides electricity for the equipment), and control system (controls the previously list components).

The heated material is referred to as “feedstock”, which is heated by means of electrical (plasma or arc) or chemical (combustion flame), to remove moisture and reduce the temperature differential between the feedstock and combustion chamber. The feedstock is fed into the combustion chamber, where is it heated and accelerated out of the spray torch nozzle. Based on the spray parameters and feedstock characteristics the feedstock particles are thermally softened to a molten, semi-molted, or solid state. Ideally the particles should be between the molten or semi-molten state in order for the particles to effectively interlock creating a well adhered dense coating.

The trend in the HVOF process development has been towards higher particle velocity and lower particle temperatures. This has a clear influence on the coating microstructure, where amount of oxidation in the lamella boundary is decreased and flattening rate is increased, due to this the coating density and adhesion are improved with increasing particle velocity [1]. This trend can easily be perceived in Figure 2.

2.1.1 Major Components of HVOF Equipment

The fist component is the powder feeder, which acts as a powder material reservoir while preheating the powder. The powder is heated to remove moisture prior to coating and reduce the temperature differential between the powder and flame. This is a vital step due to the short dwell time a particular particle spends within the combustion chamber and flame. Therefore if the temperature differential is too large the particles will not be sufficiently heated and impact the substrate in a solid state, resulting in poor mechanical interlocking and thus poor coating quality. Additionally, the powder feeder supplies the preheated powder to the spray torch for application.

The spray torch (Figure 3) is the most important component of the HVOF coating process, which contains the combustion chamber, allowing the fuel mixture, carrier gas, and coating material to mix and be expelled through the nozzle. The nozzle is typically a converging diverging lavel nozzle, which accelerates the jet velocity up to 1000m/s and the powder particles up to 800 m/s. The gas stream is directed towards the work piece, where the powder particles impact the work piece and form a thin coating.

The spray torch is mounted to an articulating robotic arm. The arm manipulates the orientation of the spray torch, which allows for control of the linear distance between the nozzle tip and work piece as well as the traverse velocity along the rotational axis of the

work piece. Depending on the work piece size the robotic arm can also be programmed to remove the flame from the substrate to allow for sufficient cooling between application passes, or continue at the starting location after the completion of a cycle. While the spray torch is traversed along the work piece, the work piece it typically rotated on a lathe, enabling the spray torch to apply a uniform coating thickness along the entire circumference of the work piece, as well as even heat distribution along the work piece. The rotational speed of the work piece, traverse speed of the spray torch, and the material feed rate have a significant impact on the deposit thickness of each pass. If the thickness per pass is too large the molten coating has the potential to accumulate and pool, allowing the rotational inertia to potentially remove molten splat formations from the substrate. Additionally, this could cause excessive substrate heating, causing undesired microstructural modifications to the substrate and additional thermal stresses. However, if the thickness per pass is too low, each work piece will require additional passes to develop the desired coating thickness, increasing the application time. P.H. Suegama and C.S. Fugivara discovered when the Cr_3C_2-NiCr coatings were applied to steel substrates by means of HVOF spraying, the coating porosity was reduced from 1.5% to 1% when the spray torch transvers speed was increased from 500mm s to 1000 mm s [2].

The final major component of HVOF equipment is the power supply and control system. The power supply outputs energy for the components to function properly, while the control system is responsible for manipulating the intricate working mechanisms within the equipment, such as valves and pump to control the gas and powder feed rates. Both of these systems can be independent for each component or integrated into a single power supply and control system.

2.1.2 Application Process of HVOF Coatings

The first step of any coating process is surface activation. The surface to be coated must be thoroughly cleaned and grit blasted to roughen the surface to allow mechanical interlocking of the initial splats. It is important to note that the strength of the coating-substrate interface can be compromised by embedment of grit into the substrate during blasting by the presence of grit remnants prior to deposition, which act as stress raisers and are agents for interfacial crack propagation and delamination of the coating when stress induced by tribological contacts are large enough to act at this interface [3]. The surface can be roughened by sandblasting with various aggregate materials, shot peening, and more recently water-jet treatment.

The second step is to increase the feedstock temperature to the molten and or semi-molten state. This is accomplished by introducing the preheated feedstock material into the hot gas stream exiting the combustion chamber of the spray torch. Once the feedstock particles enter the gas stream they are accelerated and heated within the jet stream until the particle impacts the substrate. Although the flame temperature varies in the range of 2500ºC – 3200 ºC depending on the fuel gas to oxygen ratio [1] the feedstock particles typically do not exceed 2000ºC, due to the short particle dwell time within the flame. Prior to impact the particles can reach a maximum velocity in the range of 400-1000 m/s based on the gas flow rates and stand-off distance [1].

Upon impact individual particles deform into flattened splats on the substrate surface due to the thermal softening and the kinetic energy from the jet stream. Particle splats conform to the substrate topography and are rapidly quenched allowing for mechanical keying (anchoring) and diffusion bonding between the particle feedstock and

substrate. The accumulation of splats on the substrate form a thin tribo layer in the range of approximately 3-20 μm per pass [4]. The spray torch is then directed away from the work piece for a set rest time, allowing the coating to cool and solidify. After the rest time the spray torch is returned to the initial position to apply the second layer of the coating. This process continues until the desired number of passes and therefore the coating thickness is achieved. After all layers of the coating are applied the work piece is removed from the lathe and allowed to cool to room temperature, unless a post coating heat treatment is desired.

2.1.3 HVOF Substrates

In previous years coating substrates used in drilling operations ranged have been comprised of various alloys, but recent manufacturing techniques have allowed the implementation of spinodally hardened copper-nickel-tin (Cu-Ni-Sn) alloys otherwise known as Toughmet. This substrate has been chosen due to its high strength, magnetic transparency, galling resistance, and resistance to corrosive environments. The high mechanical strength of this alloy is produced by controlled thermal management called spinodal decomposition. Spinodal structures are fine, homogeneous two phase mixtures, which are produced when the original phases are separated under certain conditions of temperature and composition, such as in a supersaturated solid solution of metals whose atoms are similar in size. When spinodal decomposition occurs the original phase spontaneously decomposes into other phases in which the crystal structure remains the same, but the atoms in the crystals are different. Due to the fact the atoms are similar in size, the, the heat-treated spinodal structure retains the same geometry as the original, which prevents thermal distortion during heat treatment [5].

2.1.4 HVOF Coatings

TS coatings are distributed in the form of powder feedstock and are comprised of various elements, particle size, and particle compositions. Tungsten carbide-cobalt (WC-Co) based feedstock materials are used extensively in industry in their sintered as well as thermally sprayed forms [6]. The morphology of small WC particles embedded in a cobalt matrix allow TS coatings do be deposited without excessive substrate heating, while providing significant abrasive and erosive resistance, due to the network of WC particles throughout the coating.

2.2 Spray Parameters and the Influence on Coating Performance

This section outlines some of the parameters affecting HVOF coatings as described by previous research. This section incorporates everything from feedstock to equipment settings in an effort to explain the effects of a specific parameter on the coating microstructure and performance.

2.2.1 Feedstock Particles

The foundation of HVOF coatings lie within the feedstock, where changing the composition, particle size, and particle distribution have a significant impact on the coating performance. The chemical composition of feedstock can vary greatly between two suppliers as well as the size distribution, and particle morphology. In the case of Tungsten carbide-cobalt (WC-Co) feedstock's the hard tungsten carbide (WC) particles form the wear resistant component of the coating, while the cobalt acts as a binder component of the coating. In the sintered material, the WC grains tend to touch one another and form a continuous "skeleton" of carbide, with the cobalt binder occupying the spaces between the carbide grains [7].

Regarding the particle size and distribution, the processing methods have a noteworthy impact. Cast and crushed powders examined have been reported to have an average particle size between 10 μm [8] and 15μm [9], with a particles ranging from about 5 - 40 μm. Sintered and crushed powders have been found to typically contains WC of 5 – 7 μm and seem to have less size variation compared to cast and crushed powders [10] & [11]. While agglomerated and sintered/densified powders contain very fine WC particles from 3-5 μm [8] to 1-2 μm [9]. Due to the variation in particle size, the coating deposition may be affected, as larger particles require more thermal energy to be heated, which could be altered by the pre heated temperature, flame temperature, or the particle dwell time within the flame. Moreover, the decrease in particle velocity due to increased particle size makes it difficult to achieve a dense WC-Co coating with large particles (44μm) [12]. On the contrary, as the particle size decreases the inflight particle temperature gradient increases making the feedstock more susceptible to decarburization, which was studied by Yunfei Qiao and colleagues, determined increased decarburization increases the coating hardness, but decreases sliding wear and abrasive wear resistance by delamination of large plates [13]. Yunfei Qiao also found that the nanostructured powders used for coatings in their study had hollow spheres and were subject to extensive decarburization. Moreover, regarding particle distribution, if the particles have a large variance it is difficult to optimise the spray parameters, due to the fact that there will be abnormal particle velocities and temperatures during spraying.

Although powders can have identical chemical composition, they can have severely different particle morphology. The particle morphology is impacted by the manufacturing process and can include spherical, blocky, or irregular geometries. Irregular shapes can

range from blocky with an elongation ratio close to one, to needle like with high-elongations ratios. Moreover, blocky particles are always dense, while spherical or irregular particles can be dense or porous due to the large range of void content [14]. Additionally, the feedstock flow rate can impact the coating, by increasing the feedstock flow rate the particle temperature can be reduced. This is achieved when the combustion power is held constant which ultimately reduced the specific heat available for individual feedstock particles, thus reducing melting and oxidation tendency during flight. E. Lugscheider, C. Herbst performed metallographic investigation of HVOF coatings and found that coating with the lowest oxygen content mainly consiteded of unmelted particles, while competely melted particles exhibited oxide phases [15].

2.2.2 Pre-Spray Treatment

Pre-spray treatment incorporates several steps including; surface cleaning, surface activation, and surface masking. These steps are required to develop a clean and roughened surface for the coating to adhere too. If these steps are not properly performed the coating will not adhere well to the substrate, compromising the wear resistance and therefore the integrity of the entire coating. Surface cleaning is the first step, which removes any contaminants from the manufacturing process. This is achieved by a degree of cleanliness Sa2, Sa2.5, Sa3 [16], which represents through blast-cleaning, very through blast cleaning, and blast-cleaning to visually clean steel respectively, which originated from The Swedish Standards Institution on surface preparation standards. A common agent to produce this level of cleanliness is acetone to remove any residue from the manufacturing or machine processes.

Once the surface is thoroughly cleaned, the surface must be roughened by way of abrasive or mechanical blasting. The abrasives can vary from; steel or iron powder, aluminium oxide, glass beads, or even high pressure water. The ideal abrasive will promote adequate roughness with a low level of anchoring into the substrate. Inadequate surface roughening leads to poor coating adhesion, while over roughening of the substrate can affect the coating roughness, which is undesirable when small dimensional tolerances are required. Y. Wang studied the effect of substrate roughness on WC-Co HVOF coatings and found when the mild steel surface roughness was relatively smooth (Ra 1.7 μm) the adhesive strength ranged from 25 to 40 MPa. Moreover, when the substrate surface was aggressively roughened (Ra 5.8 μm) all tested specimens exhibited adhesive failure and the coatings reached adhesive strength in excess of 70 MPa [17], which is comparable to the adhesion strength of FM-1000 adhesive recommended in ASTM C633 [18]. J. Knapp and colleagues found similar results when comparing the adhesion strength of MCrAlY coatings applied to Inconel 718 and Mar-M 509. The main difference being that J. Knapp studied the adhesion strength of conventional grit blasting substrate roughening compared to waterjet (WJ) roughened substrates. J. Knapp concluded that the bond strength of WJ roughened substrates exceeded 70-75 MPa, while only one trial of the grit blasted substrates (60 mesh angular grit) reached the range of water jet roughened and the remaining grit blasted trials failed at the bond interface between 46 to 58 MPa [19]. Therefore, it is possible that the reduction in coating bond strength is due to the previously mentioned stress risers from embedded grit particles, which can be seen at the substrate and coating interface in Figure 4. It should be noted that when the substrate is roughened with WJ technology there are no visible inclusions, as seen in Figure 5. This concludes that

WJ surface activation has the potential to improve coating adhesion strength by removing embedded blasting media from the bond interface.

The final step of pre spray treatment is masking. Mechanical masking is required to prevent coating application to unnecessary work piece components. Depending on the desired surface finish, masking can be applied to the work piece prior to grit blasting to protect the surface from surface roughening as well as coating application. The abrasion resistant mask is generally made of Teflon, plastics, or rubber. This mask is then removed and a different mask is applied prior to spraying, this mask is strictly to prevent coating adhesion to undesirable surfaces and is made of metallic tape, glass fibers tape, or chemical liquids, such as Metco Anti Bond [20].

2.2.3 Flame Fuel

Although the selection of the appropriate fuel may be easily overlooked, the flame fuel and carrier gas have a significant impact on the performance of HVOF coatings. Flame fuels can range from; hydrogen, propane, kerosene, ethylene, propylene, or natural gas, while the carrier gas can be compressed air, but typically an inert gas such as nitrogen or argon. The flame fuel is required for combustion heating of feedstock particles while the carrier gas is responsible for accelerating the feedstock particles towards the substrate. The selection of the appropriate flame fuel and carrier gas can be decided based on the desired production requirements, economical factors and desired coating quality. When coating quality is the most important influence of the selection process, E. Lugscheider and C. Herbst suggest using hydrogen as a flame fuel and nitrogen as a carrier gas [15]. This is due to the lower nozzle exit temperature when using hydrogen over propane, which allows for particles to be thoroughly heated without complete particle melting and higher particle

velocity. J. Picas and M. Punset studied the oxygen/fuel ratio on the in-flight particle parameters and properties of HVOF WC-CoCr coatings with hydrogen and kerosene fuels. They observed higher particle temperature and lower particle velocity when hydrogen was used over kerosene (Figure 6), which resulted in a higher micro hardness and lower specific wear rate respectively [21]. E. Turunen and T, Varis also studied the effect of fuel type and fuel/oxygen ratio for Propylene and Hydrogen fuels and it was observed that a wider melting spectrum is demonstrated by the propylene-oxygen system [22], shown in Figure 7.

Once the flame fuel and carrier gas have been chosen the fuel/oxygen ratio and the flow rate of carrier gas must be carefully selected. The fuel/oxygen ratio impacts the flame enthalpy, temperature, and velocity, therefore by altering the fuel/ oxygen ratio and total gas flow rate the in-flight particle temperature and velocity can be controlled. As previously stated the in-flight particle temperature and velocity has a substational effect on the coating porosity, hardness, oxide content and wear rate. The fuel/oxygen ratio can be divided into three categories based on chemistries; neutral (N), reducing (R), and oxidizing (O). The neutral category represents optimum combustion in which the fuel/oxygen ratio is stoichiometric balanced and the maximum flame enthalpy. Reducing category has a fuel rich condition and the oxidizing has an oxygen rich condition. It should be noted that if high-pressure air is used as the carrier gas the oxygen within the air (~20%) will affect the stoichiometric fuel/oxygen ratio. W. Fang and T.Cho investigated the effect of oxygen and hydrogen flow rates on the coating hardness, as well as the feed rate and standoff distance. They determined altering the gas flow rates, spray distance, and feedstock flow rate using the Taguchi program of optimization and discovered that the coating porosity remained

nearly constant (1.2-3.7 %), but the hardness was increased with increasing oxygen content, while the hardness decreased with increasing hydrogen fuel rates, as shown in Figure 8. The high temperature and oxygen rich atmosphere caused the decarburization of WC particles within the feedstock into tungsten sub-carbide phases (W_2C W_3C), which then transforms to metallic W [23] [24]. Although the formation of sub-carbide phases increases the coating hardness, the brittle characteristics of sub-carbide phases can reduce the coating toughness and increase the wear rate. Therefore the formation of sub-carbide phases must be mitigated relative to the desired coating properties.

2.2.4 Particle Temperature

The particle temperature typically corresponds to the surface temperature of any particular particle prior to impacting the substrate. The particles are heated from the thermal energy of the flame to the molten or semi molten state, where the particle surface temperature is effected by the; flame temperature, in-flight time, particle size, particle density, feedstock rate, and the particle thermal conductivity. Provisional of the desired coating properties, it is usually undesirable for the particles to reach the fully molten state as the feedstock will decarburize and sub—carbide phases will become dominant, making the coating behave in a brittle nature. To calculate the state of an in-flight particle the Melting Index (MI) can be developed. MI takes into account the time particles stay under the influence of flame and particle size. It can be expressed as Equation [1] from [25]:

[1]

$$MI = \frac{T\ x\ \Delta t_{fly}}{D}$$

Where T = measured particle surface temperature [K], D = particle size [m], and Δt_{fly} particle in-flight time assuming constant acceleration of particles [s]. In the MI formula the $\Delta t_{fly} = 2L/v$, where L = spray distance [m], and v = particle velocity [m/s]. MI can be defined as the ratio of particle residence time in the flame to the total time needed for particle to melt: MI = Δtfly/Δtmelt. There is also more thorough description of melting index, which incorporates thermal resistance and energy balance analysis to the formula, which can be expressed as Equation [2] from [26]:

[2]

$$MI = \frac{\Delta t_{fly}}{\Delta t_{melt}} = \frac{24K}{\rho h_{fg}} x \frac{1}{1 + {}^{4}/_{Bi}} x \frac{(T_f - T_m) x \Delta t_{fly}}{D^2}$$

Where K is the thermal conductivity [W/m·K], ρ is the density of the material in liquid state [kg/m^3], h_{fg} is the enthalpy of fusion [J/kg], and T_f is the flame temperature near the in-flight particle [K], T_m is the melting point of the material [K], D is the particle size [m], and Bi is the Biot number. The Biot number can be represented by Equation [3], where h is the heat transfer coefficient W/m^2K, V_{body} is the particle volume, $A_{surface}$ is the particle surface area, and K is the thermal conductivity of the particle.

[3]

$$Bi = \frac{h \frac{V_{body}}{A_{surface}}}{k}$$

Applying Equation [2] can be used to predict the molten state of in-flight particle feedstock relative to the spray parameters. A MI value of one means the in-flight time equals to the time required for the particle to become molten, therefore a MI value equal to or greater than one represents fully molten particles. The remaining particle states can be

represented by partially molten ($0 \leq MI < 1$) or unmolten ($MI < 0$). Comparing the MI values for different process conditions allows for the approximation of the particle state and thus the ability to develop an approximate range of allowable flame temperature and particle velocity for the desired particle state. These ranges can be used to develop a first order process map (particle temperature and particle velocity) which can be used to narrow the range of process variables such as gas flow rate, stand-off distance, feedstock flow rate.

Beyond the molten state the phase composition and oxide content can be modified by the particle temperature. In contrast to ceramics, oxidation is an important attribute of metallic particle in-flight behavior. This oxidation significantly influences the phase composition, microstructure, properties, and performance of sprayed coatings. Metal oxides are brittle and have different thermal expansion coefficients than that of the metal, the inclusion of which may cause the spalling of the coating [27]. These oxides are typically grown on the lamellar interface and can improve the coating hardness, but causes the coating to become brittle if the oxide content is too high and thus reduce toughness and wear resistance [28]. The amount of oxide formation can be characterized by the oxidation index (OI), which has been shown to agree well with the oxide mas fraction predicted by H. Xiong and colleagues [29]. The OI can be calculated from Equation [4].

[4]

$$\mathrm{OI} \approx \frac{6(Y_{o,f} - Y_{o,c})}{\rho_l} \frac{W_{ox}}{W_o} \frac{\mathrm{Sh}\rho_f D_{o,f}}{d_p} \frac{L}{V_P d_p} \propto \frac{L}{V_P d_p^2}$$

Where L is the stand-off distance in meters $Y_{o,f}$ and $Y_{o,c}$ are the oxygen concentration in the gas phase and in the particle center, respectively, W_o and W_{ox} are the atomic weight of the oxidant and the oxide product, respectively, S_h is the Sherwood

number and it is defined as $Sh = \frac{2h_m r_p}{p_f D_{o,f}}$, $D_{o,f}$ is the diffusion coefficient of the oxygen in the flame, P_f is the Favre-averaged gas density around the particle and h_m is the mass transfer coefficient between particle surface and the environment. This has revealed that the oxide content increases with increasing spray distance and decreases with increasing particle size and velocity [26]. Additional research has confirmed the decrease in oxygen with increasing particle size, as shown in Figure 9. The research also suggests a transient particle size range can be proposed by which the controlling oxidation mechanism leading to oxide inclusion is changed from the in-flight oxidation domination to the post-impact oxidation domination [28]. This is represented in Figure 11, where in (a), the dashed line shows the dependency for the post-impact oxidation, while the three solid lines illustrate the dependency for the in-flight oxidation for different particle sizes. In (b), the effect of the controlling oxidation process on the oxygen content is schematically illustrated, which is determined by particle size. When the effects of two oxidation mechanisms are comparable for the transient particle size, the effect of spray distance on the oxygen content in the coating becomes minor as indicated by dotted line. Suggesting a major parameter for controlling coating oxide content may be the particle size and temperature.

Additionally the flame chemistry can affect the particle temperature. M. Planche and colleagues measured the particle temperature of Inconel 718 feedstock using a varying stoichiometric fuel/oxygen ratio of natural gas. They realized that although there is a large standard deviation the particle temperature progressively increases as the fuel/oxygen is enriched from 0.78 to 1.38 when a stand-off distance of 300 mm was used [30].

2.2.5 Particle Velocity

Similar to temperature, the particle velocity has a large impact on coating performance and in the case of HVOF coating applications the velocity can range from 400-1000 m/s as seen in Figure 1. The increased kinetic energy supports particle splat flattening and has been shown to reduce the coating porosity [1] which is typically in the range of 1% by volume and is one of the main advantages of using the HVOF coating process. The increased particle velocity reduces the particle dwell time within the flame and thus the particle temperature and oxidation content. The particle velocity can be effected by the gas pressure, fuel/oxygen ratio and thus the total gas flow rate, but is mainly effected by the carrier gas. As the purpose of the carrier gas is to accelerate feedstock particles towards the work piece. The particle size and morphology will also modify the velocity as they will inherently change the drag force each particle is subjected to, this can observed in Figure 12, where the velocity is substantially changed when the particle size changes. The particle velocity can also be affected by the fuel/oxygen ratio where it has been found that increasing the fuel/oxygen ratio the temperature decreases and the particle velocity increases [30] [31], as shown in Figure 13. The particle velocity was increased approximately 100 m/s to 500 m/s when the fuel/oxygen ratio was raised from 0.78 to 1.38. Besides gas flow rates and stand-off distance the velocity can be modified using different chamber and nozzle designs. When the feedstock rate increase there is an inherent flame quenching effect resulting in reduced particle temperature and velocity [31].

2.2.6 Stand-off distance

The stand-off represents the linear distance between the gun nozzle and the work piece surface. As the stand-off distance increases the particle dwell time evidently

increases, which consequently causes the particle temperature and subsequently the degree of particle melting to increase. Regarding velocity the particles are subjected to a normal force accelerating them towards the work piece from the carrier gas and a drag force opposing the normal force based on the particle size and morphology. As the particle distance from the nozzle tip increases the carrier gas and particles lose kinetic energy due to the opposing drag force and the particle velocity reduces. Therefore there is a maximum velocity occurring at a specific stand-off distance, this concept is represented in Figure 14 where Propane and Hydrogen fuels were used to spray NiCr 80-20; -56 to +31 μm powder was applied with a Jet-Kote spray system. It was found that increasing the stand-off distance from 250mm to 300mm reduces the oxygen content by roughly a third. The reason being that hot combustion gases increase oxidation by atmospheric oxygen entraining the flame jet and blowing onto the hot surface when close enough and by increasing the spray distance, the heat load on the substrate is reduced thus supressing severe oxidation [15].

Prior to reaching the optimal stand-off distance the particles will have a relatively low temperature and velocity, which would result in solid particle impact upon the substrate. This scenario could result in high coating porosity, reduced coating adhesion, and an overall unsatisfactory coating performance. Alternatively, if the optimal stand-off distance is exceeded the increased particle temperature could cause complete particle melting and oxidation. Additionally, the particle velocity will be reduced. The combination of these effects can cause the resulting coating to contain a larger than desired percentage of carbides, resulting in a brittle coating.

2.2.7 Deposition Rate

The rate of deposition is the quantity of feedstock particles deposited onto the substrate in a single pass and can be represented as the deposited thickness per pass. The deposition rate is influenced by several parameters including; the feedstock flow rate, robot traverse speed, and the surface speed of the rotating work piece. Since the feedstock flow rate effects the particle temperature and velocity by way of flame quenching as previously discussed, it will be disregarded in this section. The robot traverse speed, is the velocity at which the robot travels along the axis of rotation of the work-piece, while the surface speed represents the work-piece velocity at the deposition location and can be modified by changing the work-piece rotations per minute since the work-piece radius is already established. Therefore the overall coating thickness can be estimated by the deposition thickness per pass multiplied by the number of passes.

The deposition rate influences the development of residual stresses largely dependent on thermal conditions and are a combination of quenching stresses during deposition and cooling stresses post-deposition. During deposition thermal stresses develop between the substrate and coating, due to the difference in thermal-expansion coefficients, as well as within the coating due to the difference in thermal-expansion coefficients between metal carbides and binder metals. The difference in thermal-expansion coefficients also impacts the coating by the development of cooling stresses caused by the thermal contraction after coating deposition. In the case of Wc-Co coatings the thermal contraction of the cobalt binder is approximately three times that of tungsten carbide [7]. The residual stress limits the thickness of the deposit achieved by causing adhesion loss between the deposit and its base material, interlaminar debonding, and crack

formation. J. Stokes and L. Looney [32] studied the residual stresses in Wc-Co coatings as a function of coating thickness with and without forced conduction cooling and determined that a coating thickness of 1.2 mm is relatively stress-free when forced conduction is used, shown in Figure 15. When forced cooling was not used the tensile quenching stresses and the compressive cooling stresses are both larger than when forced conduction cooling was used, resulting in a stress-free coating at a thickness of approximately 0.6 mm, shown in Figure 16. This phenomenon is caused by the difference in thermal-expansion coefficients, when conduction cooling is implemented the work-piece temperature is reduced, therefore lowering the quenching and cooling stresses.

Additionally, the effect of coating thickness can influence the tribological properties of the coatings. During the initial pass the feedstock particles impact the substrate directly and the particles can impact and flatten or they can penetrate the substrate, which is typically undesired. G. Bolelli and colleagues studied these initial impacts and found upon impact, HVOF-sprayed Wc-CoCr particles deform the relatively soft aluminium substrate remarkably, penetrating deeply into its surface. Therefore the cermet particles cannot flatten and spread extensively and small defects and pores remain inside the non-flattened particle, causing a relatively large porosity of 3.2 ± 1.1 percent when two layers were applied [33], this phenomenon is reduced as the substrate hardness increases. The splat morphology of feedstock particles impacting aluminium and steel substrates is shown in Figure 17. The large void in Figure 17 (b) is due to the feedstock particles penetrating into the Al substrate and therefore not flattening, which increases the coating porosity and a reduction in adhesion. As the coating thickness increases the porosity decreases which can be justified by two reasons. First, as the torch passes continue

in front of the substrate, the impact of new WC–CoCr particles peens the previously deposited layers intensively and increases the density of the initial layers, but this does not explain the high density of the top coatings as they have not undergone any peening action. Therefore a second phenomenon is present, where the newly incoming particles encounter a much harder surface after sufficient passes have been deposited (approximately two passes), modifying the splat behaviour which performs similar to the previously mentioned impact upon steel. The combination of these phenomena result in a high density coating throughout, when sufficient passes have been deposited, which has been shown by G. Bolelli to have a significant reduction in the wear rate [33].

2.2.8 Post Coating Heat Treatment

Once the coating has been applied a post coating heat treatment can be implemented. Heat treatments have been shown to reduce residual stresses from HVOF spraying [34], but can result in significant phase changes within the coating and substrate. Therefore the heat treatment temperature and duration must be carefully selected. Along with a reduction of residual stresses the wear resistance of WC-Co coatings has been shown to be improved by heat treatment, due to the increase of carbide content through recrystallization of the amorphous phase into one of the eta carbides (M_6C or $M_{12}C$) [35]. Typical heat treatment temperatures needed for the amorphous phase to recrystallize are high (>600ºC) [35], but D. Stewart have observed improvements in the wear resistance of WC-Co coatings of up to 35% with heat treatments temperatures as low as 250 ºC conducted in inert gas [34]. Figure 18 depicts the micro hardness relative to post coating heat treatment temperature, while Figure 19 shows the wear rate of WC-Co coatings for applied loads of 50 N and 75 N as a function of heat treatment. From this plot the reduction

in wear rate is easily recognisable and shows the lowest wear rate corresponding to a heat treatment temperature of 600 ºC, suggesting an optimal treatment temperature. Additionally, XRD was conducted on the coating for all heat treatment temperature and it was observed that no phase transformations occurred up to 600°C, but new eta carbide peaks were observed at 700°C along with a reduction in the intensity of the two amorphous peaks present in the as-sprayed spectrum. Although heat treatment always caused a reduction in the residual stress within the coating, micro cracking also occurred at varying degrees. Micro-cracking and a reduction in the residual stresses in the coating were seen as beneficial in promoting abrasive wear resistance of the coating, caused. However, large scale cracking of the coating, caused by high-temperature treatments, resulted in sites of preferential wear within the coating [34]. S. Khameneh also reported the formation of eta phases converted from the amorphous binder phase and WC particles during post coating heat treatment [36], but contrary to previously mentioned findings they reported a reduction of wear resistance with heat treatment. This is represented in Figure 20, as the weight loss compared to heat treatment of WC-17-Co coatings.

2.3 Surface Engineering to Improve Erosion Resistance

Erosion due to the loss of material by repeated particle impacts of small hard particles is commonly referred to as solid particle erosion (SPE), the effects of this erosion are detrimental to many components, commonly causing increased operating costs and on occasion pre-mature failure resulting is catastrophic damage. This specific type of damage is commonly found in many engineering fields such as horizontal directional drilling (HDD), steam and jet turbines, pipelines, valves, and hydropower stations, etc. [37], [38]. Solid particle erosion occurs whenever hard particles are suspended in a gaseous or liquid

medium impinge on a solid surface at significant velocities. SPE results in significant thinning of components, typically type one cutting, and occasionally roughening of the exposed surface, which can lead to increased stress due to the removal of material and dimensional instability, leading to pre-mature failure. Significant factors for consideration of the severity of SPE are impacting particles (size, morphology, hardness, and fracture toughness), impacting surface (hardness, work hardenability, and microstructure).

In erosion literature, the materials subjected to erosion testing are generally divided into two categories, ductile or brittle. Where the maximum erosion rate in ductile materials such as pure metals occurs at low impingement angles (15º-30º), while brittle materials such as cermet coatings exhibit a maximum erosion rate at or near 90º, the typical dependence of erosion upon impact angle is represented as Figure 21.

Additionally, the impact angle and impacting particle morphology can affect the SPE wear mechanism, which was developed by Hutchings [39], where two modes of cutting and ploughing erosion were observed. A schematic of these wear mechanisms is represented in Figure 22, where ploughing deformation is typically caused by spherical particles. Type I cutting is caused by angular particles rotating forwards during impact, which would occur at low impact angles, where Type II cutting is caused by angular particles rotating backwards during impact caused by high impact angles. Hansen [40] compared the erosion rates of a variety of alloys, ceramic and cermets under certain erosion test conditions as shown in Figure 23. Tungsten, molybdenum and 1015 steel had the lowest resistance to erosion among other metals and most ceramics exhibited low erosion rate values.

Attempts have been made to reduce erosion damage to metal substrate by deposition of cermet and ceramic coatings. Carbide coatings are commonly used for tribological applications and various carbides are used within these coatings but among them tungsten carbide and chromium carbides are the most preferred. These protective coatings are usually applied on the surface of components using TS processes including plasma spraying, high velocity combustion or detonation gun. The high temperature of the spray torch, the chaotic character of the processes and the rapid cooling of deposits associated with these techniques result in complex chemical transformations and lead to the formation of metastable phases within the coatings [41]. Air plasma spraying (APS) coatings are considered to be cheaper; however, presence of oxygen is found to promote the nucleation of oxy carbides and considerable decarburization which are undesirable for wear resistance. It is the high velocity processes such as high velocity oxy-fuel (HVOF) and detonation gun spray (DS) processes minimize decomposition of the carbide phase due to lower heat enthalpy and shorter duration involved in the coating process [42]. Suggesting, HVOF and DS coatings will outperform many APS coatings under SPE conditions.

The HVOF coating process uses significantly lower deposition temperatures relative to air plasma spray (APS) processes and therefore is desirable for coating low melting alloys. Additionally, the higher particle velocity of HVOF TS during deposition provides several advantages such as lower porosity, increased mechanical interlocking providing higher adhesion strength, and increased hardness. Therefore cermet coatings deposited by high velocity TS processes, such as HVOF, are preferred for erosion resistant applications [42]. Additionally, studies have revealed superior microstructural and

mechanical properties contributing to erosion resistance can be achieved by implementing WC-Co coatings deposited via HVOF processes rather than plasma or low velocity combustion techniques [41].

2.4 Thermal Spray Required Properties

TS coatings are typically applied to components where high wear/erosion resistance is required to provide an acceptable service life. Particularly, oil exploration efforts subject components to extremely harsh erosive environments, where the component must resist wear to prevent additional maintenance downtime and premature failure. Besides being extremely erosive, the drilling environment also contains elevated temperatures and drilling mud additives creating a corrosive environment. The required coating properties are elaborated on in the remainder of this section to aid in the depiction of the required properties of a high quality TS coating.

2.4.1 Microstructural Properties

The coating microstructure is typically a good indicator to the quality of the coating, where a polished cross-section of the coating is observed using an optical or electron microscopy. In general terms the microstructure consists of lamellar splats, with grains of WC and secondary phases embedded in a Co rich matrix [43]. In addition to structure coating porosity is also a good indication of the quality. For HVOF coating the porosity should also be relatively low (< 1 %) due to the thermal particle softening and high particle velocity during coating deposition. Coating porosity can also be referred to as voids within the coating and can be interpreted as coating defects, where the particles were not sufficiently thermally softened or had insufficient velocity to splat and effectively interlock with the previously deposited splats. These defects can be classified into the following

three prime void morphologies; inter-lamellar pores, inter-lamellar cracks, and delamination features, as well the voids can be classified based on void connectivity within the coating microstructure, which can be divided into a closed void network or an open void network [44]. A closed void network is used to describe the condition where the voids are not connected and reside within the interior of the structure, where an open void network accounts for all the pores and cracks are connected to the coating surface. The final characteristic of the microstructure to note is the coating/substrate interface. This interface is the foundation for the adhesion of the entire coating, where mechanical interlocking is the dominating factor of coating adhesion, suggesting the interface should be sufficiently roughened by a process that does not promote particle embedment, as embedded particles have been suggested to act as stress-risers at the coating/substrate interface [19] as mentioned previously in the literature review.

2.4.2 Physical Properties

The physical properties of a TS coating are the most influential to the coatings overall performance, with the adhesion strength being one of the most important parameters. The coating adhesion is crucial due to the nature of the drilling environment where drill cutting rock fragments impact the coating, which can lead to detrimental spalling or delamination of the coating, causing substrate exposure leaving the substrate vulnerable to rapid erosion. Since no metallurgical bonds are formed between the rapidly cooling deposit and the substrate, the surface finish and the deposition conditions during the first spray pass are of uttermost importance in obtaining good adhesion [1]. The erosion/wear resistance of TS coatings are also of high importance and typically is an intrinsic property of the coatings adhesion strength, hardness. Due to these requirements

TS coatings must be; extremely erosion resistant, have strong adhesion to the substrate, and hard while maintaining ductility.

2.4.3 Thermal Properties

In order for a TS coating to be effective in the drilling industry it must have a high maximum operating temperature to prevent premature failure. During drilling the coating will be subjected to thermal stresses from drilling operation itself, as well as geothermal heating based on the drilling depth, and heating due to the drilling process. Figure 25 represents the temperature and pressure categories for drilling environments ranging from low pressure low temperature (LPLT) to ultra-high pressure high temperature (Ultra HPHT). From Figure 25 it can quickly be recognized that the operating temperature during drilling can range from 25 – 500 °F, which signifies the importance to develop a TS coating with a high operating temperature.

2.4.4 Magnetic Properties

During HDD the drill head can be directed by the drilling engineer at the surface, this is achieved by the implementation of a magnetometer and inclinometer located near the drill head. The magnetometer is used to measure the strength and direction of the magnetic field at predetermined space, while the inclinometer is used to measure the inclination of the chassis relative to the north vector, otherwise known as the azimuth. The feedback from these instruments allows for accurate orientation of the drill head, but magnetic interference can result in significant errors in the azimuth angle making accurate drilling relatively difficult [45]. Therefore it is important that the chassis containing the magnetometer and inclinometer as well as the protective coating applied to the chassis must be magnetically transparent.

2.4.5 Chemical Properties

Although drilling mud typically consists of water and bentonite, additives are also commonly introduced to control the density, wettability and foam formation of the drilling fluid. These agents can include; alkalinity agents, de-foaming agents, shale and clay stabilizers, thinners/dispersants, wetting agents, viscosifiers and weighting agents. In addition to drilling additives, hydrogen sulfide (H_2S) has been found to be produced during drilling operations and diffuses into drilling fluid, due to sulphate reducing bacteria (SRB) in sea water or in formation water (connate water) under anaerobic conditions where the SRB grow with organic materials such as crude oil as a substrate [46].

Additionally, the desired target values for mechanical properties have been summarized in Table 3, which will be highlighted in the corresponding result plots.

2.5 Testing Methods of Thermal Spray Coatings

This section introduces the standard testing procedures used by the American Society for Testing Materials (ASTM) as well as researchers within the field to characterize and evaluate HVOF TS coatings.

2.5.1 Coating Porosity

Coating porosity characterization can be implemented to quantify the area porosity based on the light reflectivity from a metallographically polished cross-section of the coating. Care should be taken during polishing to avoid the introduction of artifacts or particle pull-out, therefore semi-automatic polishing equipment is highly recommended. Once the cross-sections are properly prepared an image of the cross-section can be captured and post processed using an image analysis software such as ImageJ to convert the image

into a binary mask of the initial image, which will allow the area porosity to be determined as the fraction of black pixels to the white pixels in the image, where black pixels represent voids. For reference an example has been added of the binary mask of a coating cross-section containing 1.0 % porosity by area from ASTM E-2109-14, shown as Figure 26.

2.5.2 Coating Density

The coating density of a TS coating is typically measured for quality control and can be used in addition to or instead of porosity measurements, by applying ASTM B962-15. The implementation of this measurement may be considered more practical than porosity measurements as metallographic sample preparation are not required and the sample can be tested in essentially the as-sprayed condition. This test method can also be easily applied to irregular shaped parts, due to the fact the density is calculated using Archimedes principle of buoyancy.

Although the test method was developed to calculate the density of compacted or sintered powder metallurgy products, the method can easily by applied to TS coatings by carefully removing the coating substrate via wire electric discharge machining (EDM) or using a dilute acid to dissolve the substrate, which is chemically inert to the coating.

To conduct this test the following equipment will be required; vacuum impregnation apparatus, a precision single-pan balance that will permit readings within 0.01 % of the test specimen mass, thermometer with an accuracy of 0.5 °C, a glass beaker to contain water, a test specimen support apparatus such as a suspension wire to suspend the sample (selection of wire diameter is relative to specimen weight which can be determined from Table 1) within the water without contacting the glass beaker, and a

beaker support apparatus to support the beaker above the balance pan without contacting the pan, as represented in Figure 27.

2.5.3 Hardness Testing

The Rockwell hardness test is an empirical indentation hardness test referred to as ASTM E18-12, which can provide useful information about metallic materials, which may correlate to tensile strength, wear resistance, ductility, and other physical properties [47]. This test is also extensively used to monitor quality control of high and low production products. The test involves an indenter being brought into contact perpendicular to the test surface, which should also be perpendicular to equipment stage. A preliminary force is then applied for the specified dwell time and the baseline depth of indentation is measured. The test force is then applied at a controlled rate, which is also held for a specified dwell time, after which is removed and the final depth of indentation is measured and the hardness is calculated. Modern Rockwell testers are automated to apply the set loads for dwell times automatically, resulting in extremely effective and repeatable hardness testing. It should be noted that prior to testing any samples a calibration test should be conducted on a calibration block at the intended Rockwell scale to ensure the equipment is operating properly and upon completion of testing an additional calibration test should be conducted to confirm the accuracy of readings throughout the testing process.

2.5.4 Adhesion Testing

The adhesion strength of a TS coating can be determined according to ASTM C633-13, which covers the determination of adhesion (bond strength) of a coating to a substrate or the cohesion strength of the coating, when the coating is subjected to uniaxial tension normal to the coated surface. A coated button in secured between the top and bottom of the

loading fixture (Figure 28) via a suitable adhesive with an adhesive strength at least as great as the minimum required adhesion and cohesion strength of the coating, in the case of HVOF TS coatings FM 1000 aircraft grade adhesive is typically used due to its strong adherence of approximately 10 000 psi (69 MPa) [18]. Upon curing the loading fixture with coated button sandwiched in the middle is lightly sanded to remove any excess adhesive on the outer edge of the button or loading fixture, installed into a uniaxial tensile testing machine, then the cross-head is displaced at a constant rate between 0.013 mm/s to 0.021 mm/s to apply a tensile load until fracture occurs. Where the maximum tensile load represents the adhesive strength, which can be divided into the following three failure categories; adhesive failure, cohesive failure, or delamination failure. An adhesive failure signifies the bonding adhesive between the coating and the loading fixture has failed which signifies the coating adhesion is as strong as or stronger than this recorded value and a stronger adhesive may be required if possible. A cohesive failure represents failure within the coating, typically occurring between lamellar layers, which will result in fragments of the coating on each side of the fracture surface. Finally the delamination type failure represents a failure where the entire coating has been delaminated from substrate, suggesting the pre-spray surface roughening may not be sufficient.

2.5.5 Erosion Testing

Erosion testing can be perceived as a very general term, as erosion can occur under many conditions with varying; impact velocity, suspension mediums, erodent particles, and erodent impact angles. In general, erosion can be quantified as the plot of the cumulative volume loss versus cumulative exposure time. The rate of liquid impact erosion is not constant with time, but exhibits three distinct regions; incubation period, maximum erosion

rate, and a “terminal” steady-state rate. The most common pattern consists of an incubation period which material loss is slight or absent, followed by an acceleration of erosion rate to a maximum value, in turn followed by a declining erosion rate which may or may not reach steady-state, which is graphically represented in Figure 29 [48]. From this plot the maximum volumetric erosion rate (Q_e) and the terminal erosion rate (Q_t) can be determined. The maximum volumetric erosion rate can be determined by the slope of the actual or effective straight line through the linear portion of the steepest section of the plot, while the terminal erosion rate is the slope of steady-state portion of the curve.

For the purpose of this research, erosion testing was required to simulate drilling conditions on a laboratory scale via slurry jet erosion testing rig, which utilized repeated impact erosion involving a small nozzle delivering a stream of gas or liquid containing abrasive particles which impact the surface of a test specimen. Since erosion can be quantified through many avenues the review and combination of multiple standards and research papers was required to develop the system and procedures required for this specific research [49], [48], [50], [51] & [52]. This included the development of a water and bentonite based drilling fluid, which could be used as a suspension medium for erodent particles, along with the design and fabrication of a solid particle erosion testing rig. From the available research three potential types of testing rigs were reviewed, which included a recirculating slurry testing rig, a semi recirculating slurry testing rig, and a non-recirculating slurry testing rig, which are schematically represented as Figure 30, Figure 31, & Figure 32, respectively. Each of these types of testing rigs have individual pros and cons, but based on the feasibility of construction and versatility of application the recirculating slurry testing rig was selected for this research. This is based on the fact that

the recirculating slurry testing rig has a relatively simple design with nozzles that can be easily replaced as they wear, as well the erodent particle concentration and size can quickly be changed by simply adding more erodent particles to the slurry storage tank and installing nozzles with the appropriate orifice diameter.

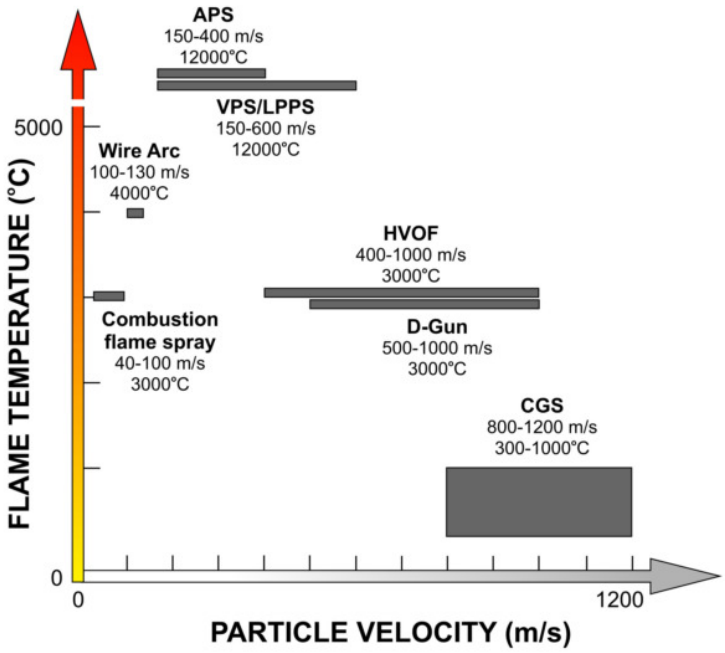

Figure 1 - Typical flame temperature and particle velocity operation ranges for various TS systems [1].

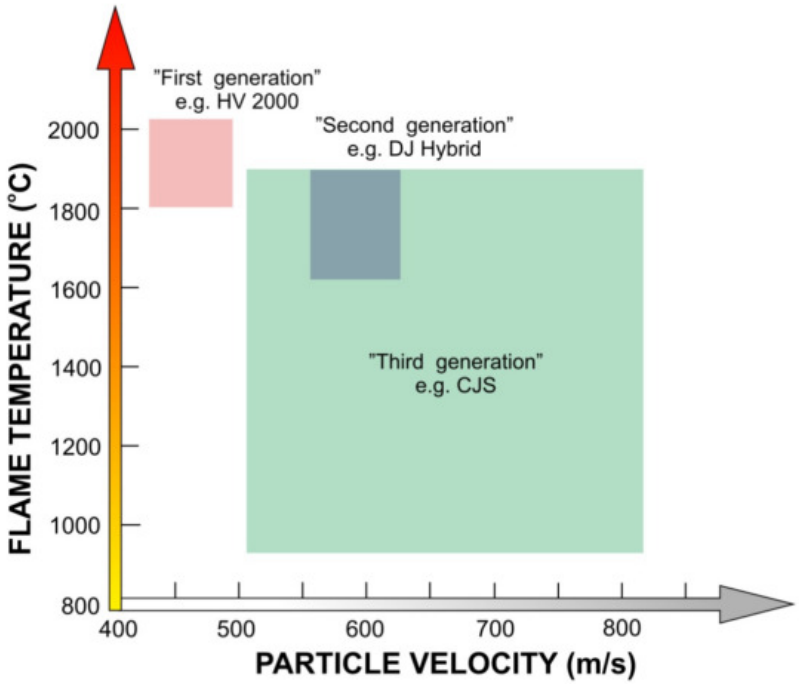

Figure 2 - Progression of particle temperature and velocity capabilities of HVOF generations [1].

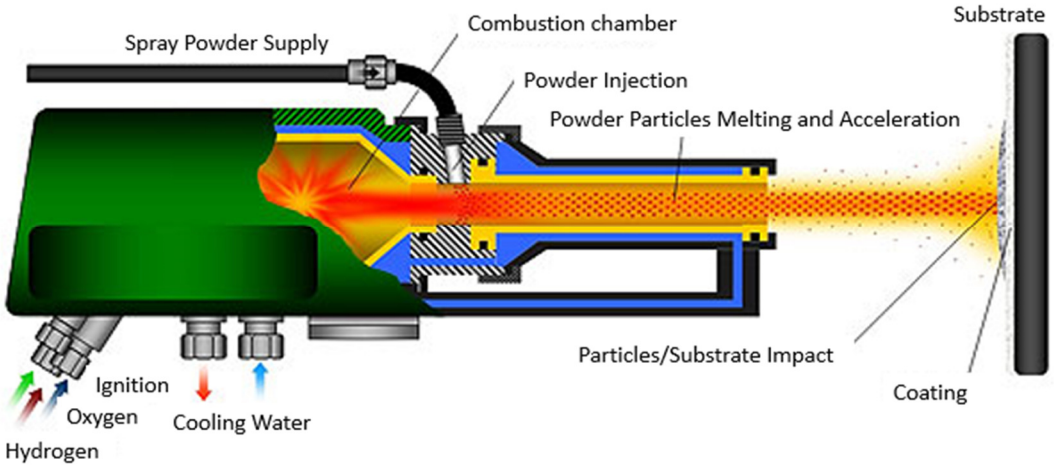

Figure 3 - HVOF spray torch schematic [53].

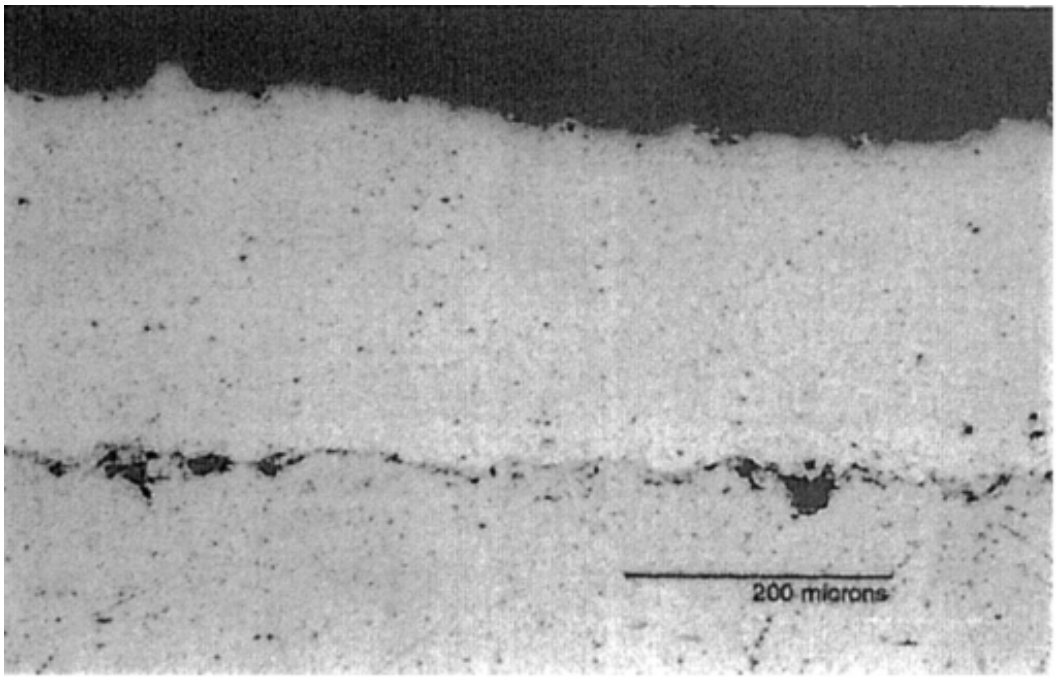

Figure 4 - Polished cross-section of grit blast roughened Mar-M 509 coated with MCrAlY, where grit inclusions are observed at the interface [19].

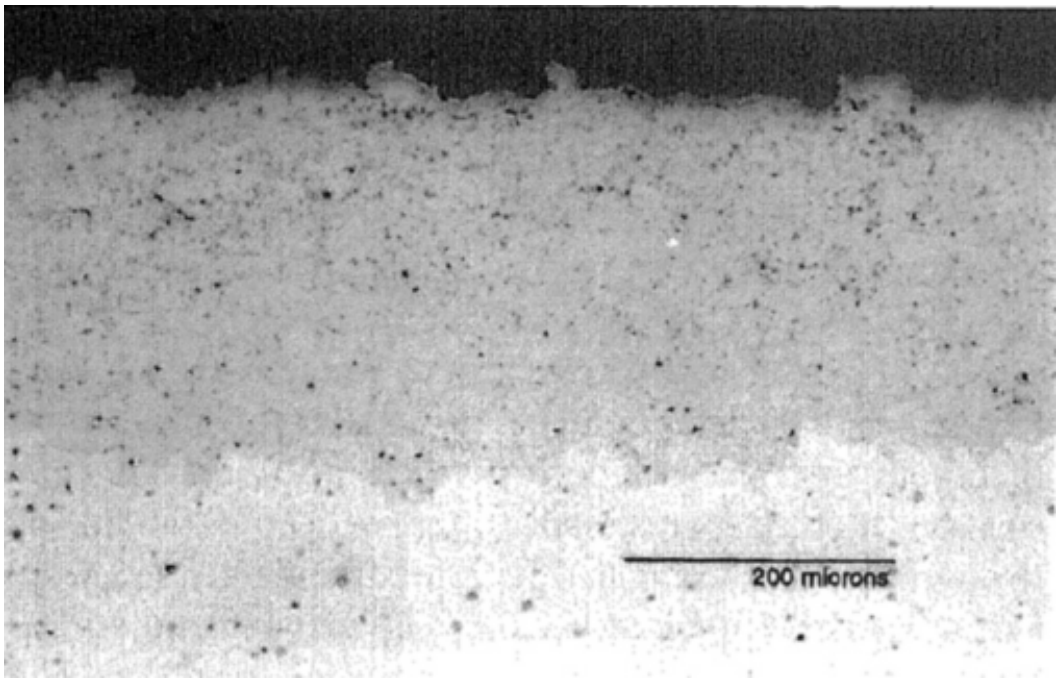

Figure 5 - Polished cross-section of waterjet roughened Mar-M 509 coated with MCrAlY [19].

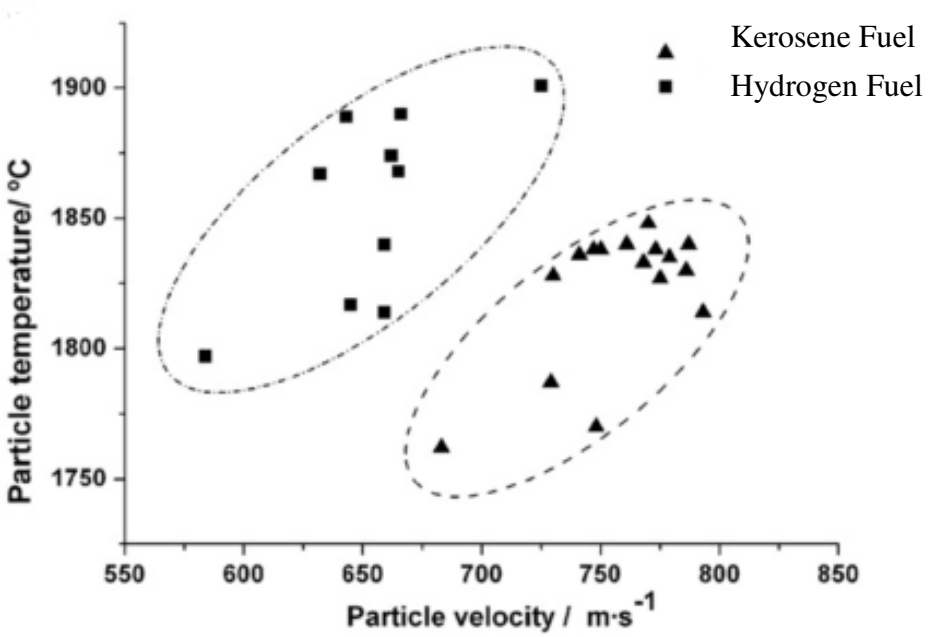

Figure 6 - Evolution of particle temperatures and velocities for two different fuel/oxygen mixtures [21].

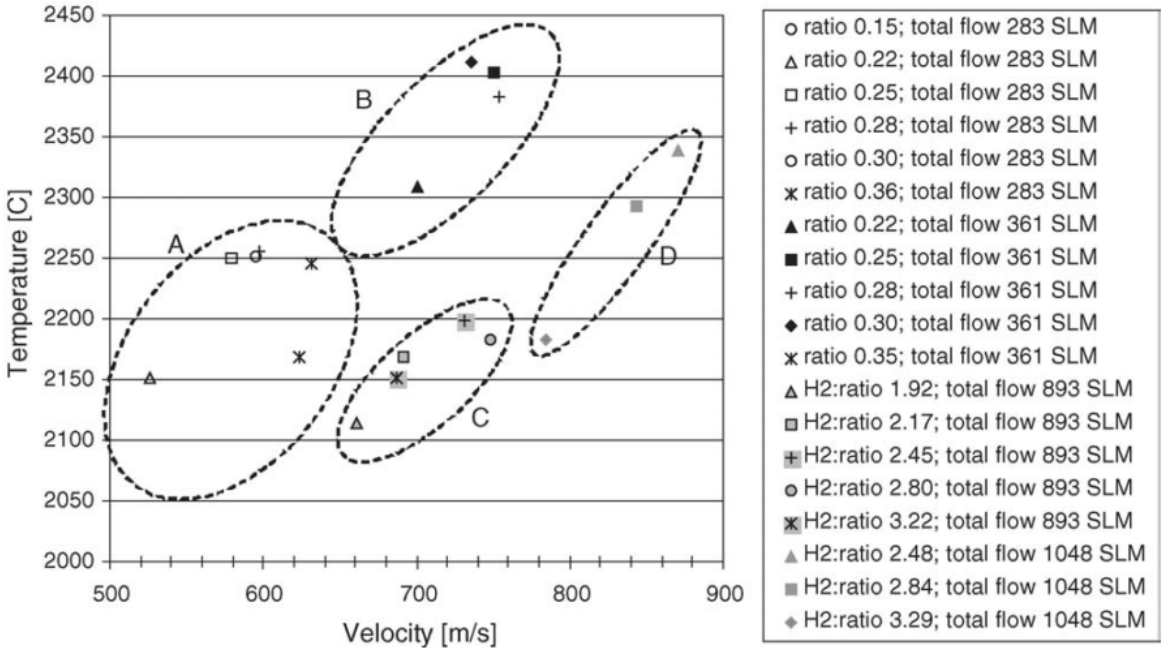

Figure 7 - Process diagnostic data for different spray parameter combinations for Propylene-Oxygen flame and Hydrogen-Oxygen flame [22].

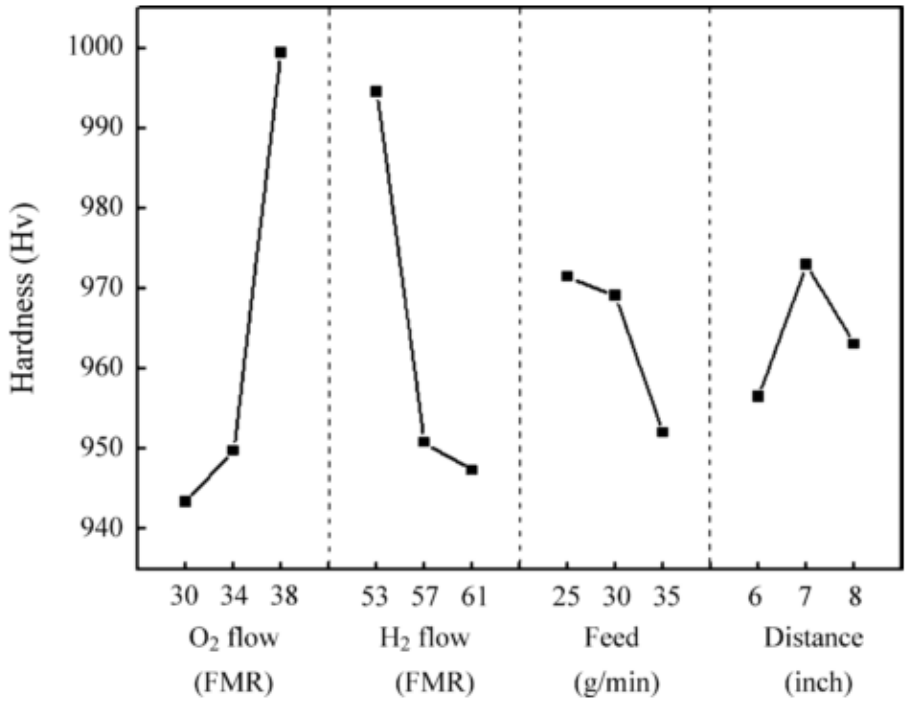

Figure 8 - Influence of deposition parameters on hardness of WC-Cr-C-Ni coating [54].

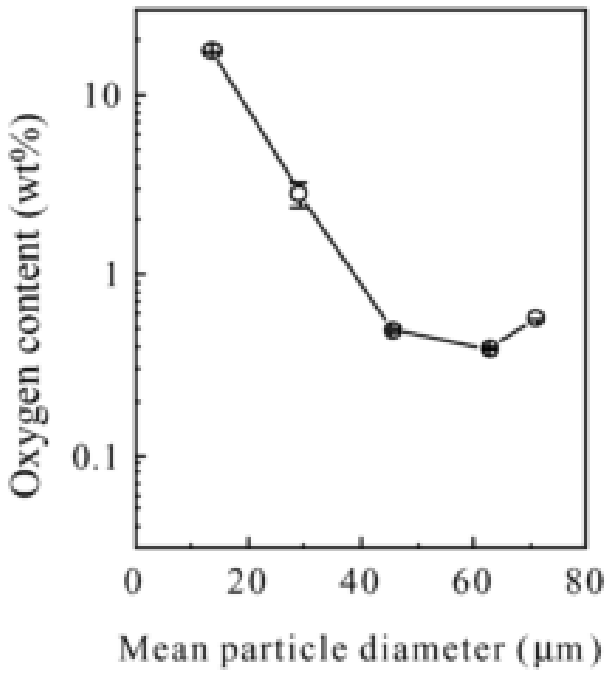

Figure 9 - Effect of particle size on the oxygen content in HVOF Ni-Cr-AL-Y coatings [28].

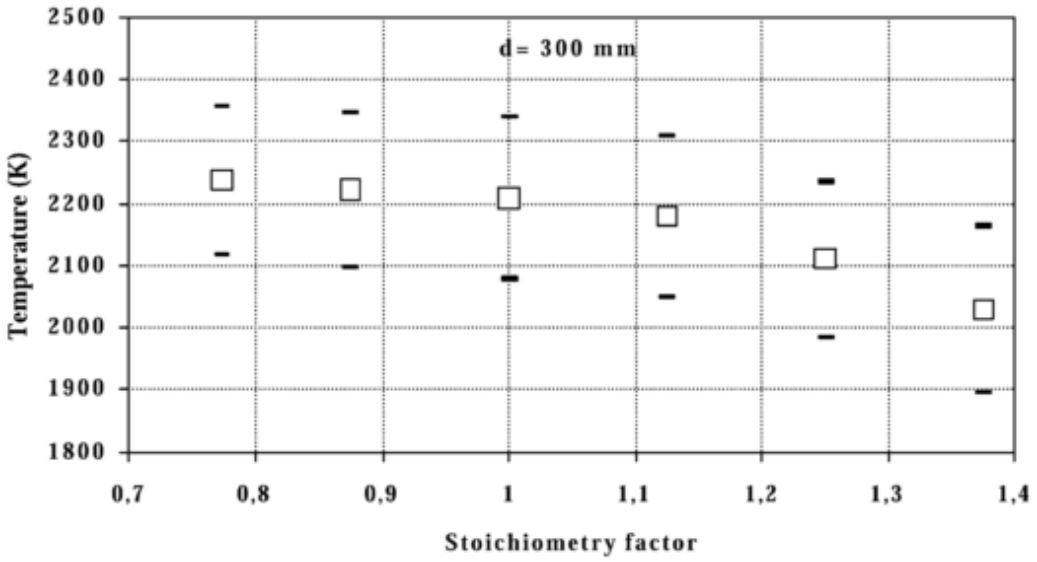

Figure 10 - Evolution of particle temperature vs. the stoichiometric factor (spray distance: 300mm, Fuel: Natural gas) [30].

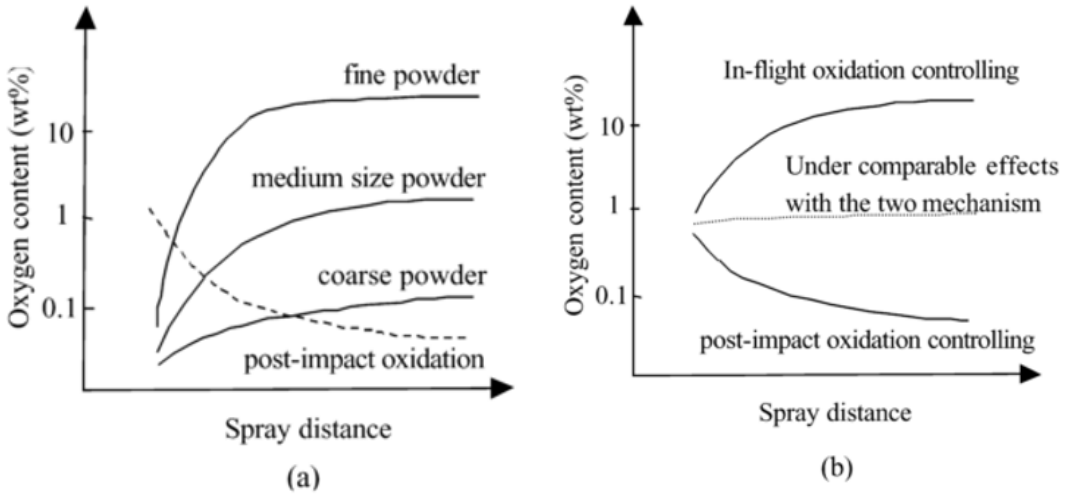

Figure 11- Schematic diagram of dependency of oxygen content in the coating on spray distance in two oxidation mechanisms. (a) effect of a single mechanism and (b) combined effect of two oxidation mechanisms [28].

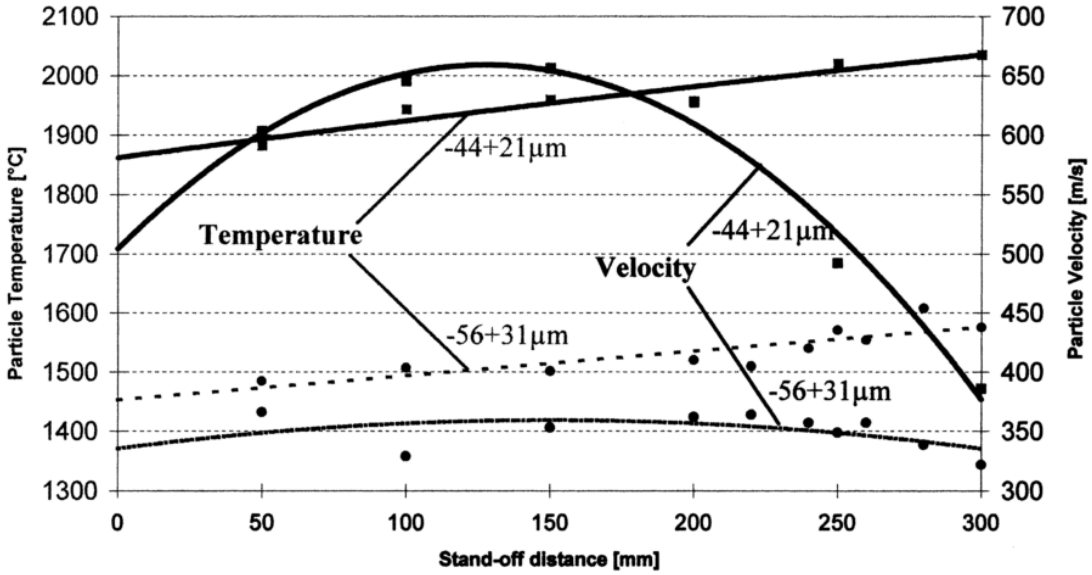

Figure 12 - In-flight particle properties as a function of spray distance and particle size [15].

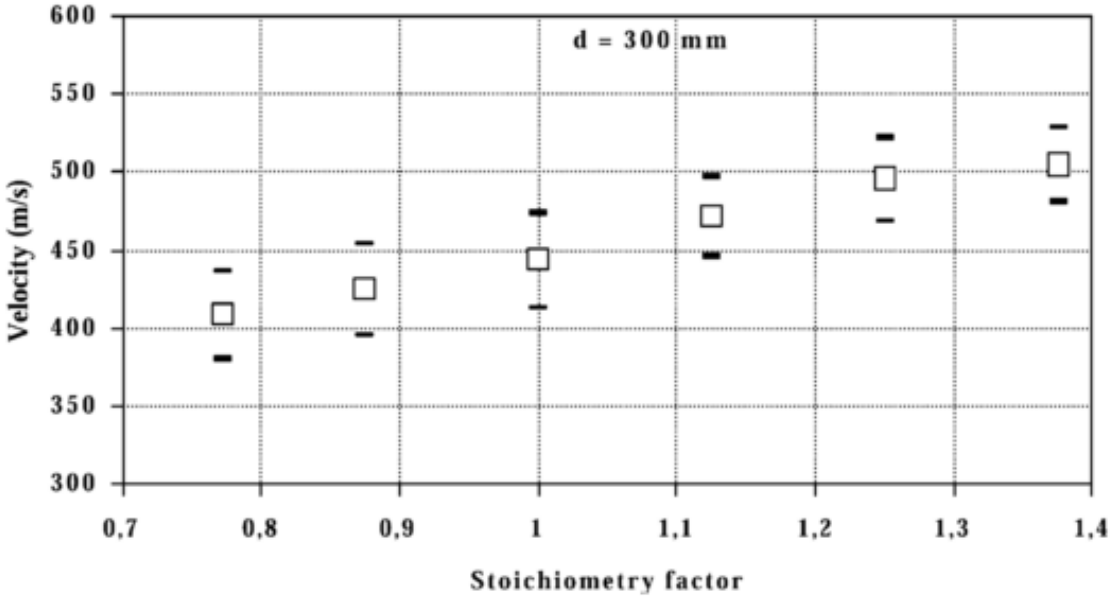

Figure 13 - Evolution of particle velocity vs. the stoichiometric factor (spray distance: 300 mm, Fuel: Natural gas) [30].

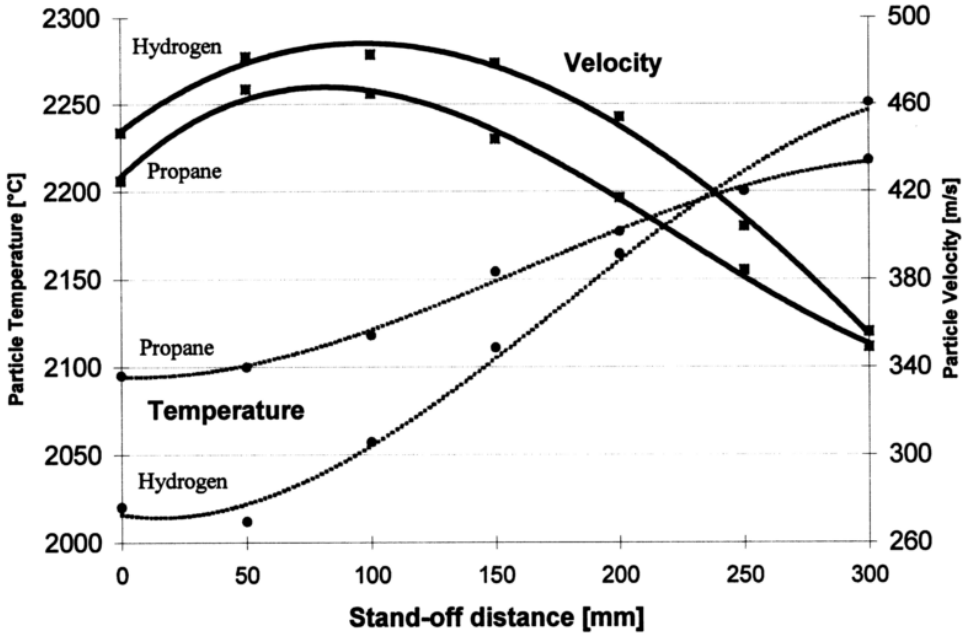

Figure 14 - In-flight particle properties as a function of spray distance and fuel gas [15].

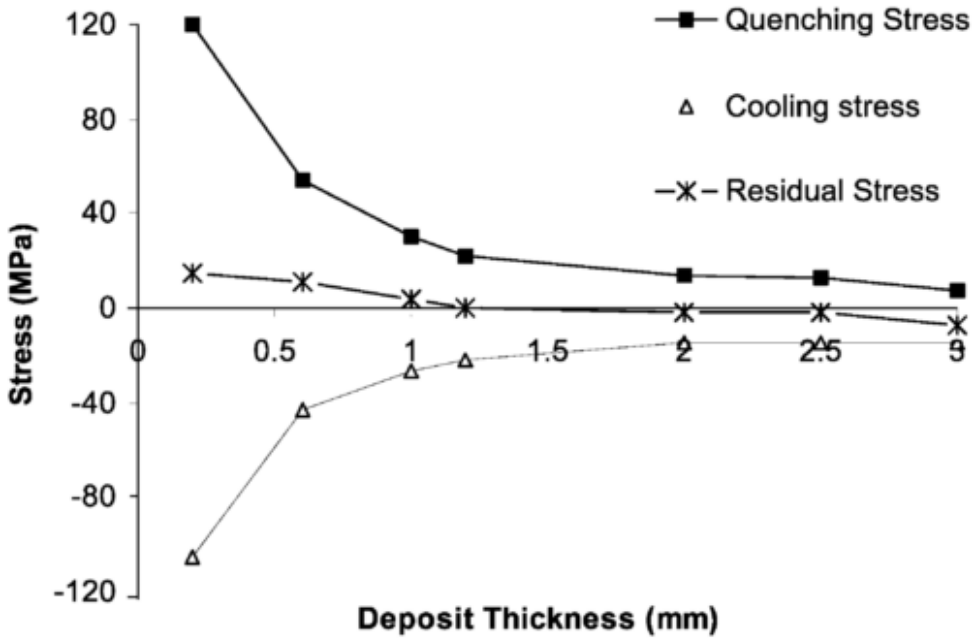

Figure 15 - Quenching, cooling, and residual surface stresses as a function of deposit thickness, with forced cooling [32].

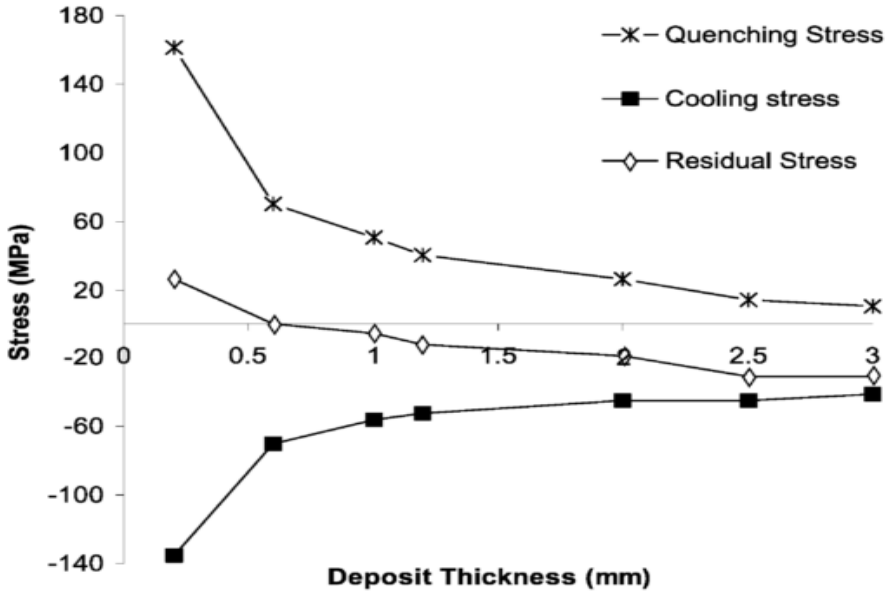

Figure 16 - Quenching, cooling, and residual surface stresses as a function of deposit thickness, without forced cooling [32].

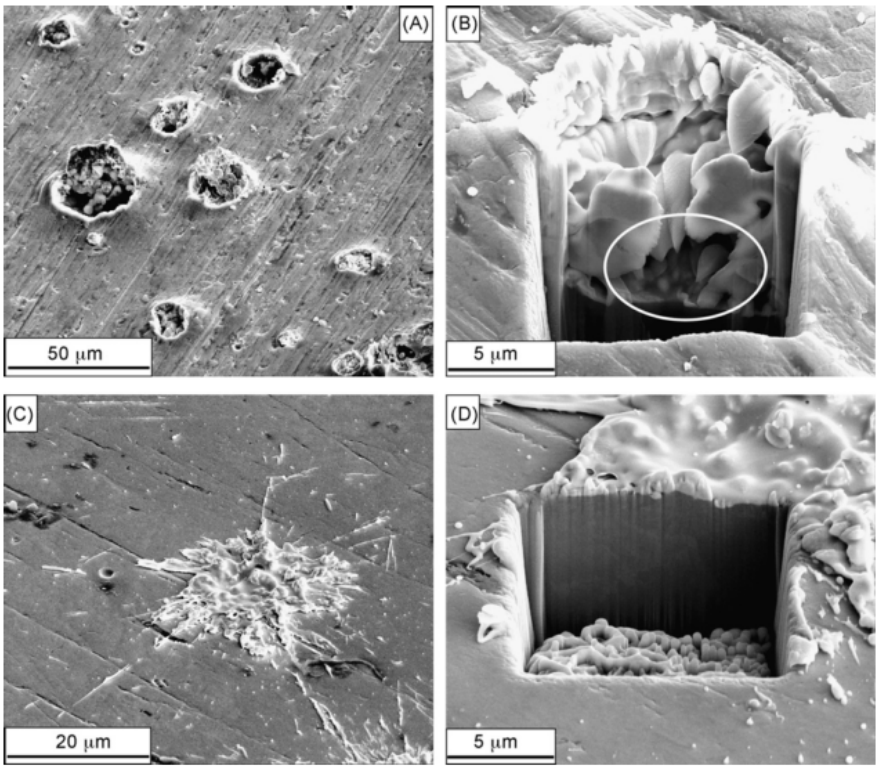

Figure 17 - SEM micrographs of single Wc-CoCr splats on Al and steel surfaces: (a) splats on Al surface; (b) FIB section of feedstock splat on AL surface, highlighting small defects (circle); (c) splat on steel surface; (d) FIB section of the splat on steel surface [33].

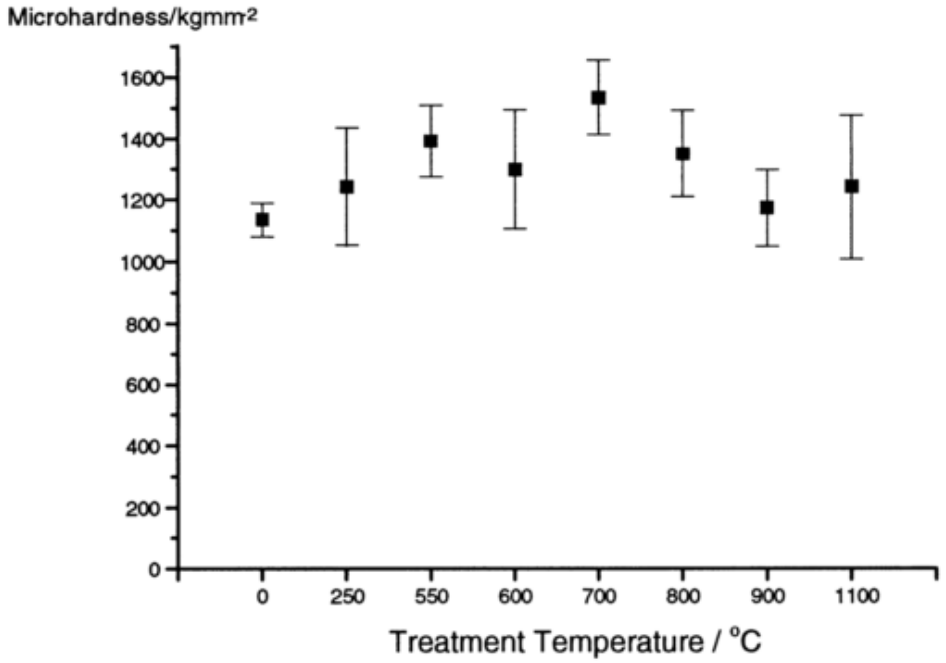

Figure 18 - Plot of coating hardness against heat treatment temperature (error bars represent one standard deviation) [34].

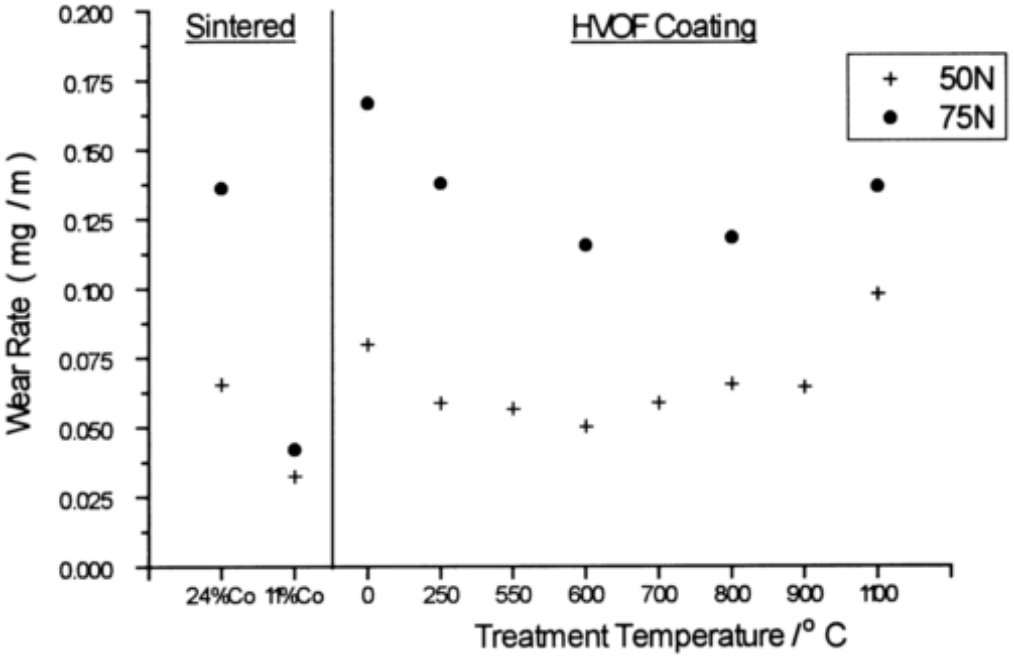

Figure 19 - Plot of coating steady-state wear rate against heat treatment temperatures for two applied loads, along with wear rates for sintered cermets using a modified dry sand rubber wheel technique [34].

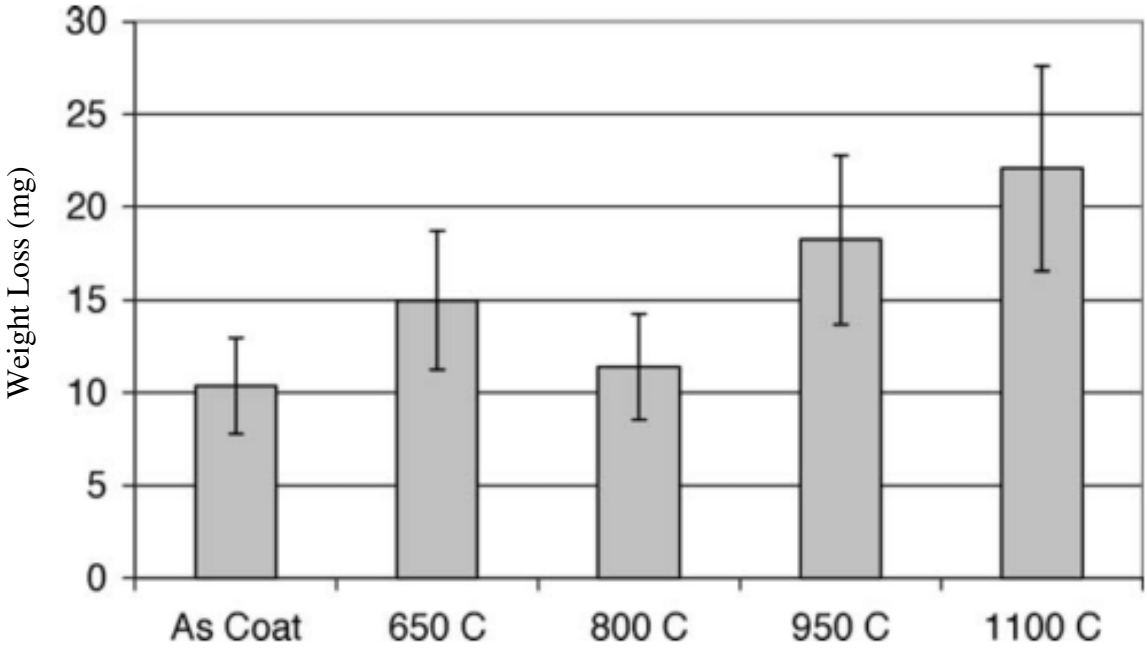

Figure 20 - Variation of the weight losses of the coated samples vs. the heat treatment temperature using a pin on disk tribometer (sliding speed 0.1 m/s, load 5 N, and sliding distance of 100m) [36].

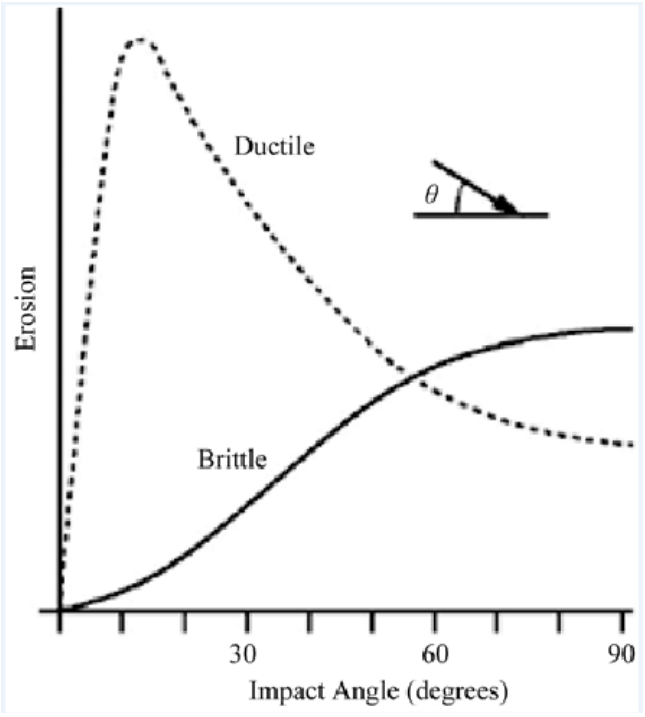

Figure 21 - Typical dependence of erosion on impact angle θ (defined as the angle between impact direction and the surface) [39].

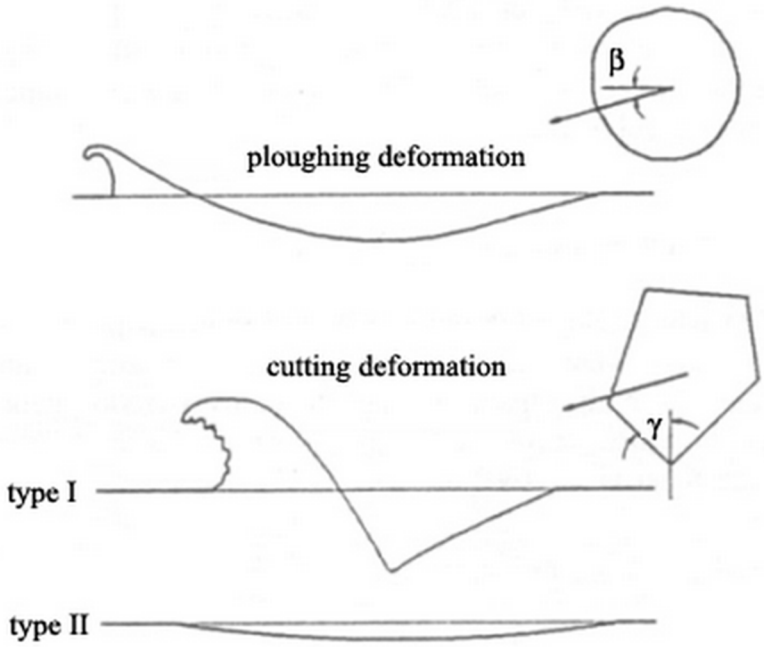

Figure 22 - Solid particle erosion wear mechanisms.

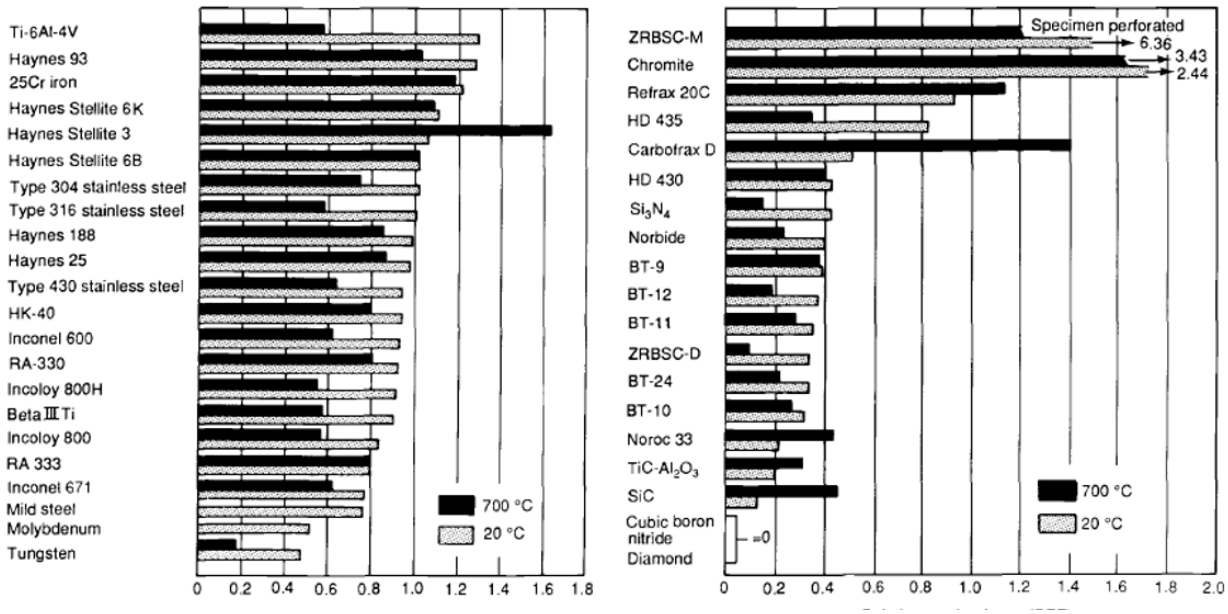

Figure 23 - Relative erosion factors for selected metals and ceramics [40].

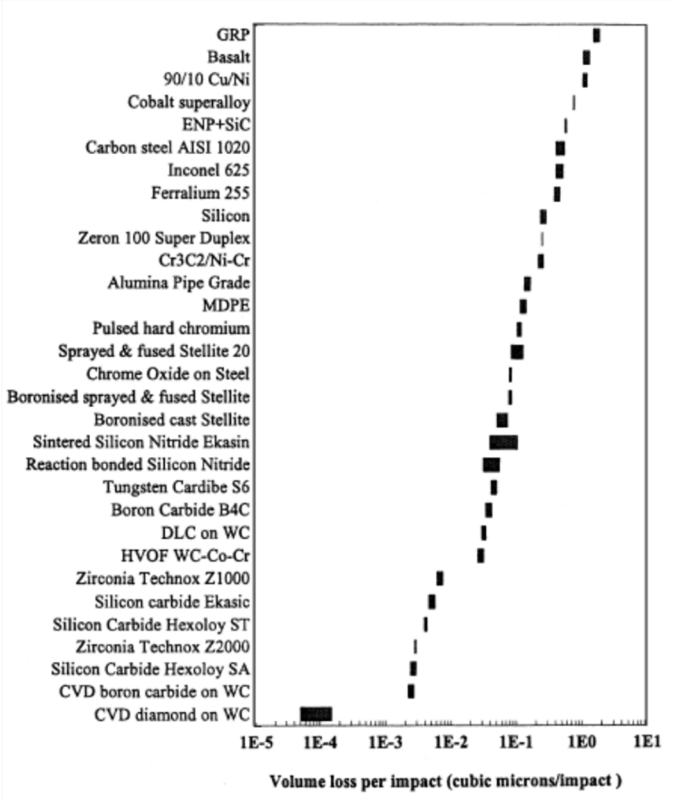

Figure 24 – Erosion test results (low energy sand slurry jet impingement using 135 µm sand at 2.25 wt.% concentration in water at 16.5 m/s and 90° impingement angle) of coated carbon steel with tungsten carbide compared with bulk erosion resistant materials [55].

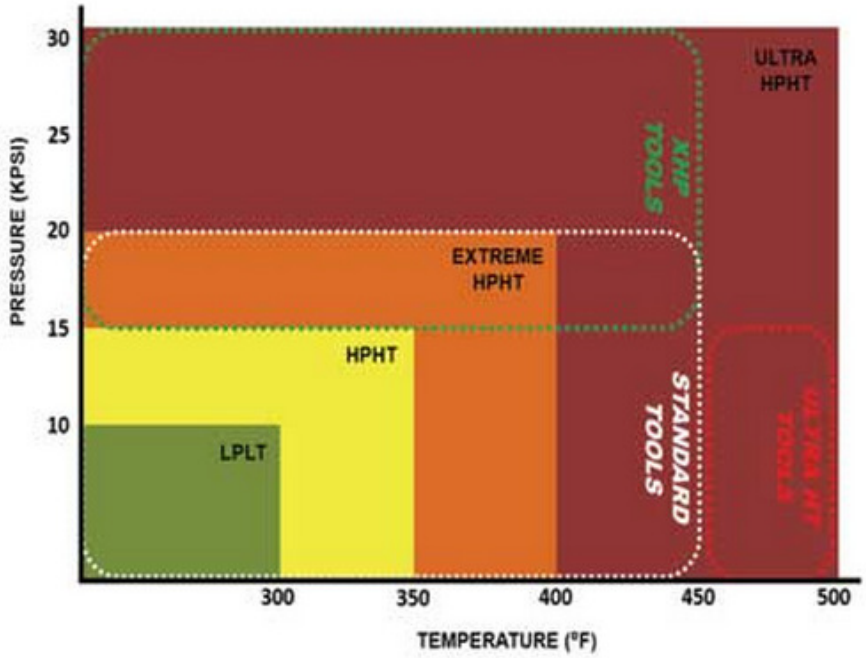

Figure 25 - Pressure and temperature categories of drilling environments, where LPLT stand for low pressure low temperature and HPHT represents high pressure high temperature [56].

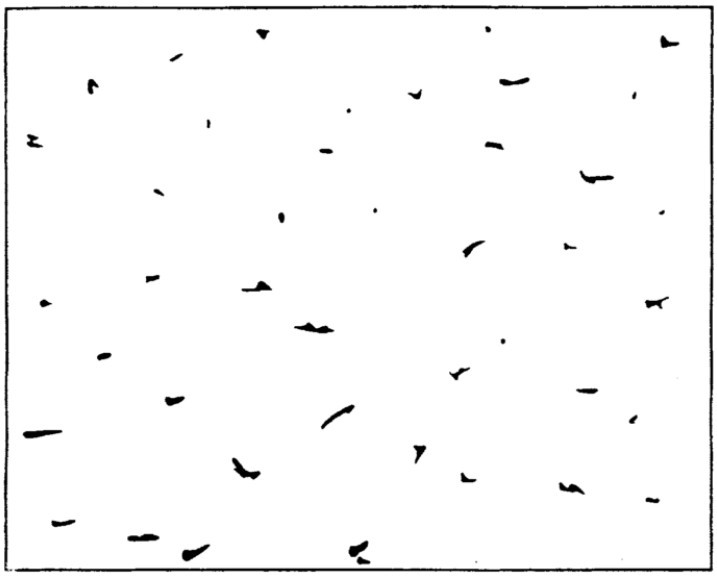

Figure 26 - Example of binary mask of coating cross-section containing 1.0 % porosity by area [57].

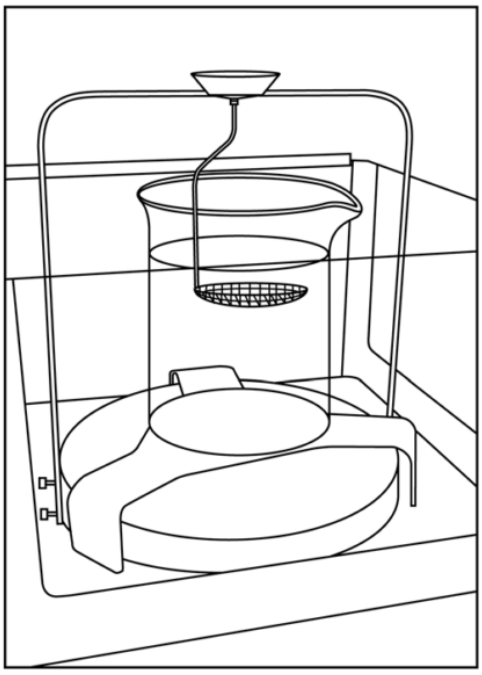

Figure 27 – Beaker support above balance pan schematic, according to ASTM B962 [58].

Table 1 - Maximum recommended wire diameter for specimen suspension apparatus [58].

Mass, g	Wire Diameter, in. (mm)
less than 50	0.005 (0.12)
50 to less than 200	0.010 (0.25)
200 to less than 600	0.015 (0.40)
600 and greater	0.020 (0.50)

Table 2 – Effect of temperature on the density of air-free water [58].

Temperature		Density
°F	(°C)	g/cm^3
59.0	(15)	0.9991
60.8	(16)	0.9989
62.6	(17)	0.9988
64.4	(18)	0.9986
66.2	(19)	0.9984
68.0	(20)	0.9982
69.8	(21)	0.9980
71.6	(22)	0.9978
73.4	(23)	0.9975
75.2	(24)	0.9973
77.0	(25)	0.9970
78.8	(26)	0.9968
80.6	(27)	0.9965
82.4	(28)	0.9962
84.2	(29)	0.9959
86.0	(30)	0.9956

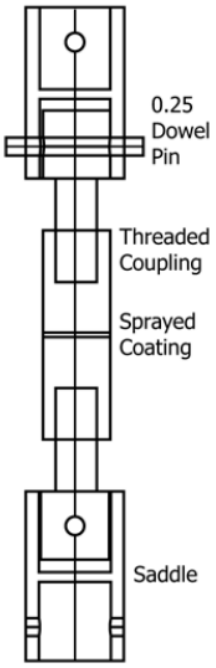

Figure 28 - Schematic of self-aligning adhesion testing fixture [18].

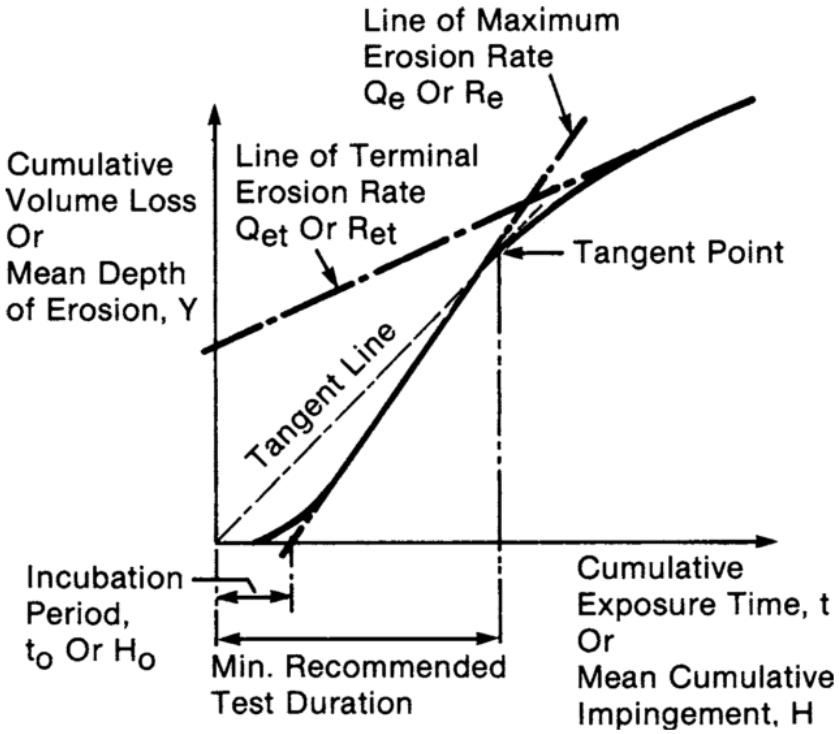

Figure 29 - Typical erosion-time pattern and parameters used to quantify SPE erosion[48].

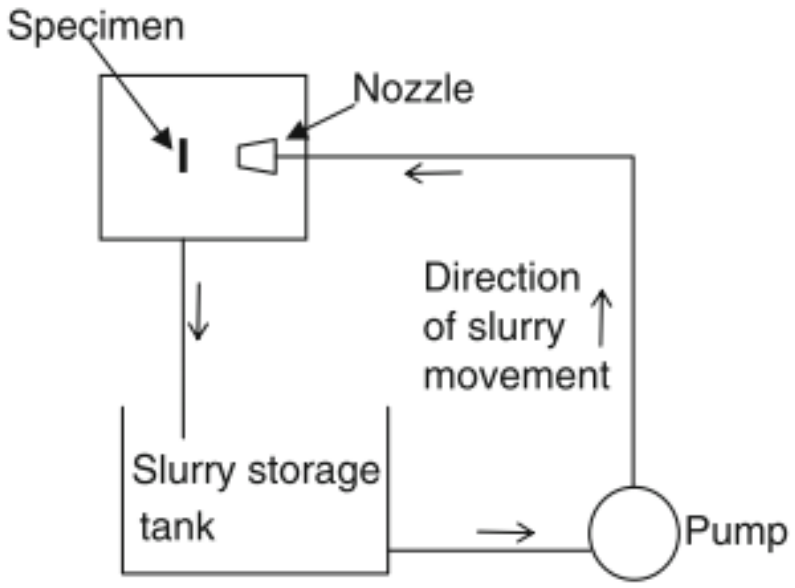

Figure 30 – Schematic of high-velocity recirculating slurry testing rig [52].

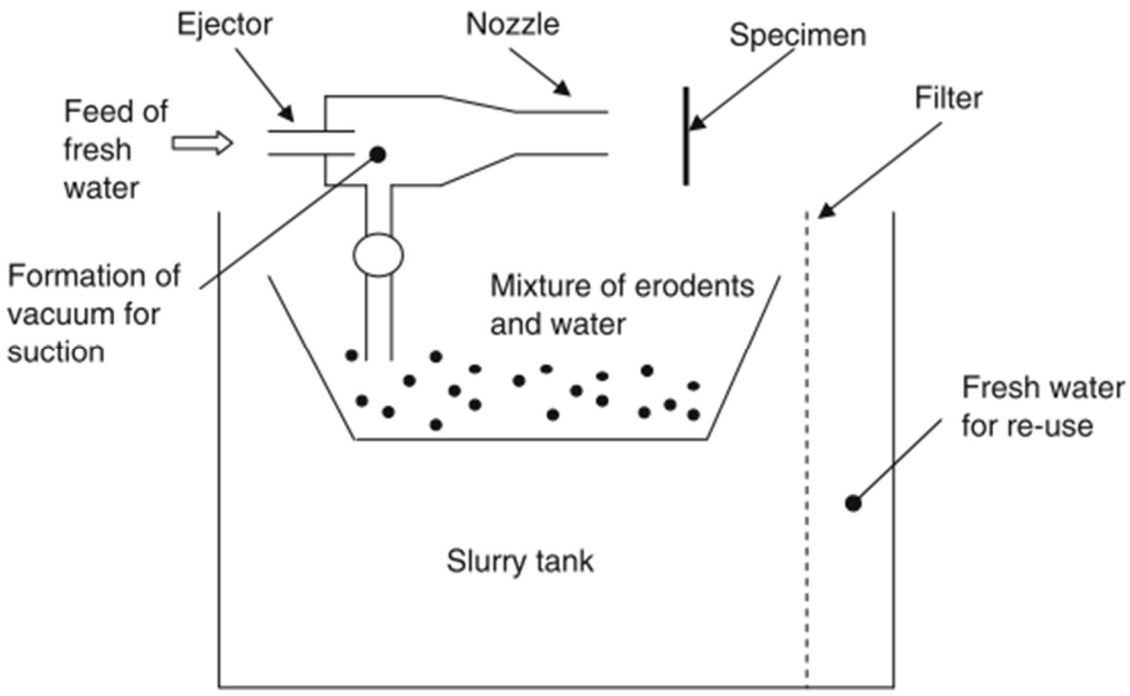

Figure 31 – Schematic of high velocity semi recirculating slurry testing rig [52].

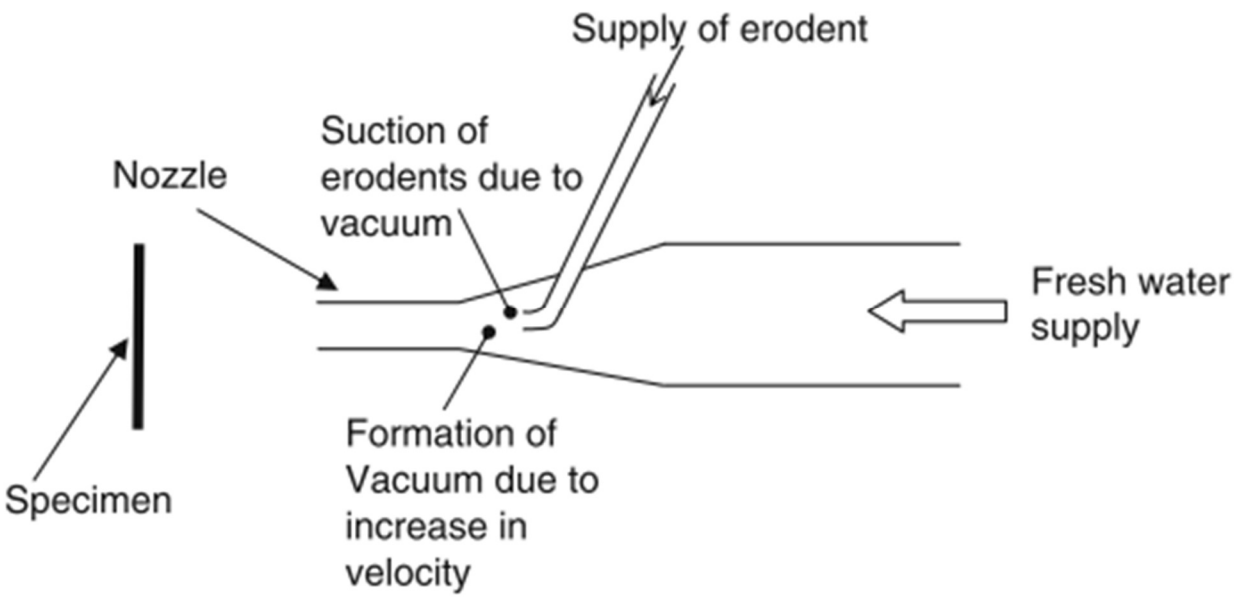

Figure 32 – Schematic of high velocity non recirculating slurry testing rig [52].

Table 3 – Summary of desired coating mechanical properties target.

Mechanical Property	**Target Value**
Coating Porosity	< 1%
Coating Adhesion Strength	≈ 69 (Mpa)
Coating Hardness	≈ 80 (HRA)

Chapter 3: Material and Experimental Methods

Chapter three provides an outline of the materials and experimental procedures used to characterize the microstructural and mechanical properties of TS coatings, including porosity, density, hardness, coating adhesion strength, and erosion resistance. As well as the design parameters of the solid particle recirculating slurry erosion tester design and built for the purpose of this research. The chapter also elaborates on the coating characterization techniques used in this study.

3.1 Coating Feedstock

The main feedstock powder investigated was amperit 558 (WC-Co-Cr) produced by H.C. Starck was supplied by SharkSkin Coating for particle size and morphology observation under scanning electron microscope (SEM) and elemental composition under energy-dispersive X-ray spectroscopy (EDS). The feedstock is a versatile, high quality powder with fine WC particles well distributed in the cobalt-chromium matrix. The composition of the feedstock as represented by HC Stark is as follows; 86 % by mass WC, 10 % wt, Co, and 4 % wt Cr, with maximum Iron (Fe) and Oxygen (O) of 0.3 % wt and 0.2 % wt, respectively.

3.2 Sample Substrate

The substrate selected for the purpose of this research was a Cu-Ni-Sn alloy commonly referred to as Toughmet, with the following composition; Cu 69.95-76.7 % wt, Ni 14.5-15.5 % wt, and Sn 7.5-8.5 % wt. The alloy is spinodally hardened, which provides excellent machinability and good dimensional stability, achieved by high-temperature solution treatment, quenching, and ageing. The spinodal-hardening mechanism results in chemical

segregation of the alpha crystal matrix on a very fine scale. Since no crystallographic changes take place during spinodal-hardening, alloys retain excellent dimensional stability during hardening. The toughmet samples are machined from one inch bar stock and sectioned into 0.25 inch disks or “buttons”, which the coating can then be applied to, which can be seen in Figure 34.

The substrates are coated with the coating feedstock using HVOF TS deposition with a coating thickness of approximately 220 (um). Upon receiving samples, each sample was gently hand washed using soap and water, which was followed by an ultrasonic bath in ethanol. During shipping, the samples were individually wrapped in bubble wrap to avoid coating damage and stored at room temperature.

3.3 Coating deposition

3.3.1 Deposition Equipment

Coatings were deposited at SharkSkin Coatings state of the art facility, which is an ISO 9001 certified industrial partner. The coatings were deposited using HVOF Jet Kote III equipment, which implements Hydrogen and Oxygen fuel gas and Argon as the feedstock carrier gas. The HVOF torch is mounted on a computer controlled robotic arm to manipulate to position and orientation of the torch. Additionally, an air knife is mounted below the work piece approximately nine inches from the sample surface for forced conduction cooling during coating deposition, which is supplied with air from the building exterior, fitted with a 24 filter air purification system. The entire assembly is housed inside an acoustically dampened booth with a high powered exhaust system to exhaust torch fumes and reduce excessive chamber heating.

3.3.2 Deposition Procedure

After sectioning, each button was faced on a lathe to provide a flat machined finish and deburred using a belt sander. Two buttons were then placed into the custom fabricated mounting fixture and secured using a set screw located on the side of the button. The mounting fixture was then shielded, using a thin piece of sheet metal with two holes located at the sample location to prevent coating buildup on the fixture, but allowing for the buttons to be completely coated. The sample surface was then degreased using alcohol and wiped with a clean cloth to remove any remaining residue from sectioning. The sample surface was then mechanically roughened in a sand blaster, using 60 mesh aluminium oxide particles, cleaned using a compressed air gun to remove any remaining grit blasting particles, then cleaned using alcohol. The mounting fixture was then secured inside the booth, where the air knife was turned on. Once lit, the torch traverses horizontally completely across the work piece and then lowered three millimeters and traverses horizontally back to the initial side. This process is then repeated until the entire work piece is coated, indicating a single deposition cycle. The torch is then returned to the origin and the process is repeated an additional four times for the standard coating.

3.3.3 Standard Deposition Parameters

The coating was deposited onto two Toughmet coupons per run, prepared using the previously mentioned deposition procedure and the deposition parameters listed in Table 4.

3.3.4 Modified Deposition Parameter Procedure

This section outlines the modified deposition parameters in an effort to improve the coating performance. To determine the effect of individual deposition parameters, one

deposition parameter was modified from the standard coating parameters listed in Table 4 and then evaluated.

3.3.4.1 Pre-Spray Substrate Temperature

During the deposition process the torch was programmed to complete the desired number of pre-heating cycles, where the torch would pass over the sample with the particle feedstock feed was turned off. Immediately after the pre-heating cycles were completed the feedstock feed was turned on and the coating was deposited as the standard coating. This was completed for one and two preheating cycles, where substrate temperature was recorded after each successive pass.

3.3.4.2 Stand-off Distance

During coating deposition the torch was programmed to remain at a set stand-off distance which is the linear distance between the torch nozzle tip and the sample surface. The stand-off distance was modified in two inch increments from the standard (10”), which resulted in coatings with a stand-off distance of 12”, 10”, 8” & 6”.

3.4 Cross-Sectional Preparation and Microstructural Observation

To determine the microstructure of the TS coated samples, cross sections of the sampled were prepared using a low speed saw fitted with a 150 mm diameter circular diamond rotating at approximately 250 rpm with a dead load of approximately 500g. After sectioning each sample was gently washed using soap and water and cleaned in an ultrasonic ethanol bath for ten minutes to remove and remaining residue. Samples were then dried and mounted using VariDur 3000 20-3580 cold mounting epoxy in batches of three moulds. Each batch of samples was then polished using a Buehler MetaServ 250

semi-automatic grinder/polisher, using the parameters from ASTM E1920-14 [59], which were optimized for this particular coating and represented in Table 5. It should be noted that if only one sample was to be polished, it was manually polished using the same progression of grit paper as the semi-automatic process with a cross-section of a standard coating sample added into the mould for comparison to a semi-automatically polished cross-section to ensure the manually applied polishing pressure was not excessive, causing WC particle pullout.

The polished cross-sectional surface were observed using a light microscope as well as a scanning electron microscope (SEM) under high vacuum to determine the coatings microstructural characteristics and morphology, which is shown as Figure 35.

3.5 Coating Characterization Testing Procedure

3.5.1 Coating Thickness

The coating thickness was determined from optical and or SEM images of polished coating cross-sections, which were prepared using a semi-automatic polisher according to the parameters depicted in the previous section.

The images were individually imported into ImageJ, where the scale was set according to the image scale, which ImageJ converts the scale into terms of pixels per micron. Then ten lines were added along the coating cross-section and measured in length of pixels, which can then be converted into microns by using the ImageJ scale. The average length and standard deviation was then calculated from the ten measurements.

3.5.2 Coating Porosity

The coating porosity was determined from optical images of polished coating cross-sections according to ASTM E-2109, where the samples were prepared using a semi-automatic polisher according to the parameters depicted in the previous section. Once polished the sample cross-sections was observed using a light microscope, where the image was captured and processed using ImageJ. The image was cropped such that only the coating cross-section remained, the threshold was adjusted to remove the greyscale, resulting in coating pores appearing as dark pixels with the background as white pixels, then the image was converted to a binary mask (Figure 26) where dark pixels are converted to black and light pixels converted to white. The image particles were then analyzed using the "Analyze Particles" function within ImageJ, where the percent area is presented as a ratio of black pixels to white pixels, which translates into the coatings porosity by percent area. Note: upon conducting multiple analysis of an identical image an inherent statistical error is present due to the nature of processing images, this has been calculated to a standard deviation of 0.01 %, which will be applied to each porosity measurement.

3.5.3 Coating Density

The coating density of each sample was measured using Archimedes' principle according to ASTM B962 – 15, where three samples were sectioned using a low speed diamond saw to prevent damage to the coating. The substrate was then dissolved in a dilute nitric acid solution until only the undamaged coating remained. The sample was then thoroughly rinsed and ultrasonically washed in a soap solution then rinsed and washed in ethanol. The samples were then carefully dried, weighed, and deposited into an oil bath, where the samples were vacuum impregnated for 30 minutes and then rested in the oil bath

for an additional 30 minutes at atmospheric pressure to remove air and draw oil into pores within the coating. After vacuum impregnation the samples were removed from the bath and excess oil was gently wiped away from the sample surface and weighed again. Finally the sample was suspended in room temperature water using a wire suspension rig, which allows for the suspended coating to be weighed while suspended in water, without the beaker of water contacting the suspension rig or the scale, a schematic of this is depicted in Figure 27. Then the coating density was calculated using Equation [5].

[5]

$$D = \frac{A \cdot P_w}{B - (C - E)}$$

Where D is the coating density, A is the mass of the sample in air (g), B is the mass of the oil-impregnated sample (g), C is the mass of the oil-impregnated sample and suspension rig immersed in water (g), E is the mass of the suspension rig immersed in water (g), and P_w is the density of the water (g/cm^3).

3.5.4. Surface Roughness

The surface roughness of the coatings were measured using a Wyko NT1100 optical profiling system. Prior to scanning the samples were thoroughly washed in an ultrasonic ethanol bath for ten minutes and dried. Individual samples were scanned at a magnification of 20 X, which generated 3-D dimensional profiles of the surface topography. The topography profiles were then processed using a low pass filter within Vision software to remove the unassigned pixels which were given a default value of the maximum scale height and resulting in a 3-D surface profile of the coating topography with minimal no pixel anomalies. From these plots the average surface roughness (R_a) and root

mean squared roughness (RMS) values were measured at three locations on the sample surface to calculate the average surface roughness and average root mean squared roughness of the sample.

3.5.5 Hardness Testing

The hardness was measured using a Mitutoyo Rockwell hardness tester (Figure 37), set to A scale according to ASTM E-18. As per the standard procedure a diamond indenter was used with an indentation force of 60 kgf. Prior to testing a calibration test was conducted on a calibration block to confirm the hardness tester was calibrated and operating normally. Then five indentations on each sample were completed with the distance between subsequent indentations at least three times the diameter of the previous indentation to avoid error associated with strain hardening of the sample. After the testing was completed an additional calibration test was conducted to confirm the equipment was still operating accurately. From the five indentations of each sample the highest and lowest outliers were removed and the average was taken from the middle three readings, as well as the standard deviation.

3.5.6 Adhesion testing

The adhesion tests were performed according to ASTM C-633 standard to measure the bond strength of TS coatings. Each test coupon was glued between two cylindrical bars (loading fixtures made of low carbon steel) of 25.4 mm diameter using FM1000 adhesive tape. The surfaces of the loading fixtures and the uncoated side of the test coupon were machined flat, mechanically roughened by grit blasting using course crushed glass blasting media, gently washed using soap and water to remove any residual dirt or grease, and cleaned in an ultrasonic ethanol bath for 15 minutes. This ensures contaminant free

surfaces, strong bonding with the test coupon, and repeatable testing. The fixtures were assembled and heated in a preheated furnace at 190˚C, under compressive stress (0.23 MPa) to ensure the adhesive penetrates the roughened surface, for a duration of 180 minutes to cure the adhesive. The assembled fixture was then lightly sanded to remove any residual adhesive forming during the curing process from the outer surface. The assembly was then secured to the remainder of the loading fixture using clevises to allow the glued assembly to align itself parallel to the axis of elongation of the tensile testing machine, ensuring the applied force generated a pure tensile force perpendicular to the coating surface.

The assembly was positioned in an MTS-Criterion tensile testing machine with a maximum load capacity of 150 kN. Then the tensile load was applied via a constant cross-head displacement rate of 0.013 mm/s and the maximum pull load was recorded and converted to stress using Equation [6].

[6]

$$\text{Adhesion/cohesion Strength} = \frac{\text{Maximum load}}{\text{Cross-sectional area}}$$

3.6 Erosion Testing

3.6.1 Erosion Resistance Measuring Method

During the drilling process drilling fluid is pumped downhole to power the drill head motor, remove heat form the drill head assembly, and remove drill cuttings from the drilling surface. This method is currently the most effective approach to cool components and remove cuttings, but introduces an extremely erosion environment, with suspended cuttings traveling at high velocities and impacting the exterior wall of the piping system which can lead to premature component failure causing decreased drilling rates and

increased operating costs. Due to varying drilling conditions and increased costs of repeatedly removing the drill head for examination, the erosion resistance is difficult to quantify without the implementation of laboratory scale erosion simulations and in the case of this coating no previous erosion resistance research or testing had been conducted.

As a result, a recirculating erosion testing rig was required to be designed and fabricated to develop a baseline for the erosion resistance of the uncoated substrate which could then be directly compared to the coated substrate and the modified coatings, along with the operating parameters and procedures to conduct erosion testing. Since designs and operating parameters are not standardized, due to the plethora of erosion scenarios, no two erosion testing rigs would yield the same result. Therefore the erosion resistance of two reference materials was required to normalize the erosion resistance in order to compare results between erosion testing rigs, which are; aluminum 1100-0, aluminum 6061-T6, stainless steel AISI 316, and 99.98% pure annealed Nickel [48].

To quantify the erosion resistance, a plot of the cumulative volume loss versus the cumulative exposure time was constructed for each material which included a minimum of 11 data points. This allows for the maximum erosion rate (Q_e) and the terminal erosion rate (Q_{et}) to be calculated by determining the largest slope of the linear portion of the curve and the slope of the steady-state linear portion of the curve, respectively, where an erosion rate approaching zero signifies an increase in the erosion resistance. Then the erosion resistance of that specific material than can be normalized in terms of a reference material using Equation [7] from [48].

[7]

$$Se = \frac{Q_{e\ reference}}{Q_{e\ material}}$$

3.6.2 Design and Fabrication of Solid Particle Erosion Testing Rig

A recirculating type slurry erosion tester was chosen as the most practical design, with a schematic of this erosion tester shown as Figure 30. The slurry storage tank has a capacity of approximately 15 L with a tapered base, to ensure suspended particles to not settle within the base of the tank and continually recirculate through the erosion tester. The slurry is then gravity fed to a dual diaphragm pump (Sandpiper model S07 non-metallic design level 1), capable of pressurizing the slurry to a maximum of 90 (psi). Once pressurized the slurry flows through a needle type bypass valve (allowing mud solution to bypass the nozzle assembly and be returned directly to the reservoir, which allows for accurate flow control and if necessary, can be used to agitate the mud solution in the reservoir), through a pressure gauge, and finally into the pressure equalization chamber. The equalization chamber is symmetrically fed from each side of the chamber then divided into three acceleration tubes measuring 4" by ½" NPT where the fluid and erodent particles can accelerate towards the sample surface. At the end of each acceleration conduit a tapered fitting was added to allow a nozzle to be threaded into the assembly. This allows for standard ½" NPT nozzles to easily be interchanged to modify the spray pattern and orifice diameter if necessary. The fluid pressure and thus the fluid flow rate can be precisely controlled by adjusting the air supply pressure at the pump, or by changing the nozzles. Additionally, the entire nozzle assembly is adjustable to change the distance between the nozzle tip and sample surface from 1-1.5". For the purpose of this testing the distance from nozzle tip to sample surface was set to 1". Finally, the entire assembly is encapsulated in a

transparent polycarbonate chamber, which funnels the slurry solution back into the reservoir, once the slurry exits the nozzle and impacts the sample.

3.6.3 Solid Particle Erosion Testing Procedure

3.6.3.1 Sample Preparation

Prior to erosion testing some of the sample surfaces were ground/polished relative to the test parameters, showed in Table 6. In addition to surface preparation, a small flat was cut into the side of samples with a circular geometry using a low speed diamond saw which allowed the samples to be mounted within the sample holder in the same location after being removed for weighing. After surface preparation and sectioning each erosion sample was degreased using soap and water then cleaned in an ultrasonic ethanol bath for ten minutes. Each sample was then thoroughly dried and individually weighed three times, taking the average of the readings as the initial mass in grams.

3.6.3.2 Grinding Procedure

SharkSkin implements a planer surface grinder mounted with a precision diamond wheel (D150 75 J166658-2) from Graff Diamond Products. The surface grinder removes initial surface asperities in increments of 12.6 (um), while cooling the surface with water. This process was continued until the all of the initial surface asperities developed during coating deposition were removed.

3.6.3.3 Slurry Solution Preparation

The slurry solution was prepared prior to testing to serve as a drilling mud analogue, in order to properly simulate drilling conditions as close to as possible in a laboratory environment. Granular bentonite was added to water and mixed in a blender until a smooth consistency was achieved, to a bentonite concentration of 30 (g/L). To simulate cutting

chips and promote solid particle erosion, course crushed silica glass was added to the drilling mud. These particles have an angular morphology and a cross-sectional area of 3.64 ± 2.14 mm^2. Prior to initiating each test, 6 Kilograms of simulated drilling mud solution and 120 grams of silica particles were added to the erosion tester reservoir and recirculated through the erosion tester (without nozzles) for 10 minutes until well mixed.

3.6.3.4 Erosion Testing Procedure

Prior to each round of testing the erosion tester was thoroughly washed using water to purge the plumbing and pipe system of any residual slurry solution or blasting media from previous trials. Once the slurry was added to the reservoir with the previously mentioned concentrations the solid stream nozzle offices were measured using a bore gauge (1.854 mm) and installed into the nozzle assembly. Following the nozzle installation, the nozzle assembly encasement was cleaned, forcing any residual slurry solution back into the reservoir for recirculation. The samples were then mounted into the sample holder and secured to the nozzle assembly case. The pump air supply pressure was then set to approximately 90 psi, which was slightly adjusted once the test began to adjust the mud pressure to 80 psi. The erosion tester was ran continuously for one cycle (ten minutes) then turned off, where the samples were removed, cleaned, and weighed. Once again the nozzle assembly case was cleaned to ensure complete recirculation of the slurry solution. Once the samples were weighed they were reinstalled in the same position and the erosion tester was ran for another cycle. This procedure was repeated for a total of 15 cycles (150 minutes) for each trial. Upon testing completing the nozzles were removed from the nozzle assembly, washed, and the orifice measured to ensure the nozzle orifice did not wear. It was determined after 15 cycles the nozzle orifice remained at the same (0.0073”). Finally

the circulated erosion particles were collected for further investigation and the remaining slurry was disposed of, after which the erosion tester was thoroughly cleaned.

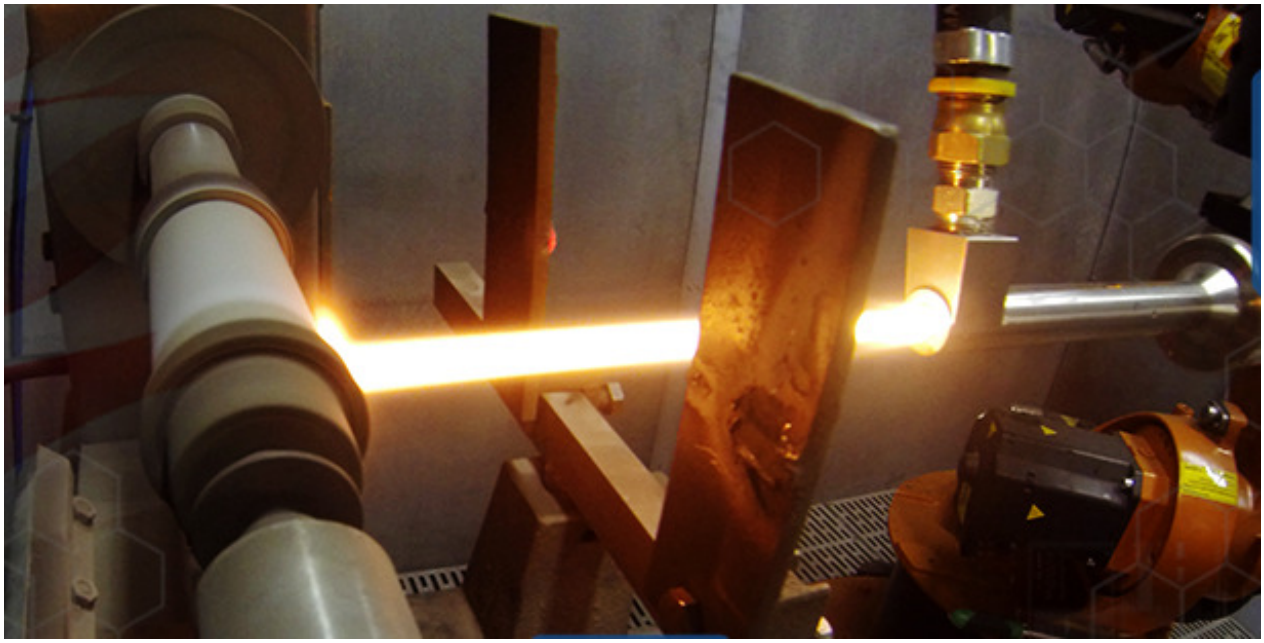

Figure 33 - HVOF coating deposition of directional drilling component, applied at SharkSkin coatings ltd. Facility [60].

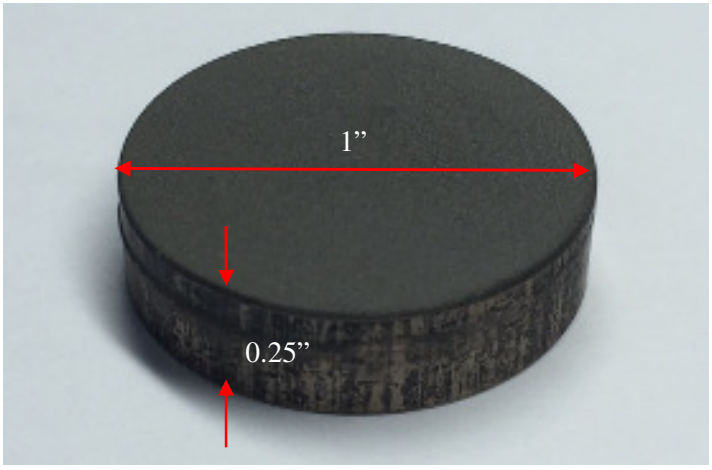

Figure 34 – Standard HVOF coated Toughmet coupon in the as-sprayed condition.

Table 4 - Standard coating deposition parameters.

Console	JKIII
Main Fuel	Hydrogen
Carrier Gas	Argon
Powder	Amperit 558
Cooling Knife (mm)	228.6
Carrier Pressure Target (kPa)	620.5
Carrier Pressure Actual (kPa)	567.4
Oxygen Pressure Target (kPa)	689.4
Oxygen Pressure Actual (kPa)	648.1
Hydrogen Pressure Target (kPa)	689.4
Hydrogen Pressure Actual (kPa)	646.7
Inlet Temp Target (K)	302.6
Inlet Temp Actual (K)	301.5
Flow Target (g/min)	12.5
Flow Target Actual (g/min)	13
Outlet Temp Target (K)	322
Outlet Temp Actual (K)	318.1
Feeder Speed (rpm)	2.3
Tar Feed Rate (g/min)	48
Deposition Angle (deg)	90

Surface speed (m/s)	2.03
Transverse Speed (m/s)	0.5
Stand-off distance (mm)	254
Carrier Pressure Target (kPa)	465.4
Carrier Pressure Actual (kPa)	426.1
Oxygen Pressure Target (kPa)	437.8
Oxygen Pressure Actual (kPa)	517.4
Hydrogen Pressure Target (kPa)	551.5
Hydrogen Pressure Actual (kPa)	530.9
Number of cycles	5
Coating Thickness (mm)	0.1397
Deposition rate (mm/pass)	0.0279
Initial Part Temp (K)	295.4
Peak Part Temp (K)	377.6
Carrier Pressure Target (m^3/min)	1.6142
Carrier Pressure Actual (m^3/min)	1.614
Oxygen Pressure Target (m^3/min)	17.275
Oxygen Pressure Actual (m^3/min)	17.275
Hydrogen Pressure Target (m^3/min)	37.467
Hydrogen Pressure Actual (m^3/min)	37.467

Table 5 – Semi-automatic grinding/polishing procedure.

Purpose	**Lubricant**	**Grit**	**Central Load (N)**	**Duration (s)**	**Surface Speed (RPM)**
Planer grinding until all specimens are in the same plane	Water	120	100	30-300	200
Rough Grinding	Water	240	100	30	200
	Water	400	100	30	200
Fine Grinding	Water	600	100	30	200
	Water	800	100	30	200
	Water	1200	100	60	200
Rough Polishing	None	3 µm	80	300	100

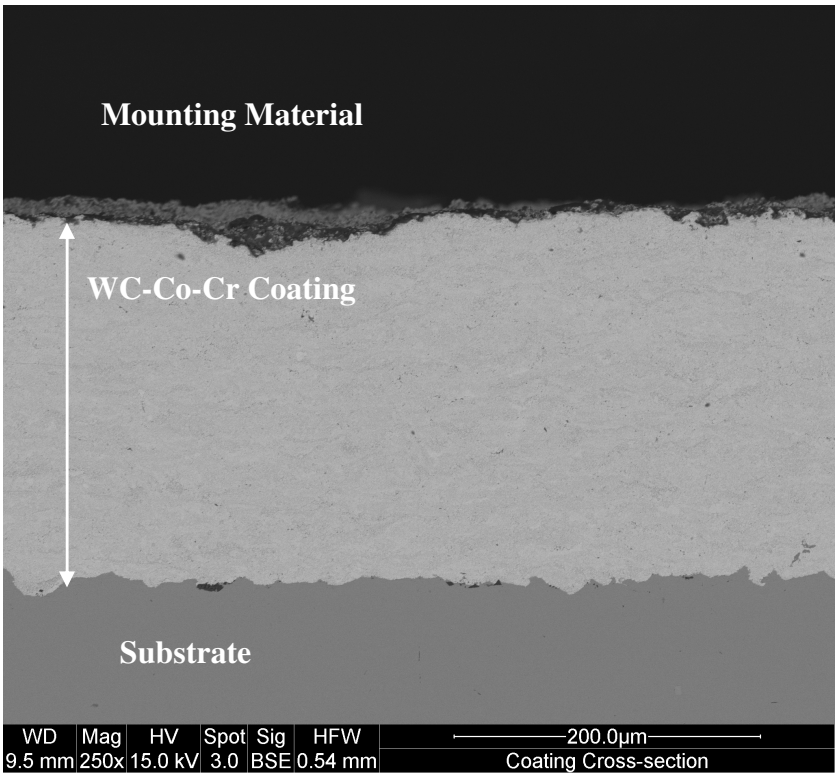

Figure 35 – SEM BSE image of standard coating cross-section at 250 X.

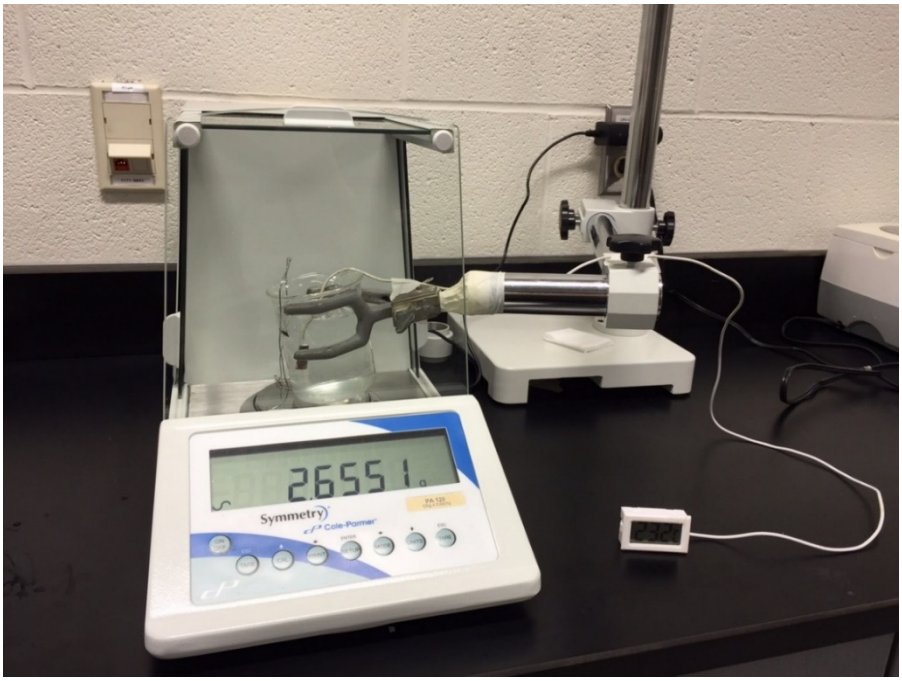

Figure 36 - Coating density measurement test setup.

Figure 37 - Mitutoyo Rockwell hardness testing machine.

Figure 38 - Adhesion sample mounted to loading fixture and secured into tensile testing grips.

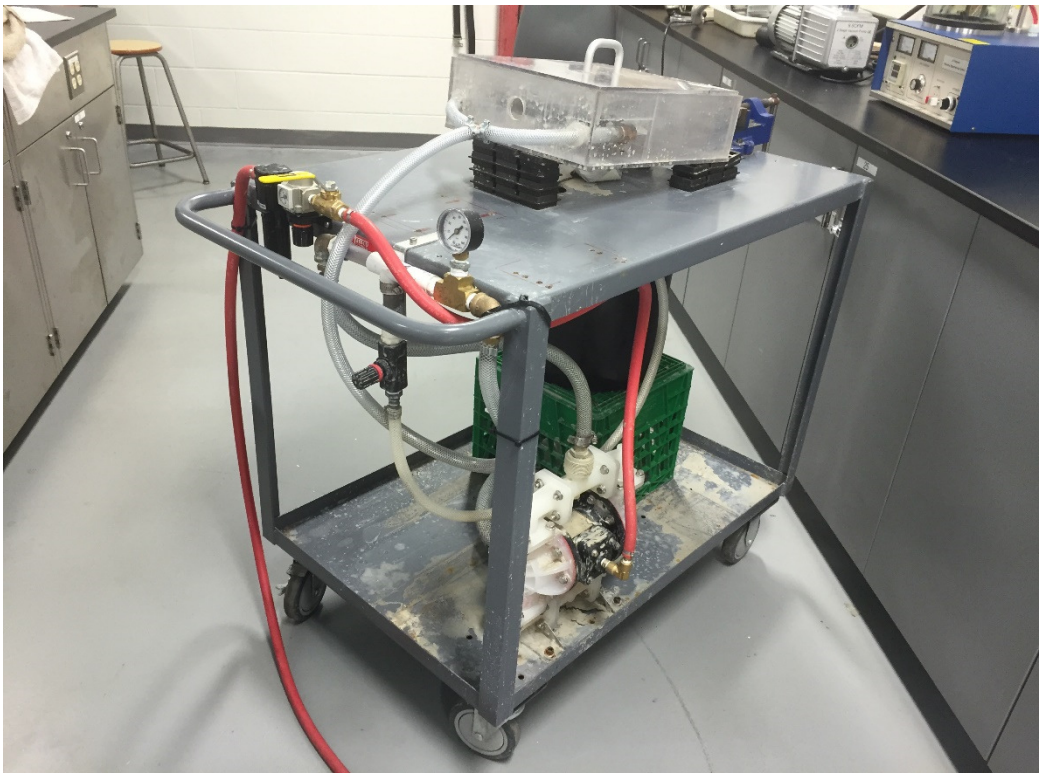

Figure 39 - Digital image of fabricated erosion tester overview.

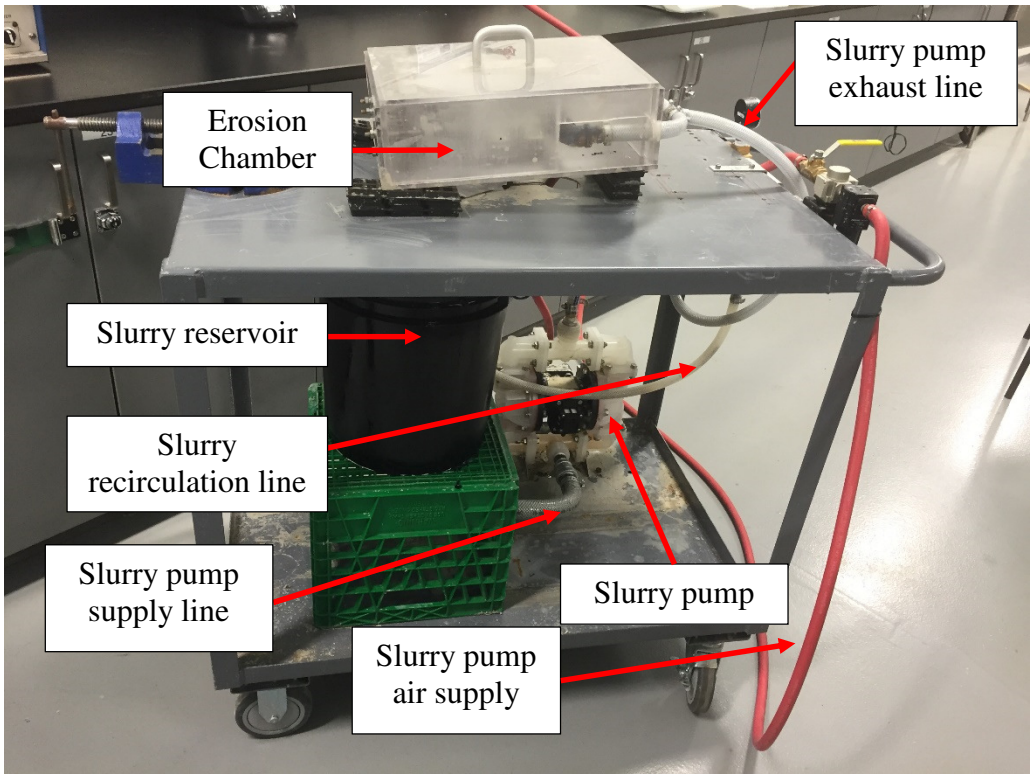

Figure 40 - Schematic structure of erosion tester slurry pumping system.

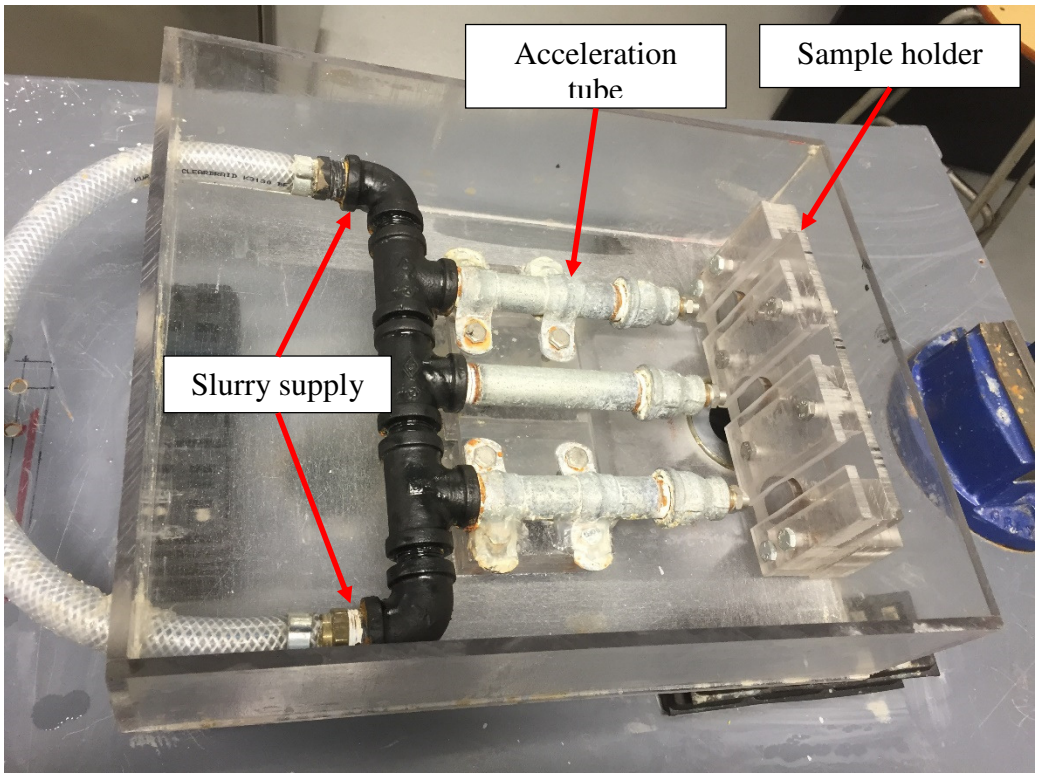

Figure 41 – Schematic structure of erosion chamber.

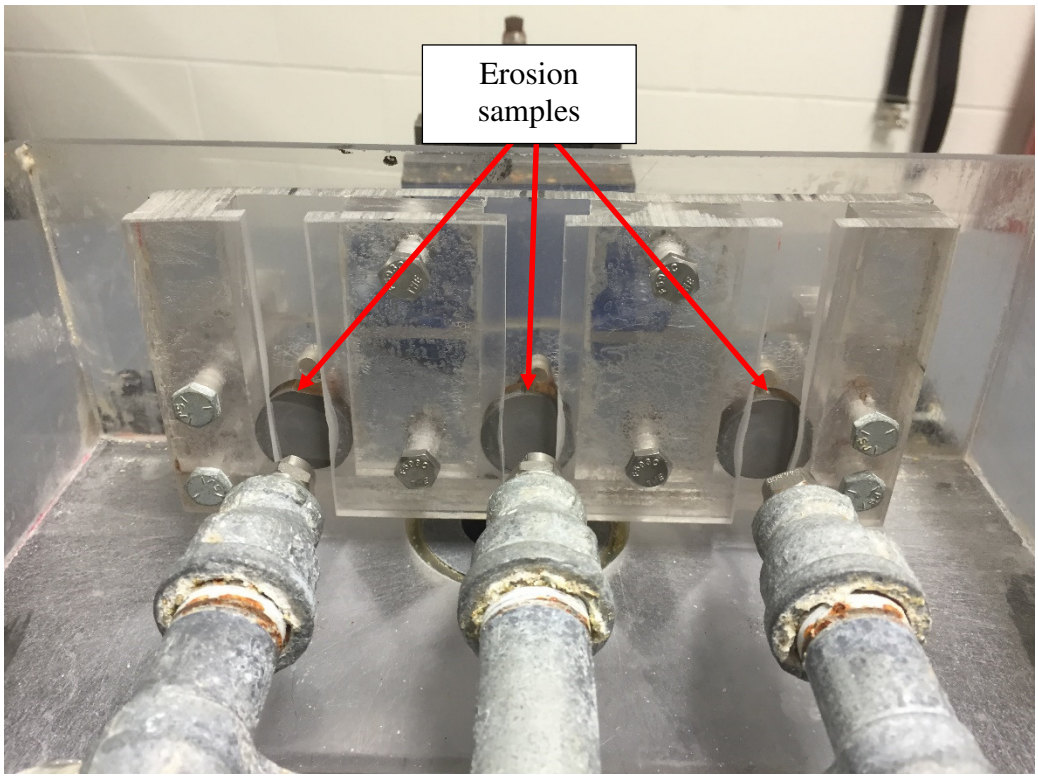

Figure 42 - Schematic structure of erosion sample holder.

Table 6 – Surface preparation procedure of erosion samples prior to erosion testing.

Test Sample	**Surface Preparation**
Reference Materials	As-received
Uncoated Toughmet	Manually polished using SiC grinding paper of decreasing roughness from 120 to 1200 grit.
TS Coating	As-received
Ground TS Coating	Ground using a surface grinder mounted with precision diamond wheel in 12.6 (um) increments until initial surface asperities were removed.

Chapter 4: Experimental Results

This chapter elaborates and outlines in detail the results obtained from the testing procedures presented in chapter three, which includes: the microstructural characterization testing of the coating cross-section, observation using optical microscopy, scanning electron microscopy, and optical profilometry (Wyko), as well as the results obtained from hardness testing, coating adhesion testing, and solid particle erosion testing. For convenience the order of test results follow the order of procedures represented in the previous chapter.

4.1 Coating Feedstock Characterization Results

This section outlines the results and observations from characterizing the coating feedstock produced by H.C. Starck (Amperit 558).

4.1.1 Feedstock Size Distribution

The feedstock was mounted on carbon tape and observed using SEM, which can be seen in Figure 43. The image was then processed into a binary image using ImageJ, and filtered such that only the outline of each particle remained. Then further processed using ImageJ to count and measure the radius of each whole particle remaining within the image to calculate the particle size distribution, Figure 44. The particle count and size were then confirmed by manually counting and measuring each particle to verify the processed data. Once the particle area was calculated, it was assumed the particles were circular to approximate the particle radius, with minimal particles disregarded due to their processed shape (oblong particles, or particles in contact, which appear as a single particle after

processing), for reference some of these particles are located in the bottom right corner of Figure 44 as a particle outline without a number located in the middle. This allowed a histogram to be created of the relative frequency (%) and particle diameter (um), as shown in Figure 45. This shows a relatively uniform particle size distribution, with a diameter between 20 -30 um, which coincides with the technical bulletin provided by H.C. Starck.

4.1.2 Feedstock Composition

An EDS map was constructed (Figure 47) from the SEM image of amperit 558 (Figure 46) to determine the feedstock elemental composition and distribution. It is important to note that due to the space between particles a carbon rich phase was detected seen as oblong faded yellow regions, which represents the carbon tape required to secure the particle during observation and that this phase is disregarded in the elemental and weight % analysis to follow. Additionally, specific regions of some particles show no composition, this is because the x-ray emitter and detector is mounted on an angle, which does not allow for these regions to be detected due to the particles spherical morphology.

Therefore the detectable X-ray diffractions were used to construct an elemental map of amperit 558 (Figure 47), which shows a relative even distribution of elements within the entire map, as well as within each particle. Table 7, shows the area percent allocation of each detected phase of the elemental map, with the elements ranked in descending weight percent from left to right. This suggests that these particles have a uniform composition throughout the entire feedstock.

The weight percent of each element was then determined for each phase and multiplied by the percent of each phase to determine the overall weight percent of each element which is summarized in Figure 48. Resulting in the following elemental

composition; Tungsten (W) 80.53%, Carbon (C) 5.21%, Cobalt (Co) 7.77 %, Chromium (Cr) 3.34 %, Oxygen (O) 1.65%, and Iron (Fe) 1.47%.

4.1.3 Feedstock Morphology

Feedstock particle morphology and composition were observed using SEM and EDS, where three distinct particle morphologies were observed, represented as a densely packed solid particle, a porous solid particle, and a porous hollow particle, shown as Figure 49, Figure 51, and Figure 53, respectively. Furthermore, EDS line scans were conducted to confirm the composition within individual feedstock particles, seen as Figure 50, Figure 52 , and Figure 54 where the location is indicated by the superimposed red line within Figure 49, Figure 51, and Figure 53, respectively.

4.1.4 Surface Temperature During Coating Deposition

The work piece surface temperature was recorded during coating deposition using an infrared thermometer mounted inside the deposition chamber aimed at the center of the coupon, where the surface temperature was recorded after the completion of each deposition cycle. It was determined for a stand-off distance of ten inches that the surface temperature stabilized at approximately 335 °F after the third deposition cycle. This indicated that pre-heating cycles in excess of two would not further increase the surface temperature and therefore not further modify the coating. The temperature plot is shown in Figure 55. Additionally, it was determined the work-piece surface temperature was significantly modified when the stand-off distance was altered. The trend was continuous across all modified stand-off distances, with an increase in surface temperature as the stand-off distance was decreased. This resulted in the final surface temperature of 299°F,

335°F, 359°F, 383°F for stand-off distance of 12, ten, eight, and six respectively, which is represented in Figure 56.

4.2 Microstructural Characterization of Pre-Spray Treated Toughmet

This section outlines the results obtained from observation of the substrate after it was mechanically roughened via grit blasting.

4.2.1 Surface Roughness

Surface roughness and topography of pre spray treated (grit blasted) toughmet were studied using an optical surface profilometer. Figure 57 represents one of three 3-D profiles of the samples surface topography. From these plots the surface roughness (R_a) and root mean squared roughness (RMS) values were measured for each of the three plots and averaged, which have been summarized in Table 8.

4.2.2 Observation of Grit Blasted Surface

All substrate surfaces must be roughened prior to TS application to ensure proper mechanical interlocking, but this process can reduce the coatings adhesion strength if the blasting media becomes embedded within the substrate. To quantify the presence of blasting media a grit blasted substrate was observed using SEM and analyzed using EDS. Figure 58 is an SEM image of the grit blasted surface, where the dark regions represent embedded particles. This was confirmed by constructing an EDS map of Figure 58, shown as Figure 59, where the blue region represents an aluminum oxide rich spectrum. This blue region represented six percent by area of the substrate. Additionally, a high magnification image of an embedded particle is shown in Figure 60, which consisted of a particle with sharp features (region one) and a particle with rougher features (region two), where the

EDS spectrum is represented in Figure 61 and Figure 62 respectively, which contains large spikes of Al, O and Si.

4.3 Microstructural Characterisation of The Coating

This section outlines the microstructural characterization results obtained from the employing the standard coating deposition techniques previously outlined.

4.3.1 Coating Cross-sectional Microstructure

Specimens were prepared from cross sections of samples using conventional metallographic techniques for TS coatings. Figure 63 shows an SEM of the cross-section of the WC-Co-Cr coating on toughmet substrate. Using ImageJ the cross section was analyzed at six locations to determine the thickness, resulting in an average coating thickness of 221.46 ± 3.76 (um). Additionally, the coating interface was observed, and is shown in Figure 65. An EDS point scan was conducted on the particle at the coating interface (location 1), which was confirmed to be Al_2O_3. An EDS point scan was also conducted at location 2 confirming the light grey particles are WC. Finally, an EDS point scan was conducted on the dark grey region surrounding WC particles was shown to contain peaks of W, Co, Cr, and C. This confirms the coating contains solid WC particles embedded within the WC-Co-Cr, with minimum Al_2O_3 particles at the coating interface, present from pre-spray roughening processes. Furthermore, when observing the coating cross-section, interlaminar micro-cracks and cracked WC particles were observed as seen in Figure 69.

4.3.2 Coating Porosity

This section represents the coating porosity results obtained from processed optical images of coating cross-section using ImageJ. The coating porosity is typically a good indicator of the coating quality, which was represented as the area percent and is commonly used for quality control purposes. Furthermore, the coating porosity of HVOF TS coatings is typically lower than other TS application methods, due to the high in-flight particle velocity, where HVOF coatings should have a porosity less than two percent, and lower porosity commonly correlates to an improved coating performance.

4.3.2.1 Standard Coating

The coating porosity of the standard coating cross-section was measured to determine a baseline for comparison of the modified coatings. The pre-processed image is shown as Figure 70 which was then processed using ImageJ to crop the coating and filter out the background, resulting in the coating pores and or voids represented as black pixels and the remainder white. Once processed the percent area can be calculated by the ratio of black to white pixels from the processed image. The processed image of the standard coating is shown as Figure 71, which resulted in a coating porosity of 0.423 %, where it is assumed the coating porosity is randomly distributed and uniform throughout the coating.

4.3.2.2 Modified Pre-Spray Surface Temperature

The standard coating deposition parameters were modified to determine the effect of pre-spray substrate temperature on the coating porosity. The porosity of the modified coating was compared to the standard coating, which can be represented as the coating porosity with zero pre-heating cycles, shown as Figure 70. One pre-heating cycle was then applied, which resulted in a substantial increase in the coating porosity to 2.255% which

can be easily recognized in Figure 72 and in the processed image shown in Figure 73. When two pre-heating cycles were applied the coating porosity was once again increased relative to the standard coating to 1.579%, however did not exceed the porosity of one pre-heating cycle. The coating porosity after two pre-heating cycles is represented as Figure 74 and the processed image is shown in Figure 75. Furthermore, the effect of pre-heating cycles on coating porosity have been summarized into Table 11 and Figure 76.

4.3.2.3 Modified Stand-off Distance

Similarly to the pre-spray heated modified coating, the coatings with modified stand-off distances are directly compared to the standard coating which has a stand-off distance of 10 inches. First the stand-off distance was increased from 10" to 12", which was found to have a large increase in coating porosity to 1.212%, shown as Figure 77 and the optical image being Figure 78. The stand-off distance was then reduced to 8", which resulted in a reduction of coating porosity to 0.334%, which can be seen in Figure 79 and the processed image as Figure 80. Finally, reducing the stand-off distance to 6" resulted in a slight increase in coating porosity to 0.716%, likely caused by insufficient thermal softening due to the decreased particle dwell time. This indicates the coating porosity is directly correlated to the stand-off distance, with the apparent trend of decreasing coating porosity as stand-off distance decreases. Additionally, the effect of stand-off distance on coating porosity is tabulated as Table 12 and graphically represented as Figure 83.

4.3.3 Coating Density

This section outlines the results on the coating porosity measurements of the standard and modified coatings, measured according to ASTM B962 using Archimedes method. The coating density was required in order to convert the mass loss during erosion

testing into a volume loss so materials of different densities can be directly compared in terms of volume loss. Furthermore, the coating density was used to confirm the correlation of coating porosity of coatings with modified deposition parameters.

4.3.3.1 Standard Coating

The standard coating density was calculated to develop a baseline value, where an increase of density signifies a decrease in overall porosity which typically correlates to improved coating performance. The coating density was calculated according to Equation [5], based on the procedure detailed in chapter three. To accurately measure the coating density each measurement was measured three times and the average was used to calculate the coating density for three coating samples, with the standard coating having an average coating density of 12.783 ± 0.009 (g/cm^3).

4.3.3.2 Modified Pre-Spray Surface Temperature

The coating density of the pre-spray heated coating density was measured identically to the standard coating. The results correlate well with the measured coating porosity where the lowest coating density occurred with samples of one pre-heating cycle, measuring 12.349 ± 0.167 (g/cm^3), which also correlates to the highest porosity. Two pre heating cycles also relates to the coating porosity with the second lowest density measuring 12.697 ± 0.175 (g/cm^3). The results of the measured density have been tabulated in Table 13 and graphed as Figure 84.

4.3.3.3 Modified Stand-off Distance

Similar to the modified pre-spray treatment cycles, the coating density of samples with a modified stand-off distance were measured identically to the standard coating with the standard coating representing the ten inch stand-off distance. The coating density

correlates identically to the coating porosity measurements, which shows an increase in coating density as the stand-off distance decreases. This results in the lowest coating density of this modified parameter occurring at the largest stand-off distance (12") with a value of 12.650 ± 0.043 (g/cm^3). The density continually increases to 12.827 ± 0.004 (g/cm^3) when a stand-off distance of eight inches was used and slightly decreased to 12.730 ± 0.029 (g/cm^3) when the stand-off distance was reduced to six inches. Additionally, these results have been represented in Table 14 & Figure 85.

4.3.4 Coating Surface Roughness

Surface roughness and topography of WC-Co-Cr sprayed samples in the as-sprayed and ground condition were studied using an optical surface profilometer (Wyko); Figure 86 and Figure 87 represent three dimensional profiles of the samples surface topography. From these plots the average surface roughness (R_a) and root mean squared roughness (RMS) values were measured at three locations on the sample surface, which have been summarized in Table 15. As confirmed in Figure 87 the grinding process removed surface asperities, thus reducing the average surface roughness (Ra) from 4.49 ± 0.63 (um) to 0.249 ± 0.02 (um). The purpose of planer surface grinding is to remove initial surface asperities in order to adhere to the part tolerance and prevent the "break-inn" period of the coating. Preventing this initial wear will reduce play between components and prevent additional third body wear from the removal of surface aspetites.

4.4 Hardness Results

This section represents the results of Rockwell hardness testing conducted on un-coated toughmet and WC-Co-Cr coated toughmet in accordance with ASTM E-18-12 [47]. The hardness of the substrate and WC-Co-Cr coated substrate were measured using a Rockwell

hardness tester set to scale A. Due to the surface roughness of the as sprayed WC-Co-Cr coating, hardness measurements were conducted on coated samples in the as-sprayed and ground surface conditions, to confirm the removal of coating asperities did not affect the hardness readings.

4.4.1 Standard Coating

The uncoated toughmet has been found to be relatively hard with a Rockwell hardness of 64.33 ± 0.12 (HRA). However, the coated substrate increased the hardness by 24 % compared to the uncoated hardness, resulting in an as-sprayed hardness of 79.8 ± 0.51 (HRA). When the initial surface asperities were removed, via planer grinding the hardness was slightly reduced to 74.40 ± 0.00 (HRA). For convenience, this information has been summarized in Table 16.

4.4.2 Modified Pre-Spray Surface Temperature

The effect of pre-heating cycles on coating hardness was measured for samples in the as-sprayed condition with zero, one, and two pre-heating cycles prior to coating deposition. This resulted in a peak hardness of 80.67 ± 0.26 (HRA), occurring at two pre-heating cycles. The coating hardness reached a minimum value of 78.73 ± 0.12 (HRA) at one pre-heating trial, while the standard coating with zero pre-heating trials resulted in a median value of 79.80 ± 0.51 (HRA). The hardness results have been summarized in Table 17 and Figure 88. The reduction in hardness for one pre-heating cycle is most likely due to the collapsing of pores due to the increased porosity in the coating, while the increase in hardness from two pre-heating cycles is most likely due to the increase of carbides from the increased surface temperature.

4.4.3 Modified Stand-off Distance

The effect of stand-off distance on coating hardness was measured for samples in the as-sprayed condition with stand-off distances ranging from six 12 inches in two inch increments. This resulted in a peak hardness of 80.7 ± 0.0.65 (HRA), occurring at a stand-off distance of six inches. The coating hardness continually decreases slightly as the stand-off distance increases, to 80.33 ± 0.54 (HRA), 79.80 ± 0.51 (HRA), 77.97 ± 0.48 (HRA), for eight inch, ten inch and 12 inch respectively. This decrease in hardness is likely caused by a reduction in carbides due to decreased surface temperature due to the increased stand-off distance as well as increasing the stand-off distance, increases the particle dwell time and thus the inflight particle temperature which increases the potential for feedstock decarburization during coating deposition.

4.5 Coating Adhesion Results

This section depicts the adhesion results from adhesion testing conducted according to ASTM C-633 [18] to measure the bond strength of TS coatings. Each deposition condition was tested three times in order to develop an average adhesion strength of the coating. During testing the load is increased due to a constant cross-head displacement of 0.013 mm/s until the loading fixture is assembly is separated, indicating failure. The failure can occur in one of three ways, either adhesive, cohesive or delamination. An adhesive failure occurs within the FM1000 adhesive and does not represent failure within the coating and indicates the coating. Additionally, this does not represent the maximum adhesion strength of the coating, only the maximum strength of the glue which is currently available and is accepted within the TS industry. A cohesive coating failure occurs when deposited splats debond and crack propagation occurs along inters-plat cracks resulting in an inter-

lamellar cohesive fracture. This fracture stress indicates the upper limit of the coating adhesion strength and can be considered as a coating failure. Finally, coating fracture can occur at the coating and substrate interface indicating a delamination failure. This also indicates a coating failure in addition to insufficient mechanical roughening during pre-spray surface treatment.

4.5.1 Standard Coating

It was determined the standard coating was similar to the rated strength of the FM 1000 adhesive of 69 MPa when new, which resulted in a standard coating adhesion strength of 67.76 ± 0.03 MPa where all three failures occurred within the adhesive, indicated in Table 19.

4.5.2 Modified Pre-Spray Surface Temperature

The adhesion testing was repeated for samples with one and two pre-spray surface treatments, which was compared to the standard coating with zero pre-spray surface treatments. It was determined the pre-spray heating cycles had a minimal impact on the adhesion strength with an average failure (calculated by averaging the maximum failure stress from three adhesion tests for each deposition parameter condition) stress of 67.10 ± 1.50 MPa and 66.04 ± 0.38 MPa for one and two pre-heating cycles respectively. Although during adhesion testing one cohesive failure occurred for each of the pre-heating coatings, indicating the maximum adhesion strength of the coating is being approached. The results of each trial are represented in Table 20, Table 21, and summarized in Figure 90. Additionally, it should be noted that these values can be perceived equal when the standard deviation is considered.

4.5.3 Modified Stand-off Distance

The adhesion testing was also repeated for samples with modified stand-off distances of 12, eight, and six inches, which was compared to the standard coating with a stand-off distance of ten inches.. It was determined the stand-off distance had a significant impact on the adhesion strength which resulted in a substantial decrease in adhesion strength when the stand-off distance was decreased to six inches, where the all trials exhibited cohesive failure at a stress of 43.79 ± 2.59 MPa, shown in Table 22. As the stand-off distance increased to eight inches the adhesion strength also increased similar to the standard coating with a failure stress of 66.51 ± 1.35 MPa where all trials occurred adhesively, as shown in Table 23. Finally, once the stand-off distance was further increased to 12 inches the adhesive strength remained similar the standard coating to 67.00 ± 0.99 MPa, which resulted in a single cohesive failure, shown in Table 24. Similarly to the pre-heated samples this indicates the measured failure stress is approaching the maximum failure stress of the deposited coating. For convenience, the adhesion strength of coatings with a modified stand-off distance have been summarized in Figure 91.

4.6 Solid Particle Erosion Results

This section represents the results of SPE testing in accordance with ASTM G73 [48], where the cumulative volumetric loss is plotted versus the sample exposure time. This testing was conducted for the reference materials from ASTM G73 as well as uncoated and coated toughmet. Additionally, the erosion testing was conducted for coatings with modified stand-off distance, which did not contain excessive porosity, as excessive porosity (above one percent) is an early indicator of reduced coating quality.

4.6.1 Preliminary Erosion Results

Preliminary solid particle erosion testing was conducted on two reference materials (AL 6061 T6 and Stainless Steel 316) as well as uncoated toughmet and coated toughmet in the as-sprayed condition. The cumulative mass loss was converted to volume loss using the materials density and graphically represented in relation to the cumulative exposure time, represented as Figure 92. This resulted in AL 6061-T6 exhibiting the largest volumetric loss of 24.9699 mm^3 after 150 minute of exposure, while the stainless steel 316 had a volumetric loss of 7.9191 mm^3 exposed to identical conditions after 150 minutes. The toughmet in the uncoated condition was found to be slightly more erosion resistant then the SS 316 reference materials with a total volumetric loss of 7.6602 mm^3 after 150 minutes of exposure. However, the coated toughmet in the as-sprayed condition demonstrated the best erosion resistance compared to the reference materials and the uncoated toughmet with a total volumetric loss of only 0.4112 mm^3 after 150 minutes of exposure, due to the minor relative volume loss of the as sprayed coating an individual graph of this plot was added to clearly represent the coatings behaviour during erosion testing which is represented as Figure 93.

As represented is Figure 92 and Figure 93, each of the tested materials exhibited two individual erosion rates, initially a steep erosion rate which represented the maximum erosion rate (Q_e), followed by stabilization of the erosion curve resulting the terminal erosion rate (Q_{et}), and finally the minimum test duration, which was surpassed in every condition. For simplicity these results were summarized in Table 25 and Figure 94. Additionally, these erosion rates were normalized by selecting the uncoated toughmet as the baseline material for comparison, where the coating in the as sprayed condition was

found to have a maximum erosion rate 14.91 times better than the uncoated toughmet and a terminal erosion rate improvement of 24.75 fold, summarized in Table 26 and Figure 95.

The erosion scars of the uncoated toughmet and coated toughmet in the as-sprayed condition were observed using a stereo microscope to obtain a low magnification representation of the wear scar. The uncoated toughmet wear scar is easily recognisable as shown in Figure 96, with a maximum wear depth of 1.72 mm (Figure 97), while the wear scar of the coated toughmet in the as-sprayed condition appears as a slight discoloration of the coating, seen in Figure 98. The wear scar morphologies were investigated by implementing SEM, where significant type one cutting and thus a sharp angular surface morphology was observed within the uncoated toughmet erosion scar seen in Figure 99. However, the coated toughmet did not exhibit any type one cutting, but rather minimal smoothing of surface asperities from the as-sprayed condition shown in Figure 100. Additionally, at higher magnification the erosion scar of the coating contains smooth hemispherical formations seen in Figure 101, which suggests entire particle splats were spalled of the coating surface during erosion testing, indicating the cause of the high initial maximum erosion rate. Suggesting, planer surface grinding prior to erosion testing would remove poorly adhered particle splats and result in an immediate terminal erosion behaviour.

4.6.2 Modified Stand-off Distance

Coatings with a modified stand-off distances were selected for erosion testing to determine the effect of stand-off distance on erosion resistance. The coatings were tested in the ground condition and compared to the standard coating in the as-sprayed condition. Coatings with porosity above one percent were not selected for erosion testing since

excessive porosity is a good indicator of poor coating quality and thus would not pass preliminary evaluation. This resulted in the following tested conditions; 10” SD (as-sprayed), 10” SD (ground), 8” SD (ground), and 6” SD (ground). Due to the robustness of the coating the erosion testing was extended to 300 minutes, which resulted in a total volumetric loss of 0.4705 mm^3, 0.1938 mm^3, 0.1468 mm^3, and 0.2488 mm^3 for the 10” SD (as-sprayed), 10” SD (ground), 8” SD (ground), and 6” SD, respectively, represented in Figure 102. This resulted in a steady-state rate of erosion for all coatings tested in the ground condition with a terminal erosion rate comparable to that of the 10” SD (as-sprayed) coating. The maximum and terminal erosion rates, along with the calculated minimum test durations are summarized in Table 27 and while the erosion rates are plotted in Figure 103.

The erosion rates were also normalized to toughmet in the uncoated condition to determine the improvement of erosion resistance with the implementation of the modified coating. This resulted in 14.9 fold improvement of maximum erosion rate and 24.75 fold improvement of terminal erosion rate of the coating in the as-sprayed condition over the uncoated toughmet, as mentioned in the previous section. When the same coating was tested in the ground condition the improvement of maximum erosion resistance soars to 139.2 fold with an improvement in terminal erosion of 33.0 fold. When the stand-off distance was decreased to eight inches the normalized maximum erosion rate spikes to 167.0 times with a terminal erosion rate improvement of 39.6 times. When the stand-off distance was further decreased to six inches the normalized maximum erosion rate falls to 104.4 and the normalized terminal erosion rate decreases to 24.75. For easy of accessibility these results have been summarized in Table 28 and Figure 104. This suggests the removal of surface asperities has a significant impact on the erosion resistance and should be

completed to keep components within tolerance. Furthermore, the stand-off distance impact the erosion resistance of deposited coatings with a stand-off distance of eight inches obtaining the highest erosion resistance of all tested materials and coatings.

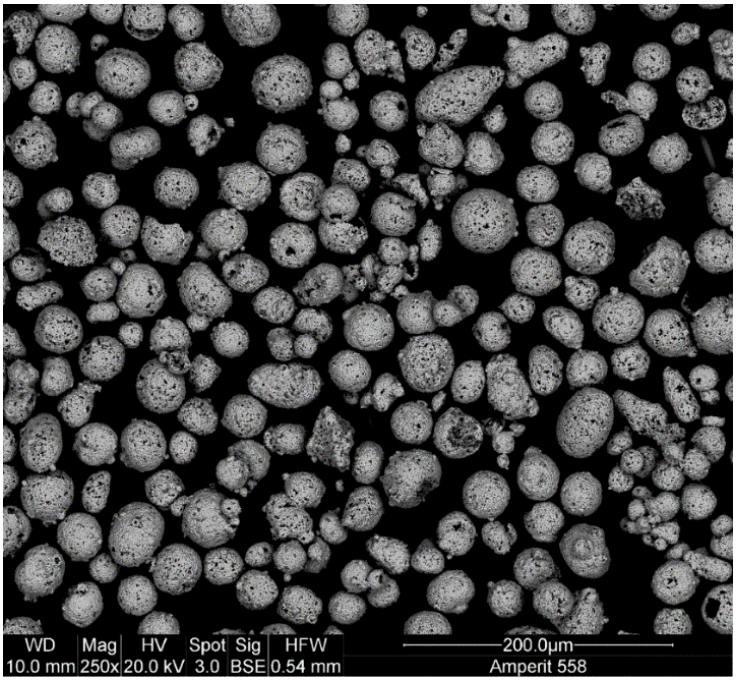

Figure 43 - SEM observation of Amperit 558 feedstock.

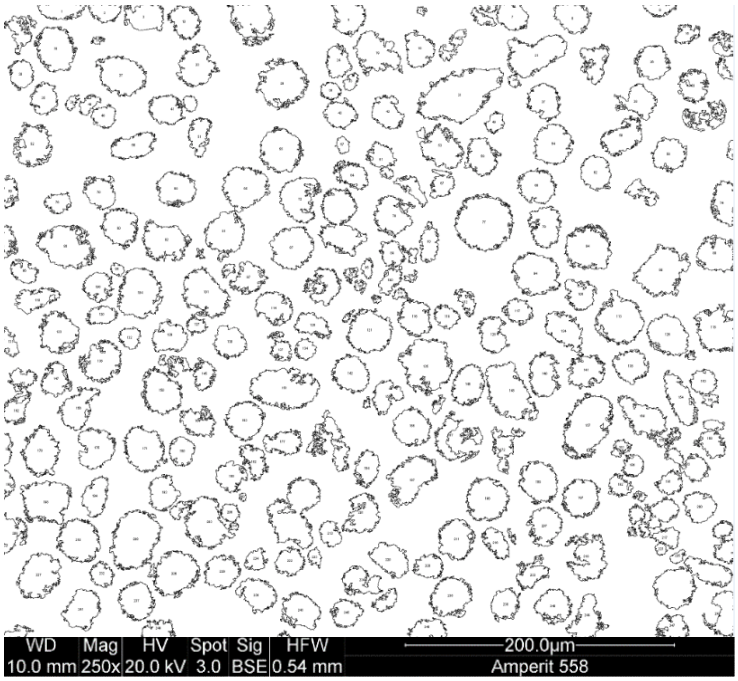

Figure 44 - Processed image of Amperit 558 feedstock using ImageJ.

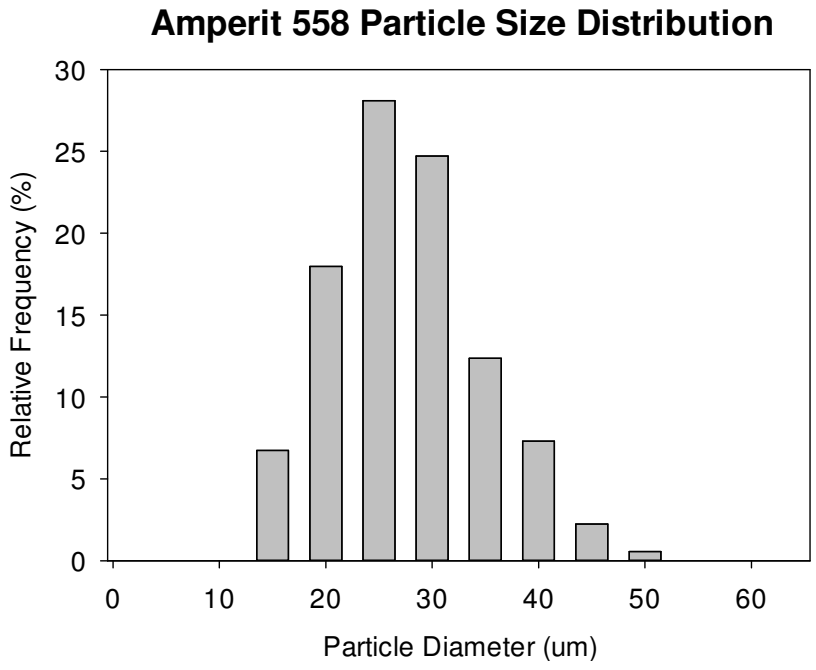

Figure 45 - Relative frequency (%) of particle diameter (um) of Amperit 558.

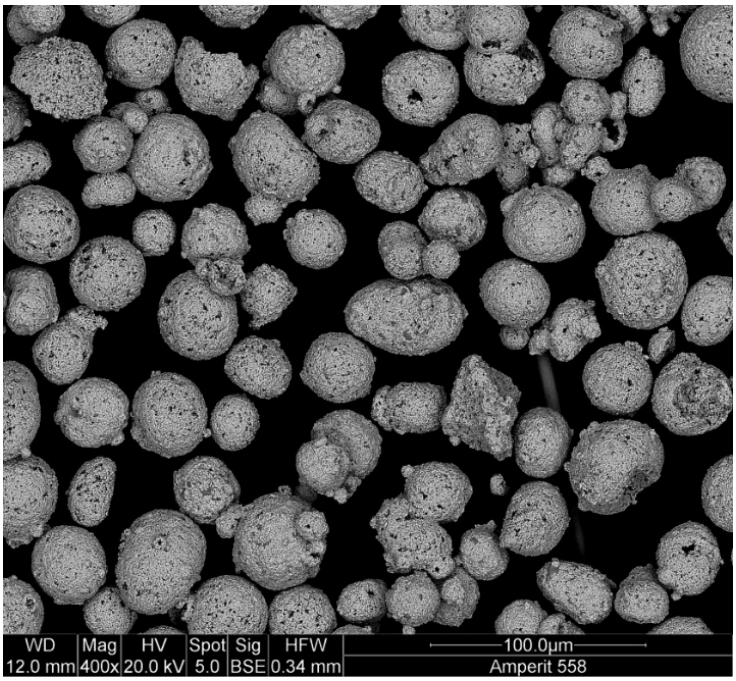

Figure 46- SEM image of amperit 558 prior to EDS analysis.

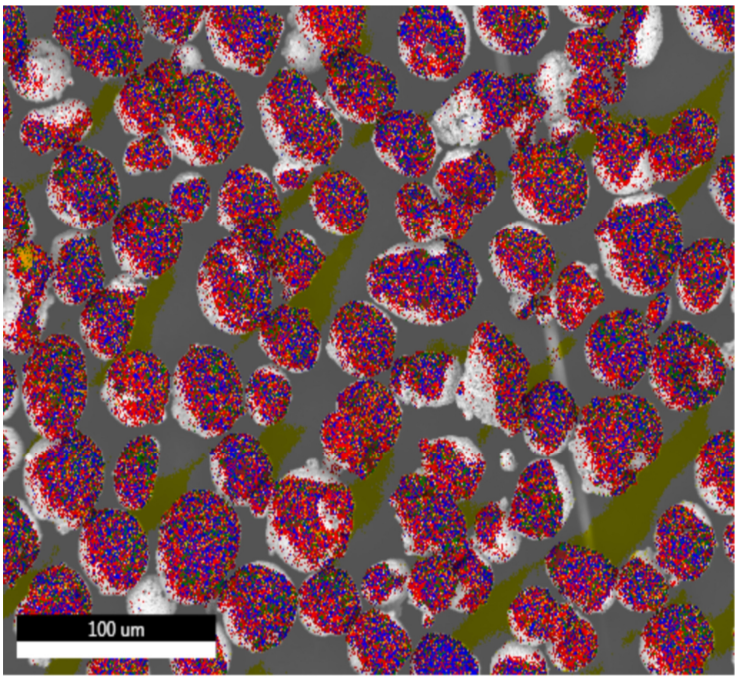

Figure 47 - EDS composition map colour coded based on detected compositions (Table 7).

Table 7- Legend of EDS elemental map for Figure 47.

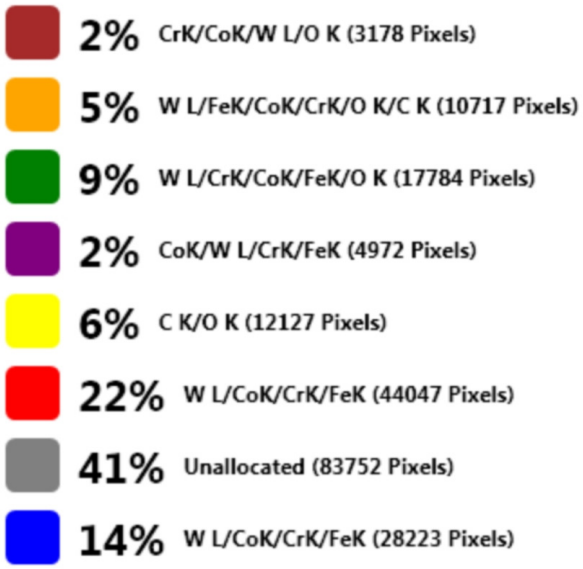

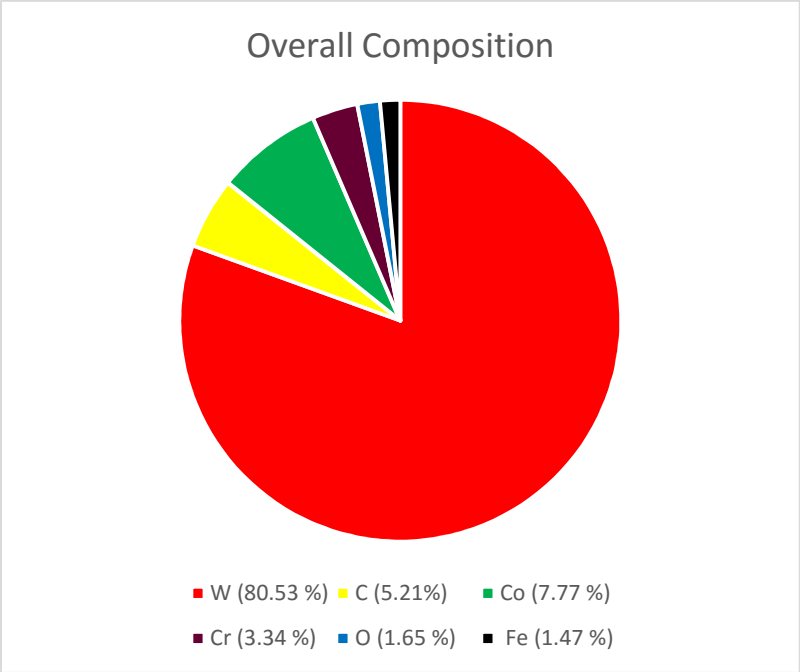

Figure 48 - Overall composition of amperit 558 feedstock in percent weight.

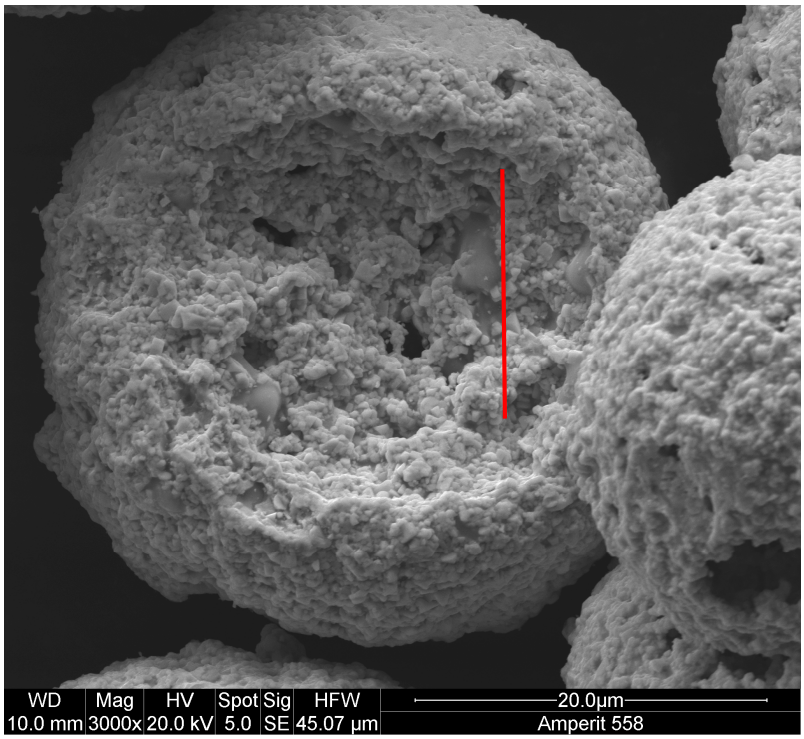

Figure 49 - SEM image of densely packed solid particle at 3000 X magnification.

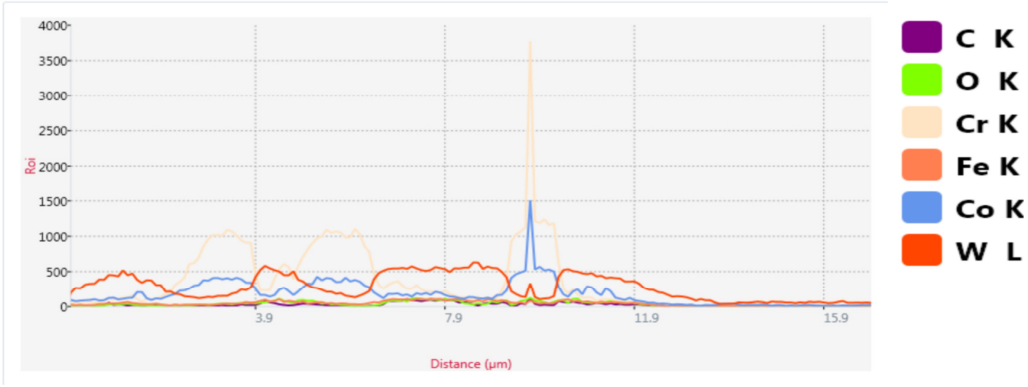

Figure 50 – EDS line scan of densely packed solid particle composition at 300 X (indicated by red line on previous image).

Figure 51- SEM image of porous solid particle at 3000 X.

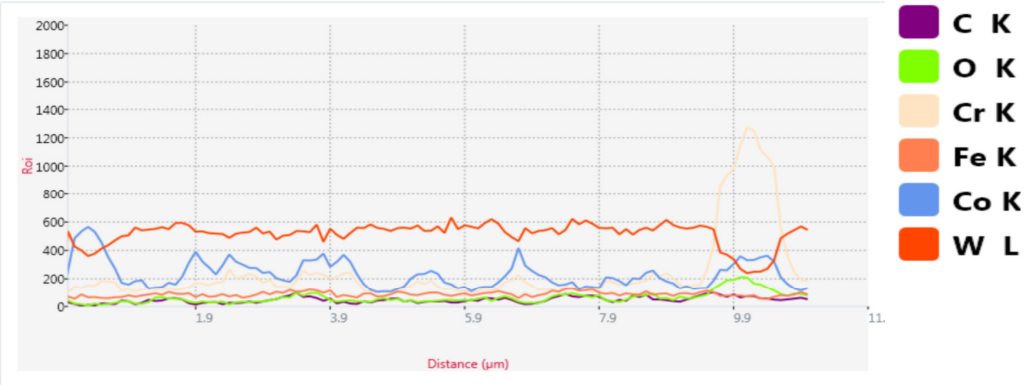

Figure 52 – EDS line scan of porous solid particle composition at 3000 x (indicated by red line on previous image).

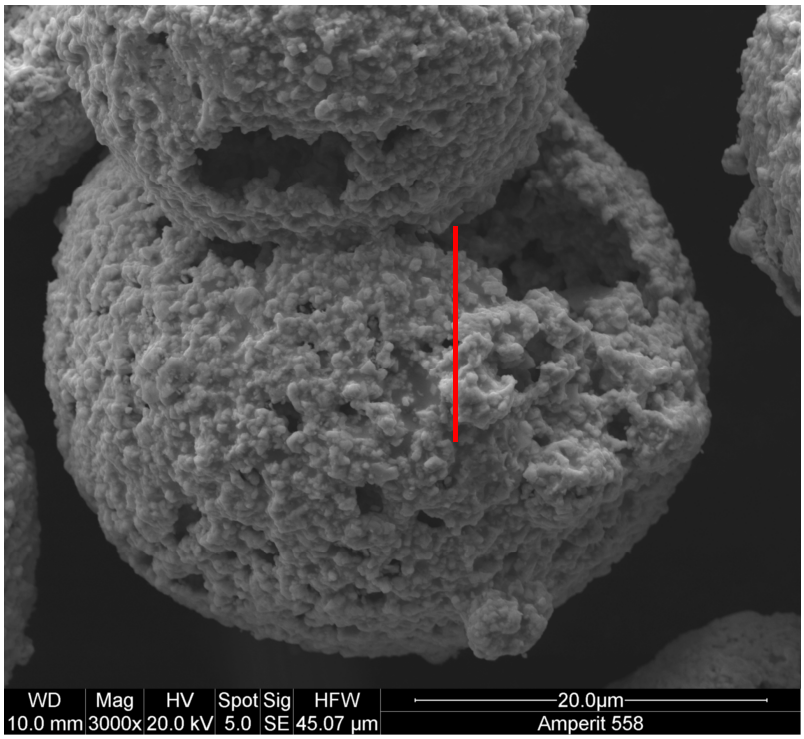

Figure 53- SEM image of porous hollow particle at 3000 X.

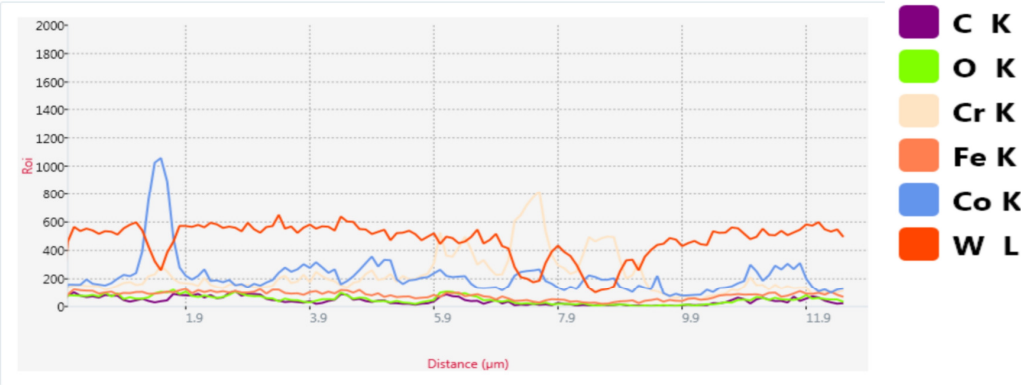

Figure 54 – EDS line scan of porous hollow particle composition at 3000 x (indicated by red line on previous image).

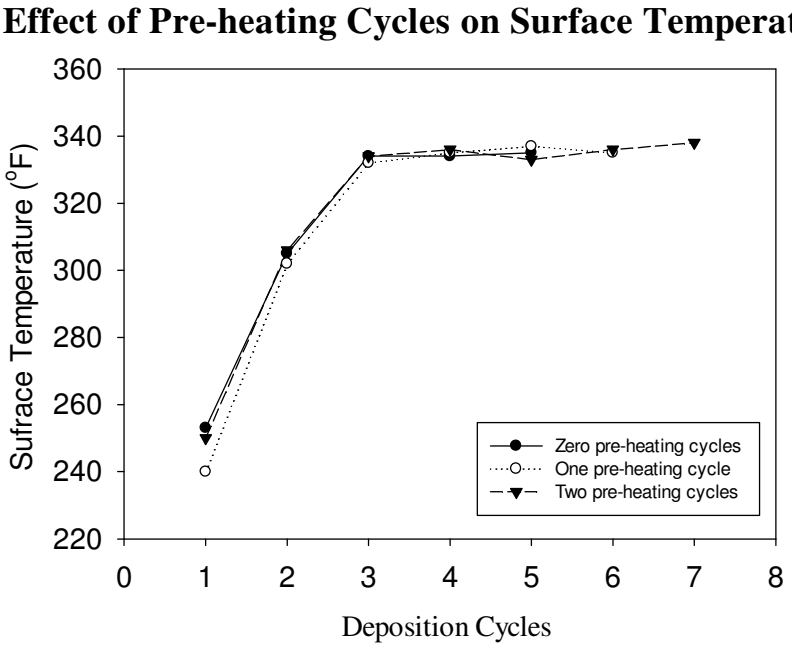

Figure 55 – Effect of pre-heating cycles on surface temperature, measured using a mounted infrared thermometer aimed at the center of the work-piece after the completion of each deposition cycle, coated using the standard deposition parameters with a stand-off distance of ten inches.

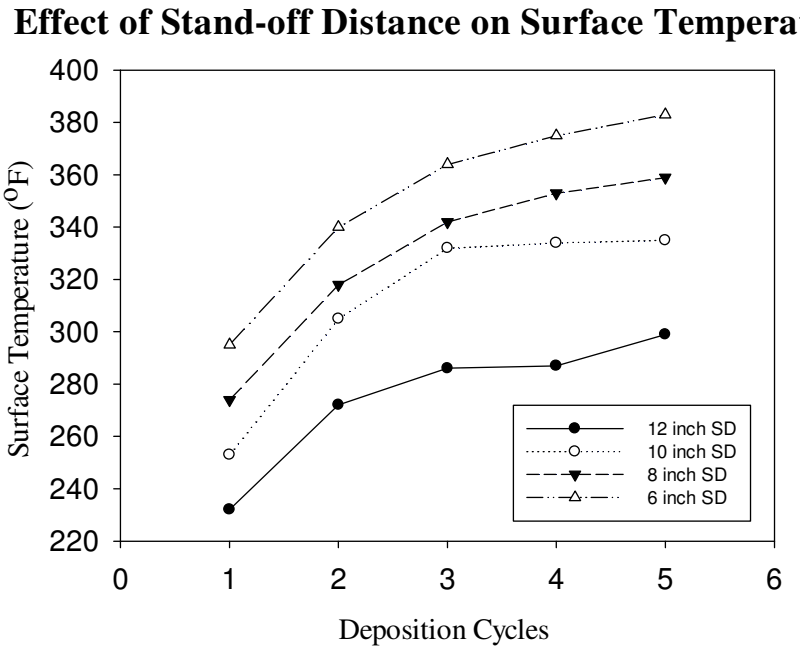

Figure 56 - Effect of stand-off distance on surface temperature, measured using a mounted infrared thermometer aimed at the center of the work-piece after the completion of each deposition cycle, coated using the standard deposition parameters.

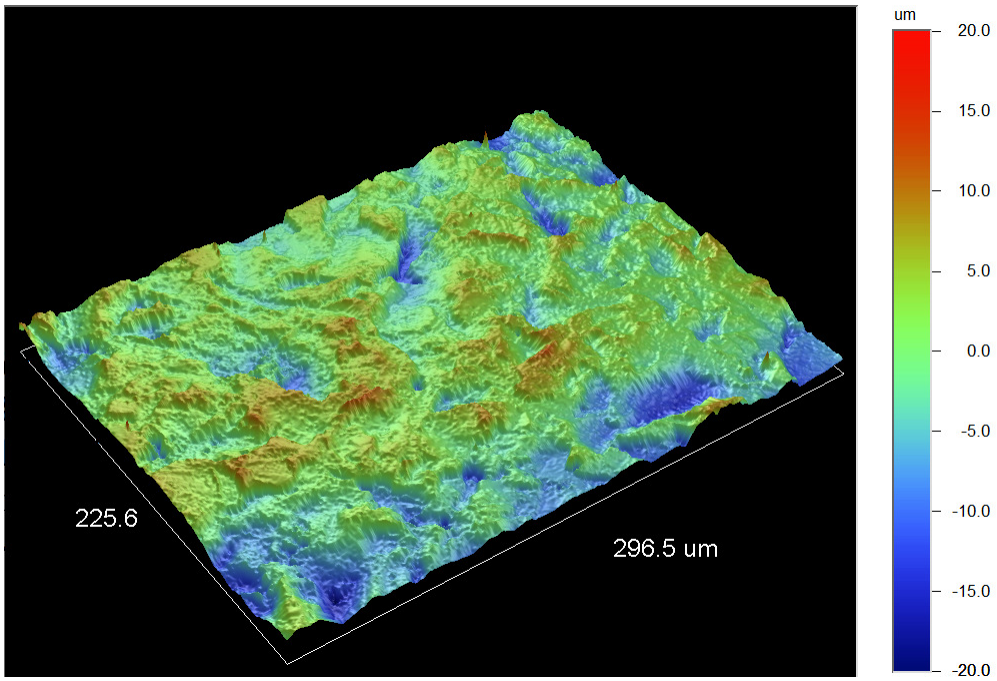

Figure 57 - Three-dimensional topography of grit blasted toughmet at 20 X.

Table 8 – Average surface roughness from three measurements of pre spray treated toughmet.

Sample	R_a (um)	R_{RMS} (um)
Pre-spray treated toughmet	3.46 ± 0.24	4.56 ± 0.28

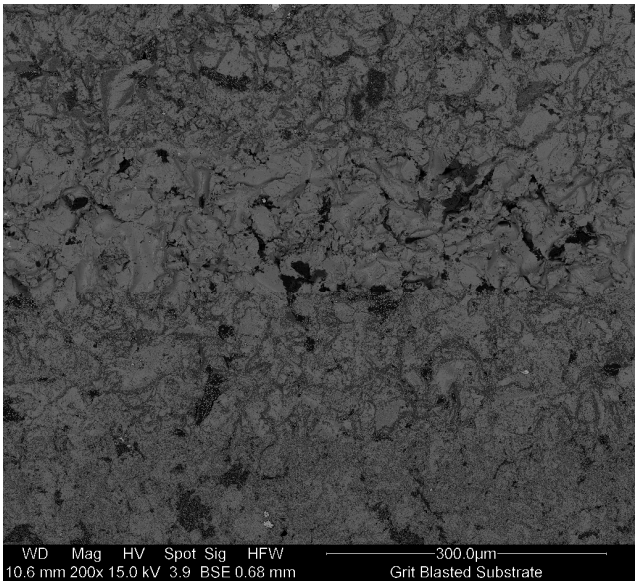

Figure 58 - SEM image of grit blasted substrate at 200 X (top view).

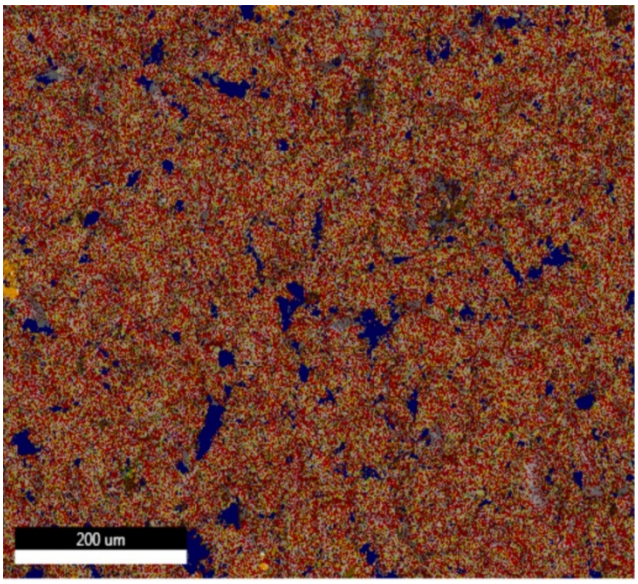

Figure 59 - EDS map of grit blasted substrate at 200 X colour coded based on detected composition (Table 9), where the blue region represents embedded blasting media in the substrate

Table 9 – Legend of EDS map of grit blasted substrate for Figure 59.

3%	O K/AlK/CuK/SiK/SnL/NiK (6499 Pixels)
41%	CuK/NiK/SnL (84280 Pixels)
17%	CuK/NiK/SnL/AlK (35447 Pixels)
2%	CuK/FeK/NiK/SnL/AlK/O K (4228 Pixels)
28%	Unallocated (58081 Pixels)
6%	AlK/O K/CuK (13240 Pixels)
0%	O K/FeK/AlK/CuK/SnL (114 Pixels)
1%	SiK/AlK/CuK/O K/SnL (2892 Pixels)

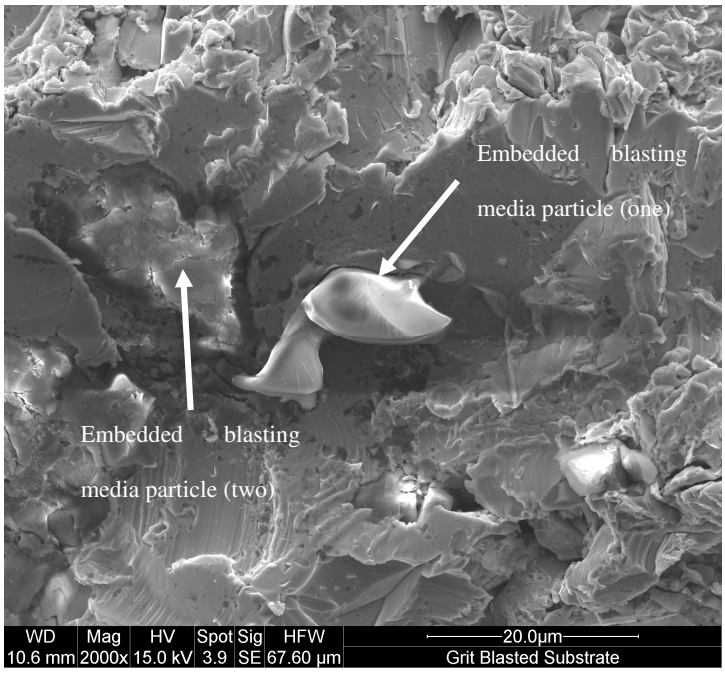

Figure 60 - SEM image of blasting media particles embedded into substrate due to mechanical roughening prior to coating application at 2000 X.

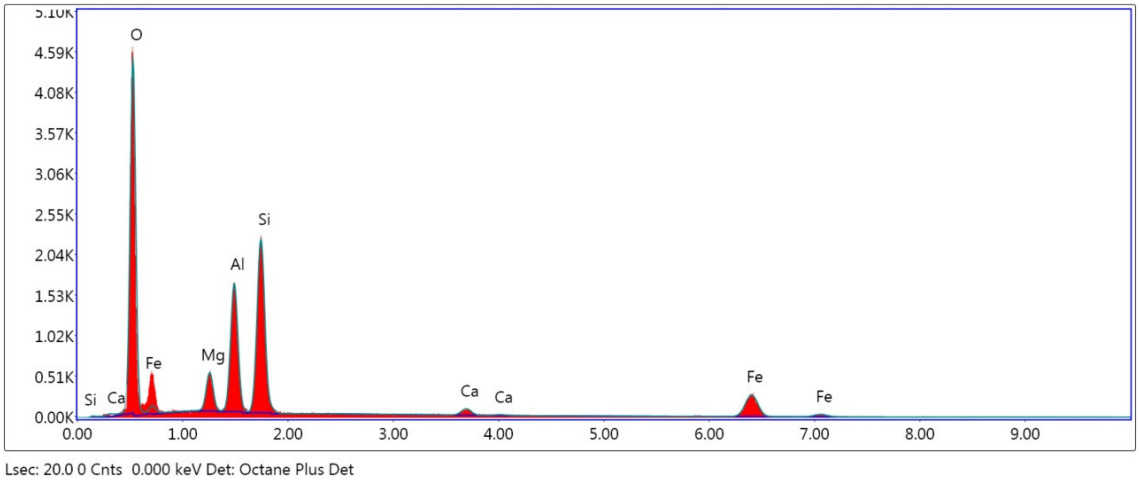

Figure 61 – EDS spectrum of embedded blasting media particle (one) from Figure 60.

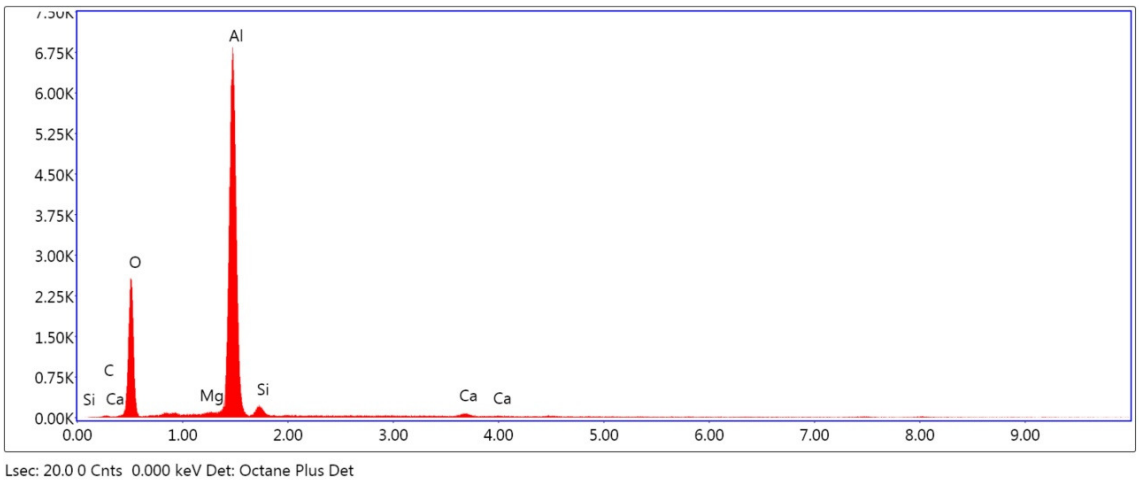

Figure 62 - EDS spectrum of embedded blasting media particle (two) from Figure 60.

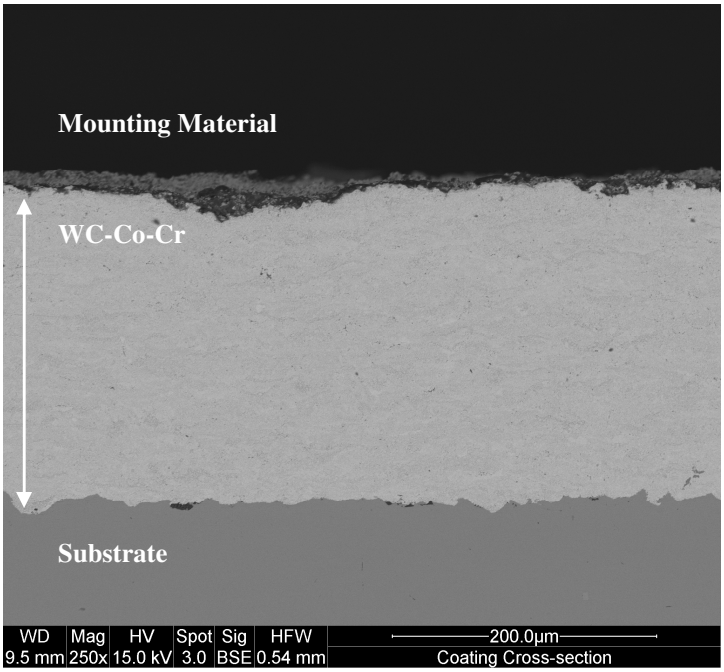

Figure 63 – SEM image of coating cross-section at 250 X.

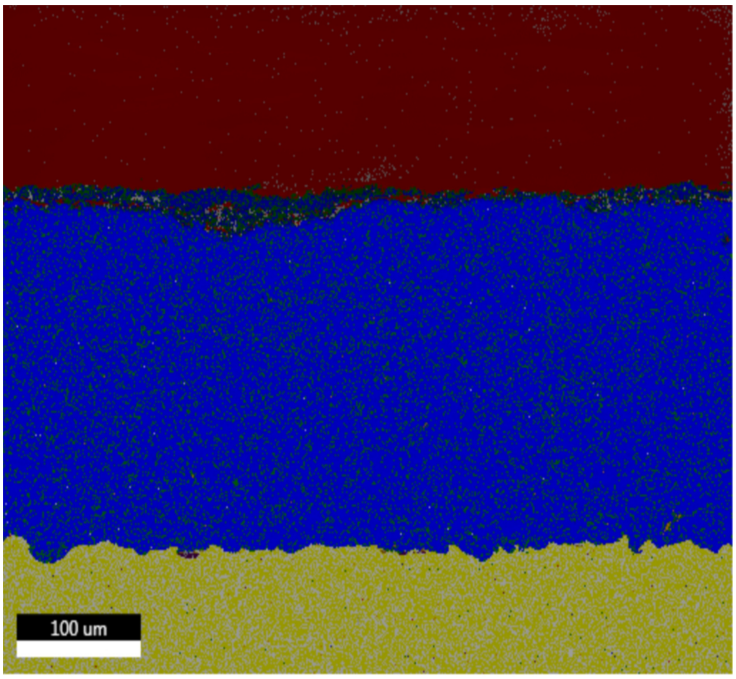

Figure 64 - EDS map of coating cross-section (Figure 63).

Table 10 - Legend of EDS map for coating cross-section from Figure 64.

0%	CrK/O K/CuK/W M/NiK/CoK (127 Pixels)
7%	Unallocated (14919 Pixels)
44%	W M/CoK (90469 Pixels)
12%	CuK/NiK (24426 Pixels)
9%	W M/CoK/CrK (18358 Pixels)
28%	C K/O K (56444 Pixels)

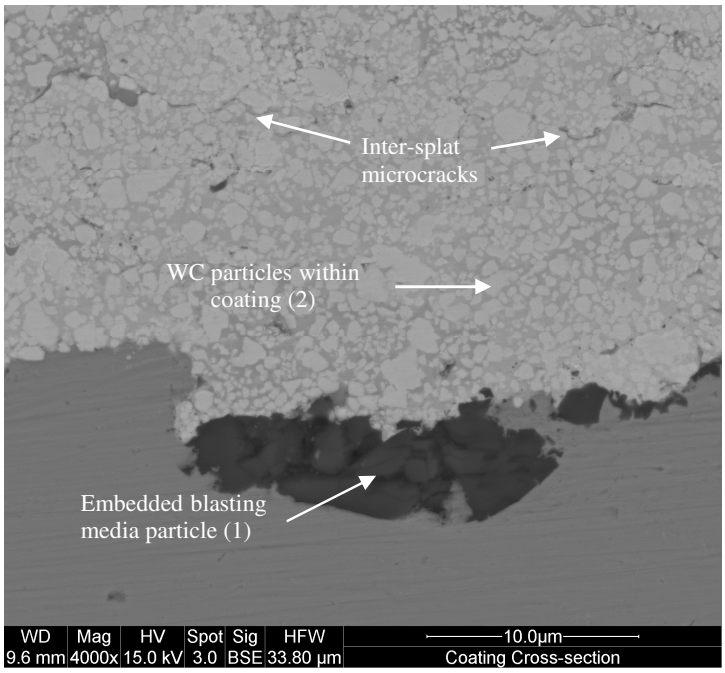

Figure 65 - SEM image of coating cross-sectional interface at 400 X.

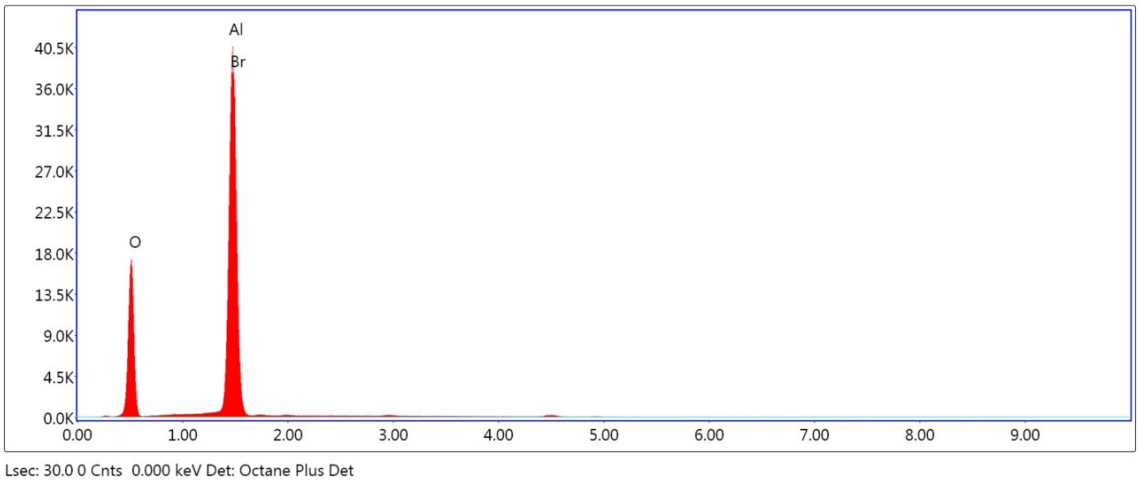

Figure 66 – EDS spectrum of location embedded blasting media particle (indicating Al_2O_3 particle) of SEM coating interface.

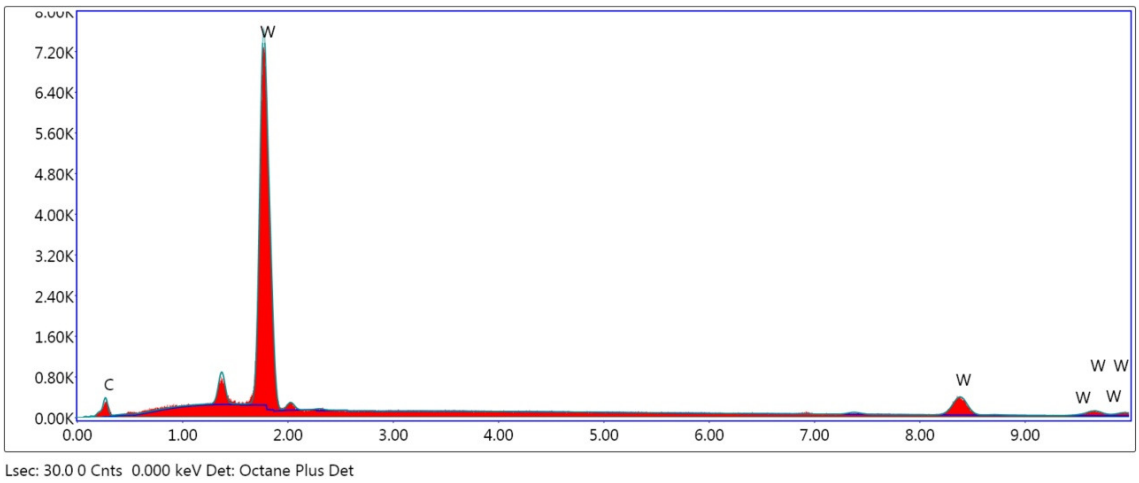

Figure 67 – EDS spectrum of location 2 (indicating WC particle) of SEM coating interface.

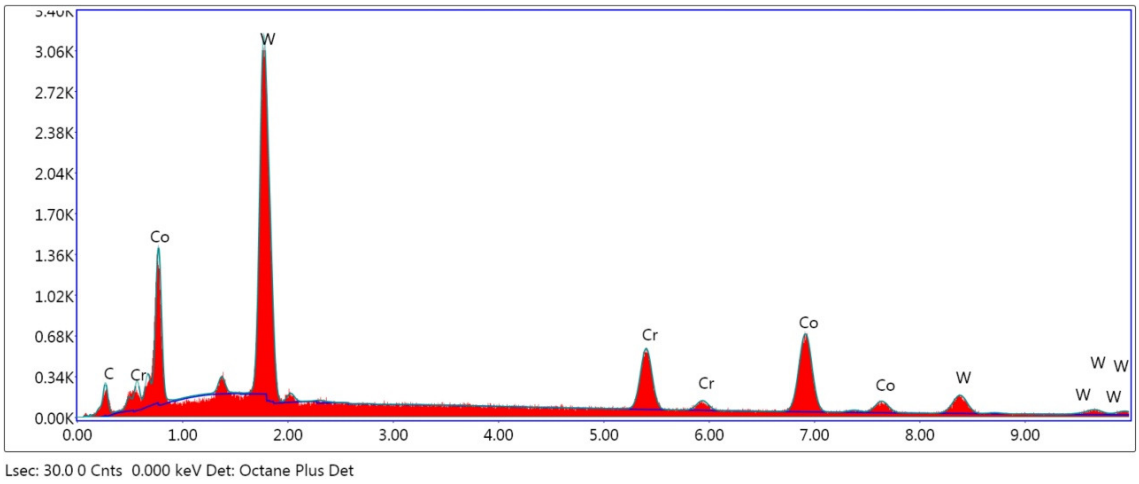

Figure 68 - EDS spectrum of dark grey region surrounding WC particles.

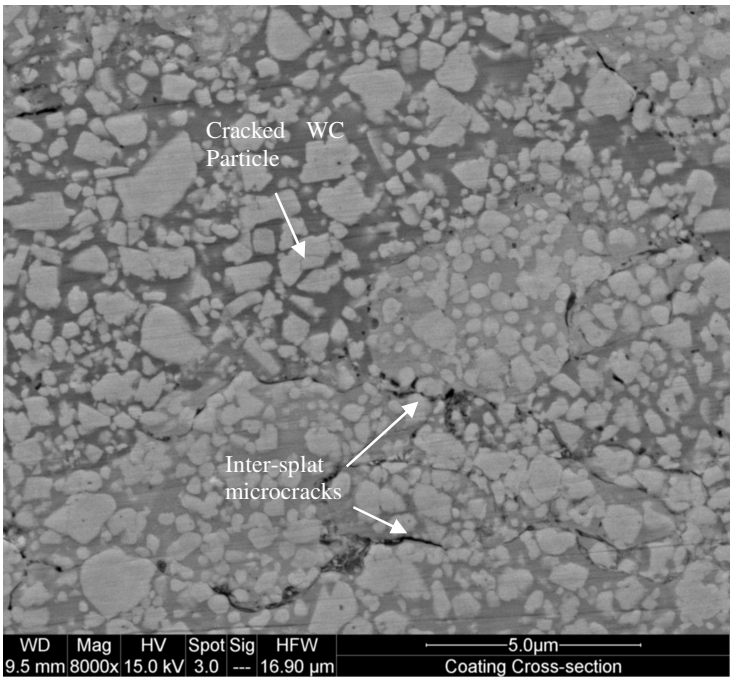

Figure 69 – SEM image of coating cross-section depicting inter-splat microcracks and a cracked WC particle at 8000 X.

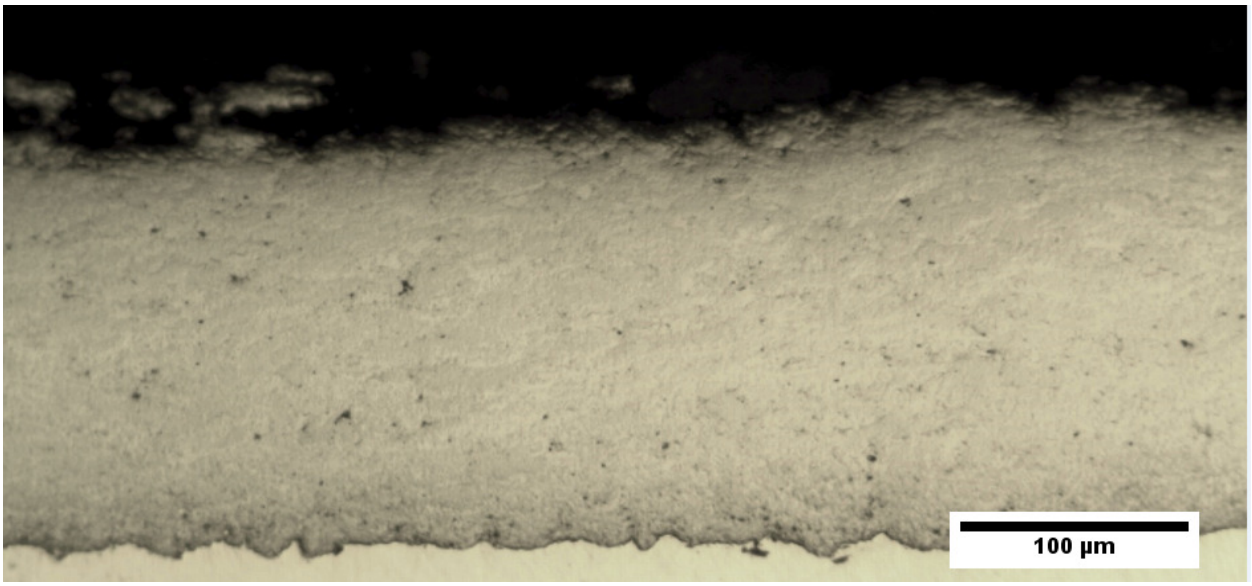

Figure 70 - Optical image of coating cross-section of coating with standard deposition techniques (stand-off distance: 10") at 20 X.

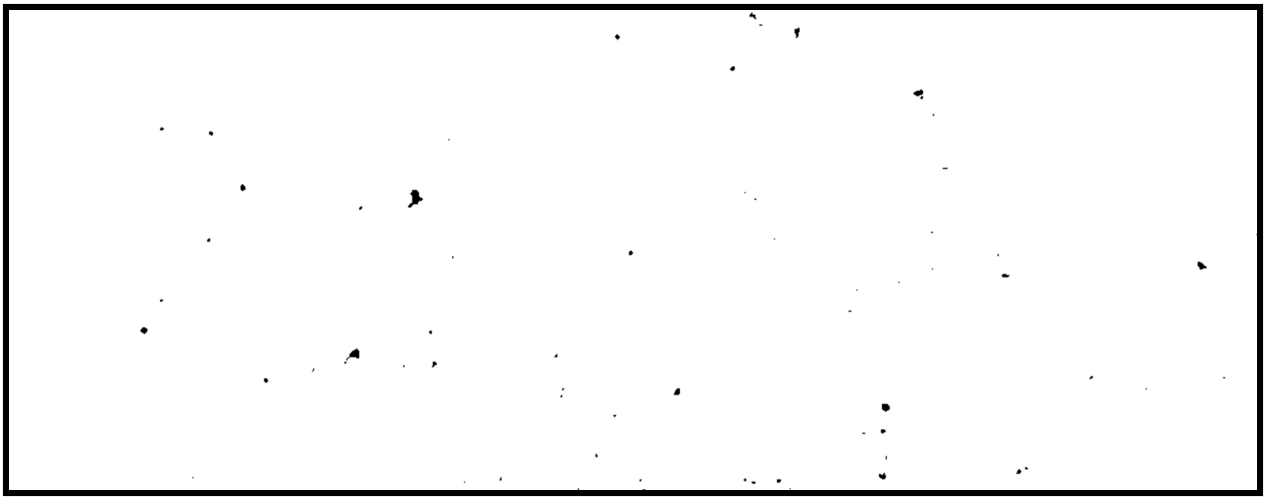

Figure 71 – Processed image of optical image of standard coating cross-section (Figure 70), black pixels represent voids and or pores within the coating cross-section.

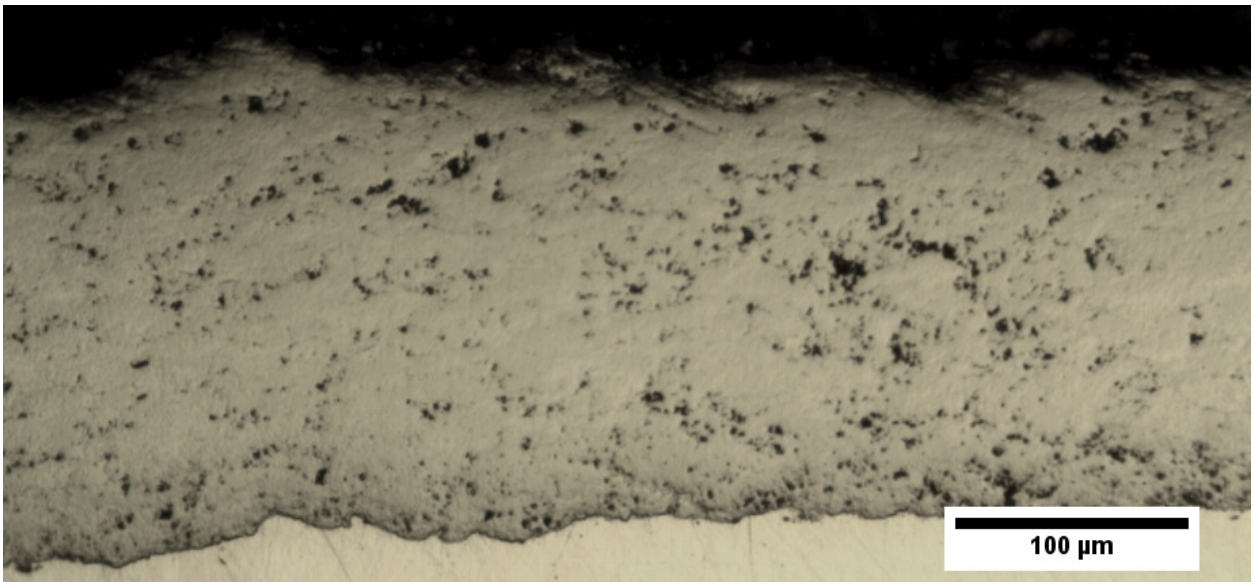

Figure 72 - Optical image of coating cross-section with one pre heating cycle at a stand-off distance on 10" at 20 X.

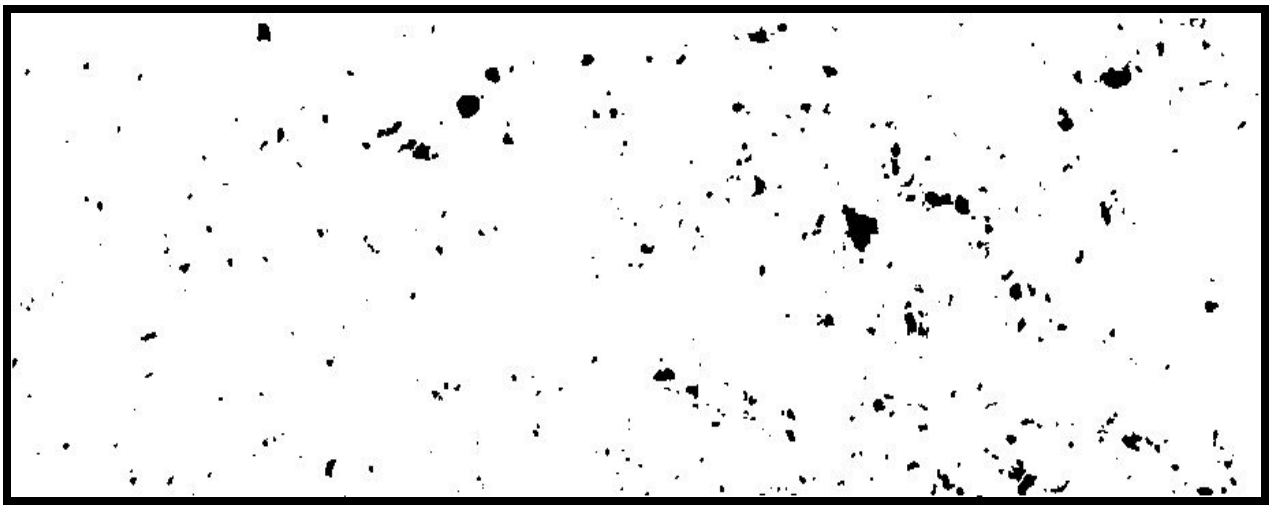

Figure 73 – Processed image of optical image of coating with one pre heating cycle (Figure 72), black pixels represent voids and or pores within the coating cross-section.

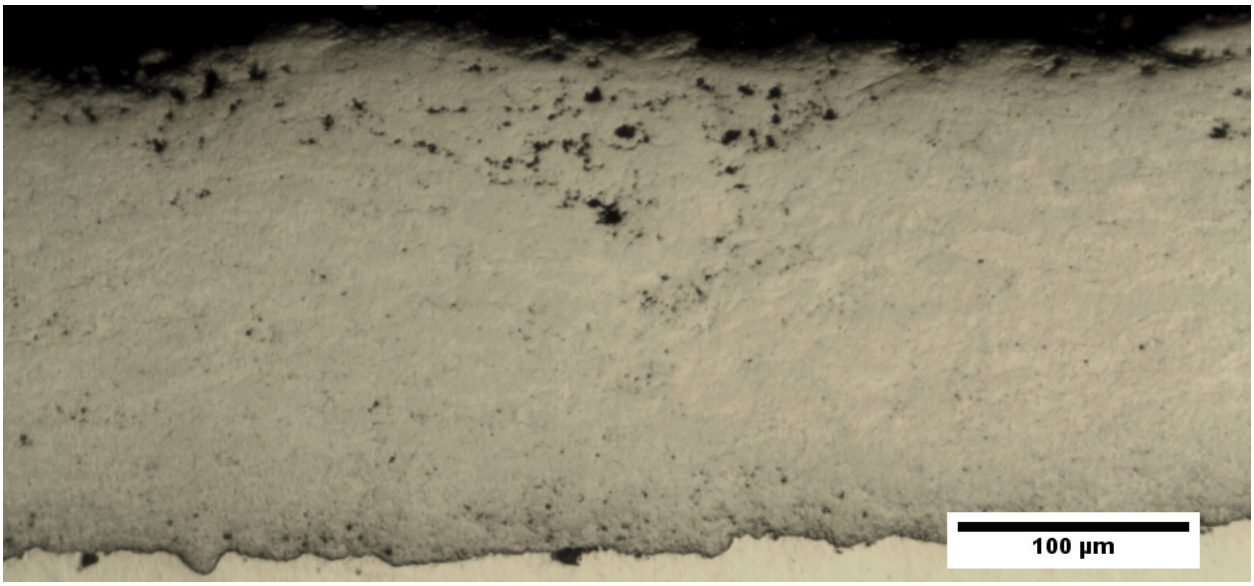

Figure 74- Optical image of coating cross-section with two pre heating cycle at a stand-off distance on 10" at 20 X.

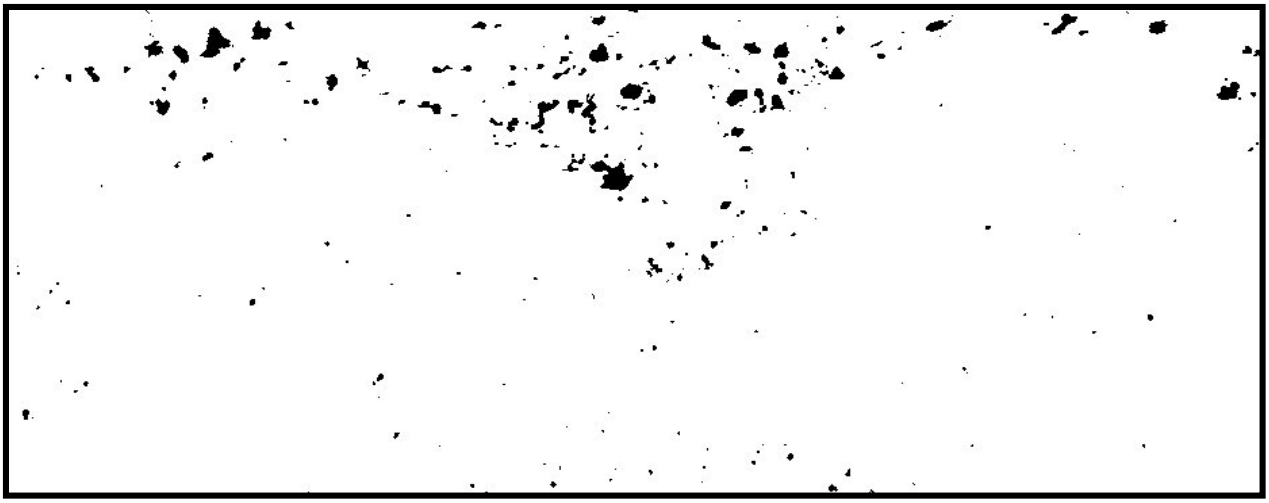

Figure 75– Processed image of optical image of coating with two pre heating cycles (Figure 74), black pixels represent voids and or pores within the coating cross-section.

Table 11 - Effect of pre-heating cycles on coating porosity, calculated using Image J from optical images of coating cross-sections.

Sample	Coating Porosity
No pre-heating cycles	0.423 ± 0.01
1 pre-heating cycle	2.255 ± 0.01
2 Pre-heating cycles	1.579 ± 0.01

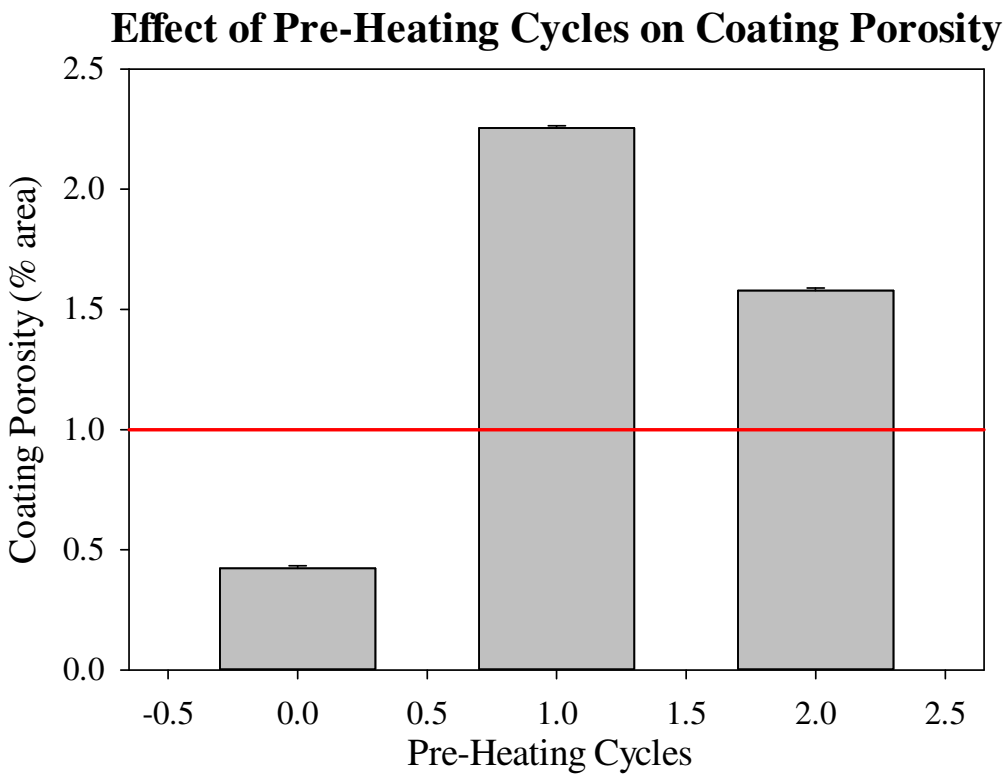

Figure 76 - Effect of pre-heating cycles on coating porosity, calculated using Image J from optical images of coating cross-section (red line indicates the desired minimum porosity of 1 (% area)).

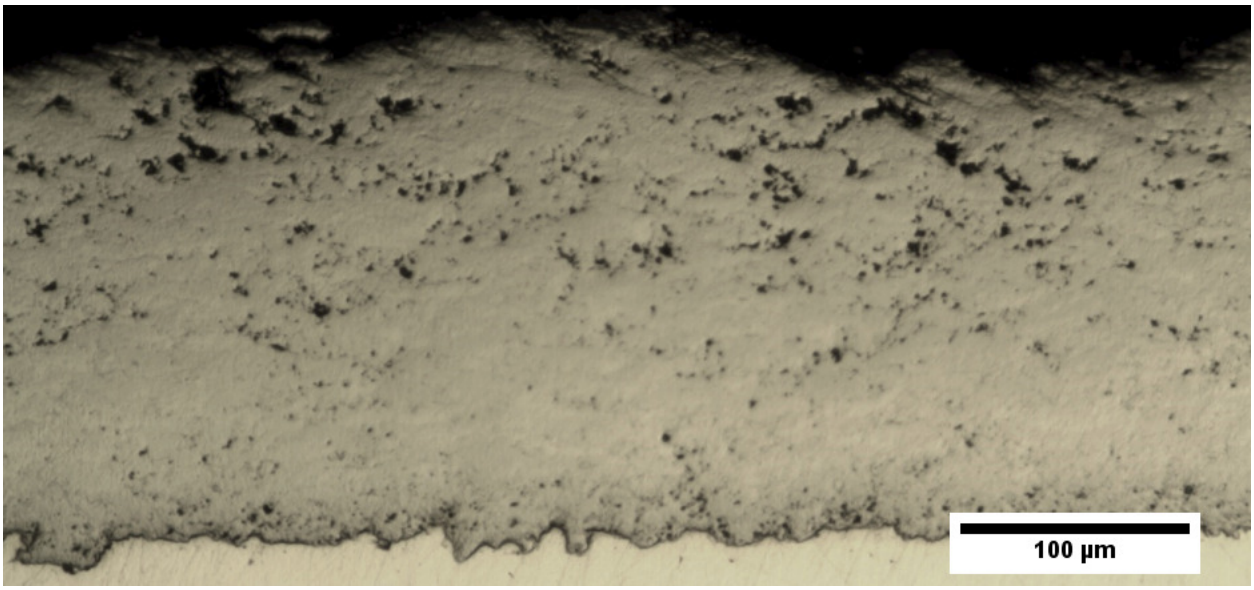

Figure 77 - Optical image of coating cross-section with modified stand-off distance (12") at 20 X.

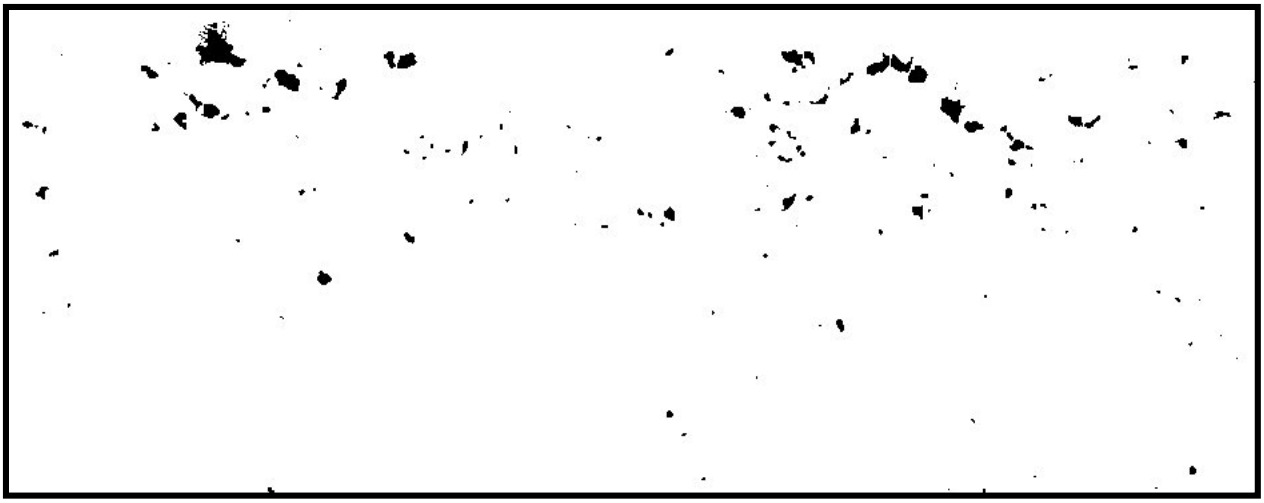

Figure 78 – Processed image of optical image of coating cross-section with a modified stand-off distance of 12 inches (Figure 77), black pixels represent voids and or pores within the coating cross-section.

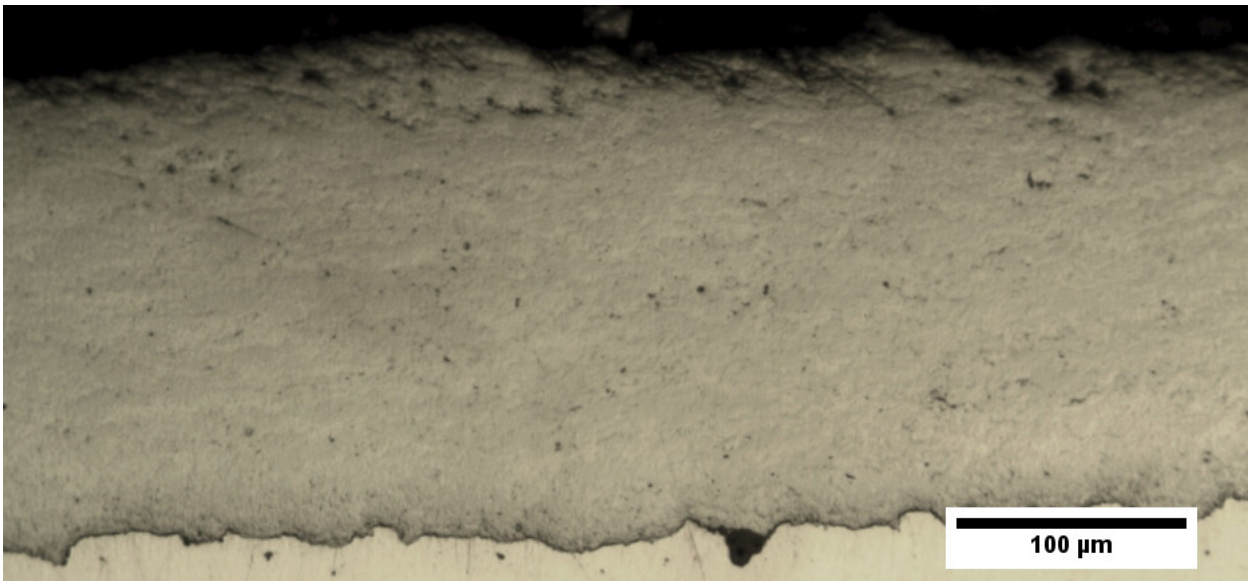

Figure 79 - Optical image of coating cross-section with a modified stand-off distance (8") at 20 X.

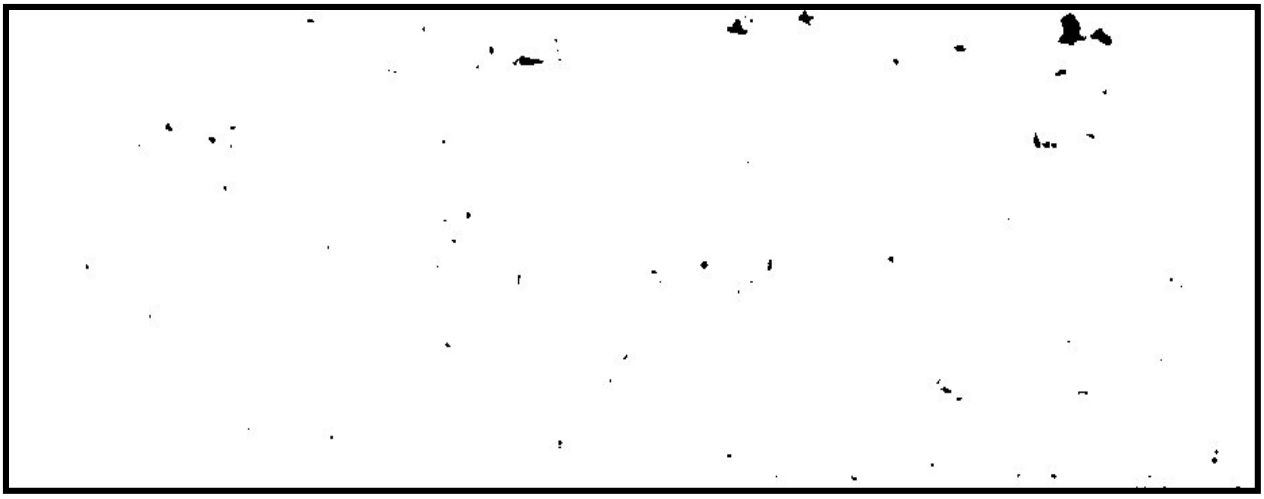

Figure 80 – Processed image of optical image of coating cross-section with a modified stand-off distance of 8 inches (Figure 79), black pixels represent voids and or pores within the coating cross-section.

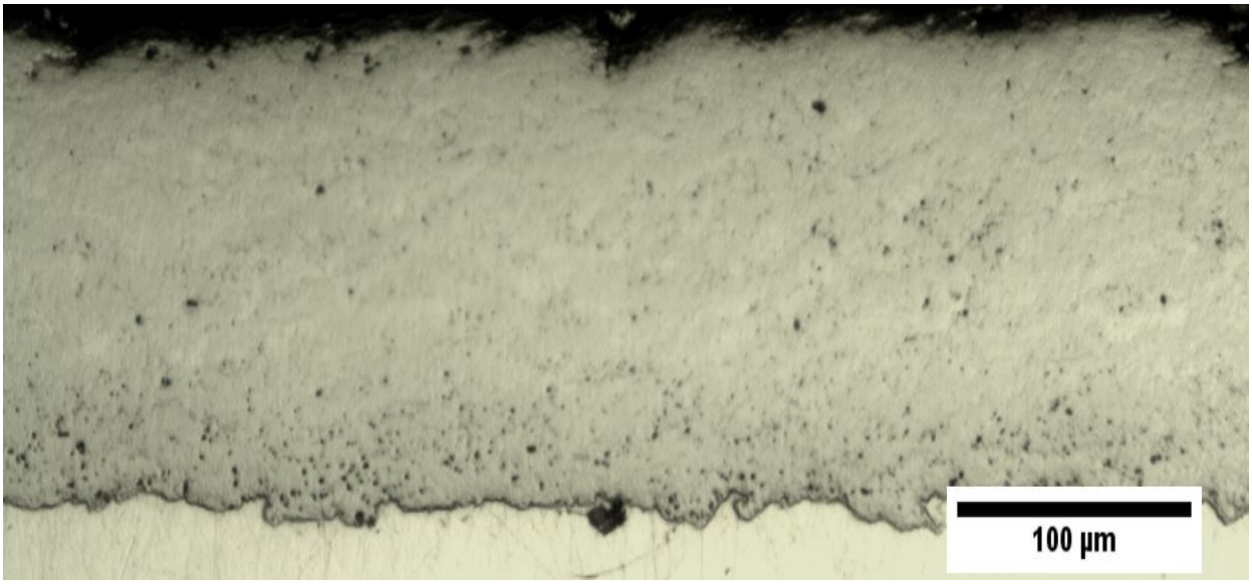

Figure 81 - Optical image of coating cross-section with modified stand-off distance (6") at 20 X.

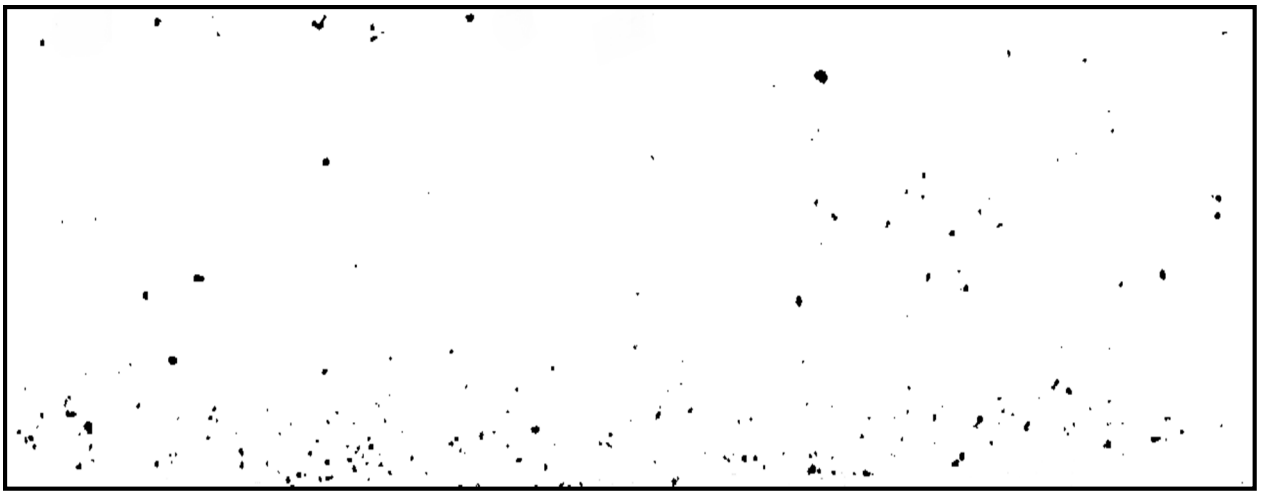

Figure 82– Processed image of optical image of coating cross-section with a modified stand-off distance of 6 inches (Figure 81), black pixels represent voids and or pores within the coating cross-section.

Table 12 – Effect of stand-off distance on coating porosity, calculated using Image J from optical images of coating cross-section.

Sample	Coating Porosity
6 in stand-off distance	0.716 ± 0.01
8 in stand-off distance	0.334 ± 0.01
10 in stand-off distance	0.423 ± 0.01
12 in stand-off distance	1.212 ± 0.01

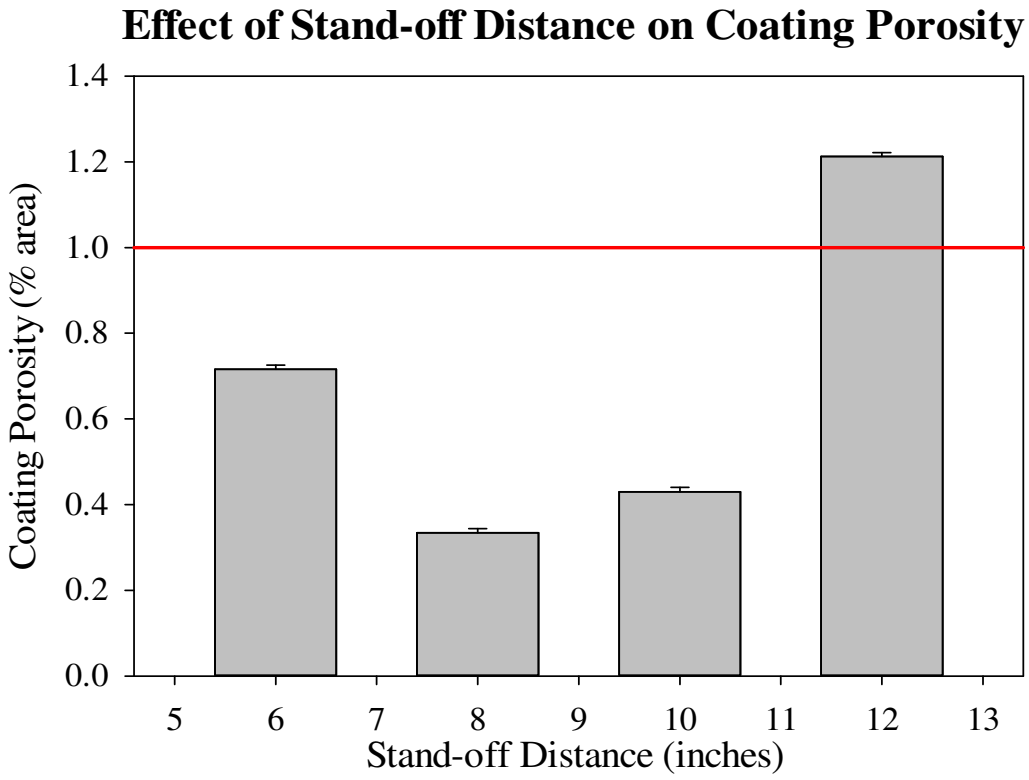

Figure 83 - Effect of stand-off distance on coating porosity, calculated using Image J from optical images of coating cross-section (red line indicates the desired minimum porosity of 1 (% area)).

Table 13 – Effect of pre-heating cycles conducted prior to coating deposition on coating density, the coating density was measured according to ASTM B962 using Archimedes method.

Pre Heating cycles	Average Density (g/cm^3)	Standard Deviation
0	12.783	0.009
1	12.349	0.167
2	12.697	0.175

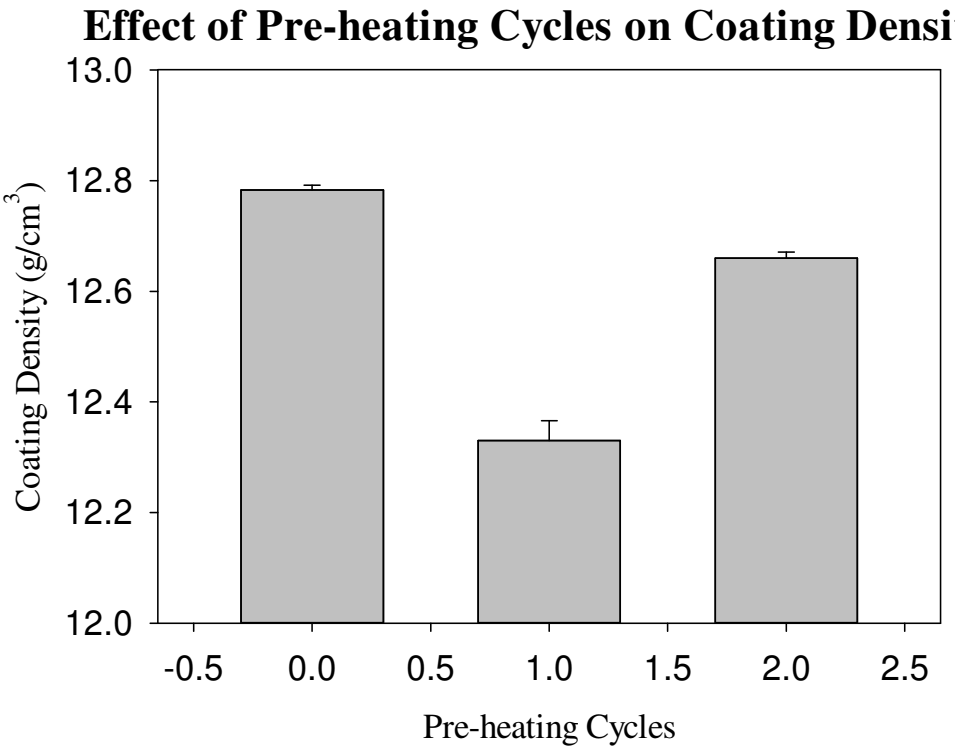

Figure 84 – Effect of pre-heating cycles conducted prior to coating deposition on coating density, coating density measured according to ASTM B962 using Archimedes method.

Table 14 - Effect of stand-off distance on coating density, the coating density was measured according to ASTM B962 using Archimedes method.

Stand-off distance (in)	Average Density (g/cm^3)	Standard Deviation
6	12.730	0.029
8	12.827	0.004
10	12.783	0.009
12	12.650	0.043

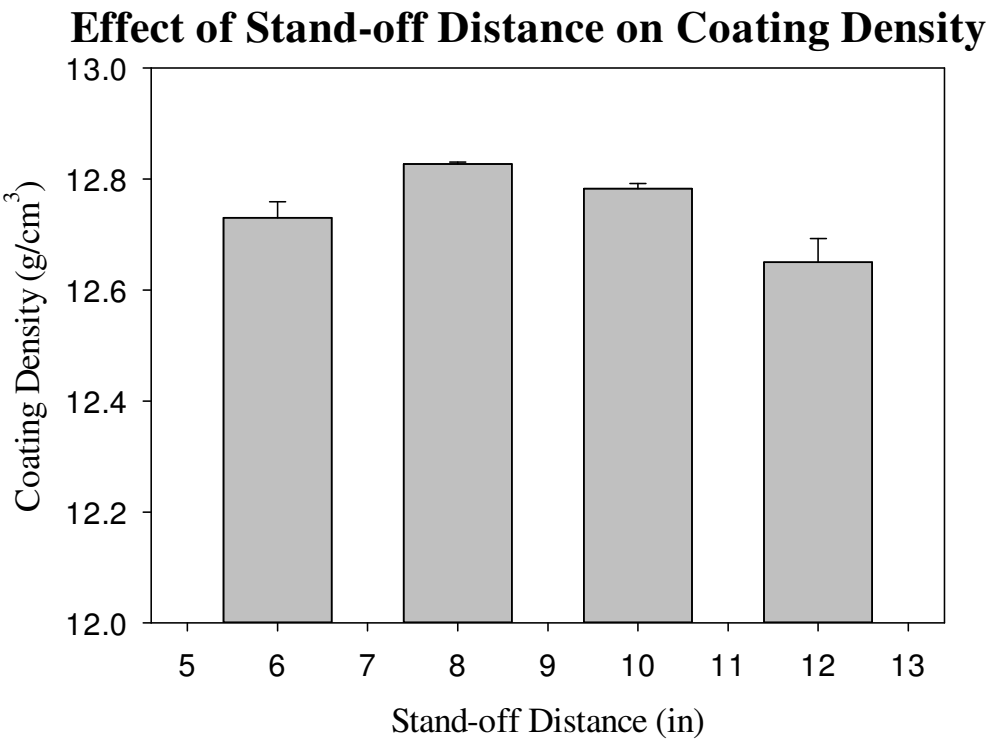

Figure 85- Effect of stand-off distance on coating density, coating density measured according to ASTM B962 using Archimedes method.

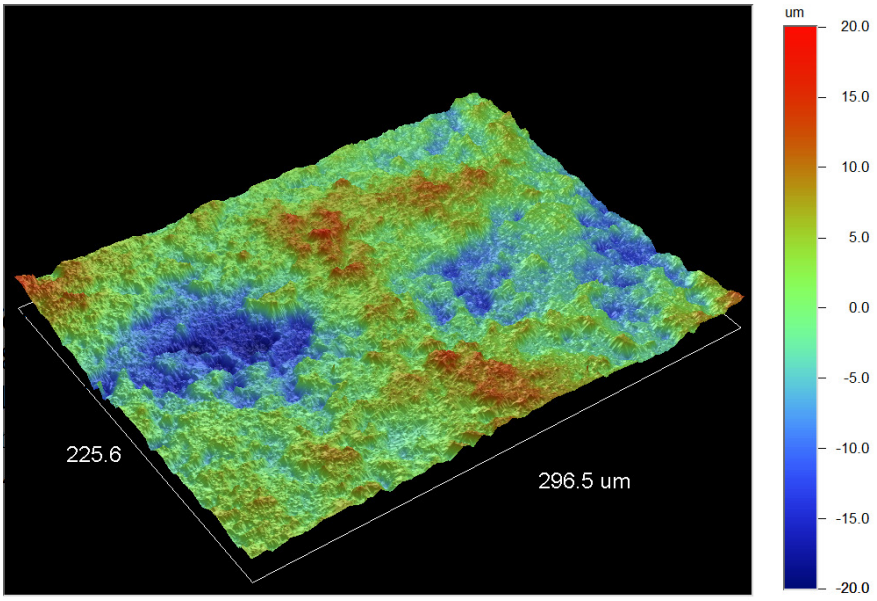

Figure 86 - Three-dimensional topography of WC-Co-Cr TS coating in the as-sprayed condition at 20 X.

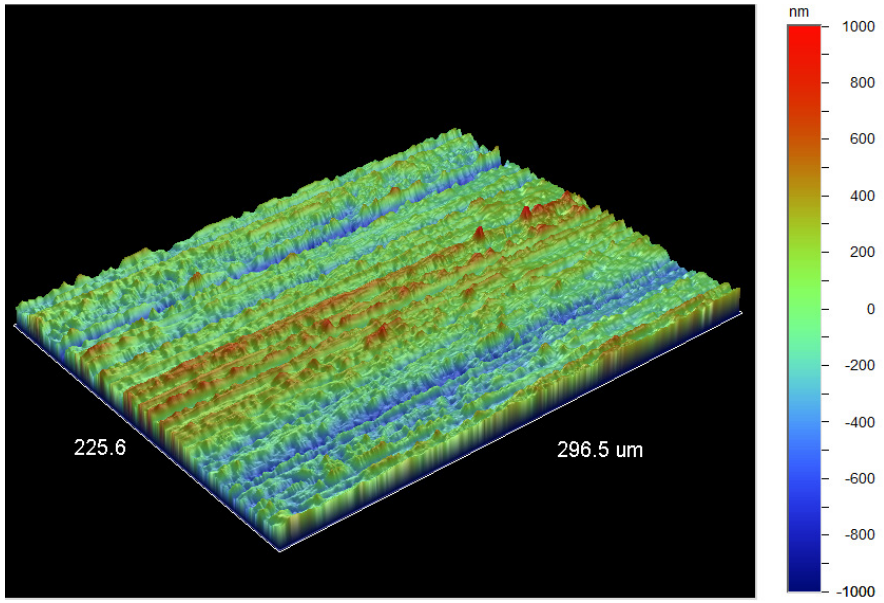

Figure 87 - Three dimensional topography of WC-Co-Cr TS coating in the ground condition at 20 X.

Table 15 - Average surface roughness of standard coating, measured by calculating the average of three surface measurements using an optical profilometer.

Sample	Ra (um)
WC-Co-Cr Coating (as-sprayed)	4.49 ± 0.63
WC-Co-Cr Coating (ground)	0.249 ± 0.02

Table 16 – Uncoated toughmet and standard WC-Co-Cr coating hardness measured according to ASTM E-18.

Sample	Macro-Hardness (HRA)
Uncoated Toughmet	64.33 ± 0.12
Coated Substrate (as-sprayed)	79.80 ± 0.51
Coated Substrate (ground)	74.40 ± 0.00

Table 17 –Effect of pre-heating cycles on coating hardness in the as-sprayed condition.

Number of Pre-heating Cycles	Macro-Hardness (HRA)
0	79.80 ± 0.51
1	78.73 ± 0.12
2	80.67 ± 0.26

Table 18 - Effect of stand-off distance on coating hardness in the as-sprayed condition.

Stand-off Distance (inches)	Macro-Hardness (HRA)
6	80.70 ± 0.65
8	80.33 ± 0.54
10	79.80 ± 0.51
12	77.97 ± 0.48

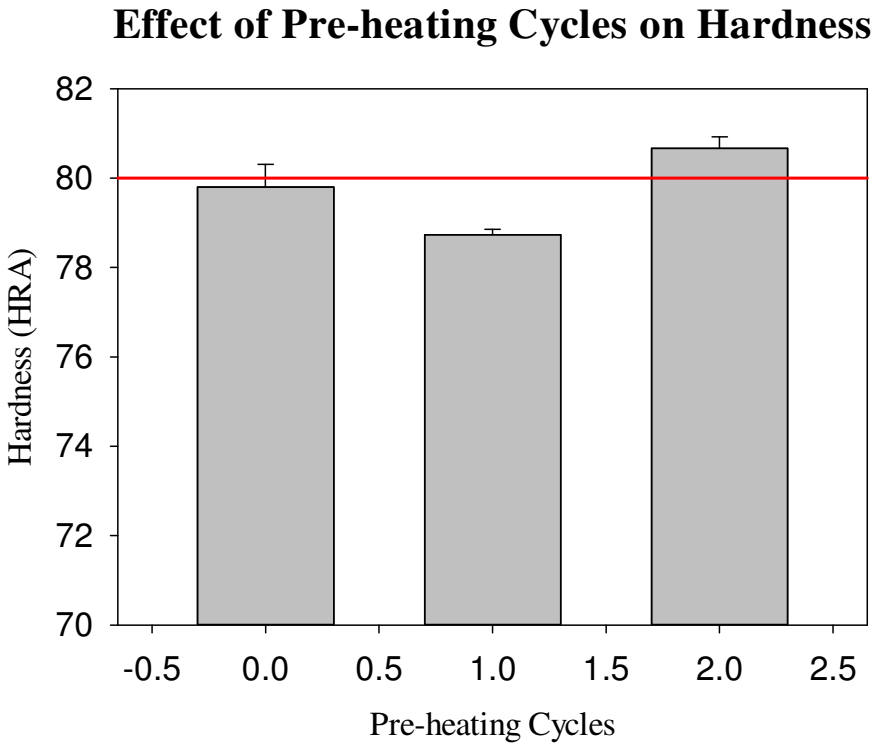

Figure 88 – Effect of pre-heating cycles on coating hardness (HRA) of coatings in the as-sprayed condition (red line indicates the desired target hardness of 80 (HRA)).

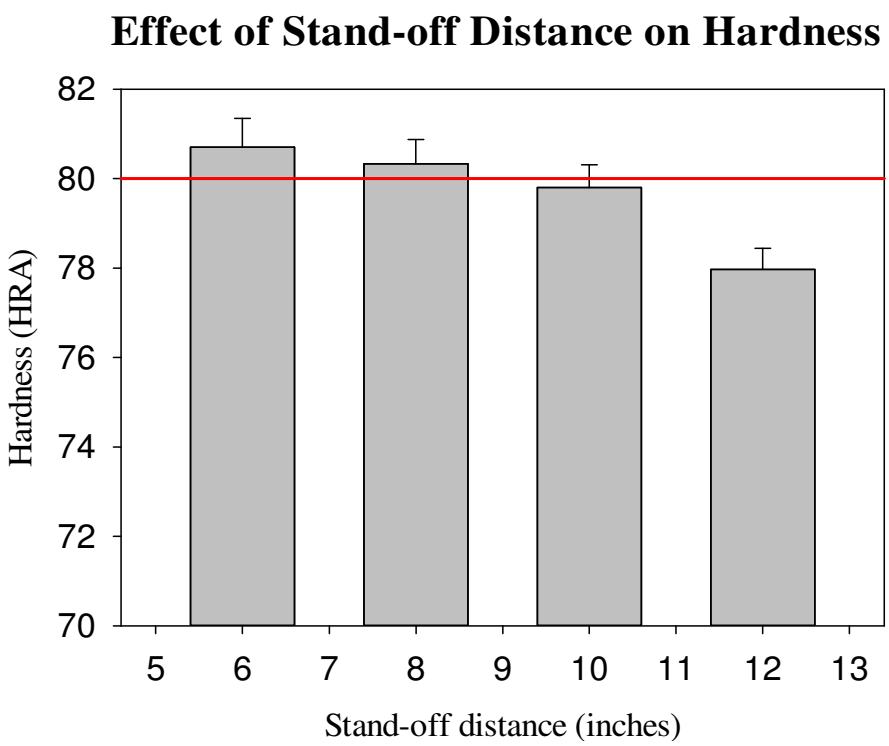

Figure 89 – Effect of stand-off distance on coating hardness (HRA) of coatings in the as-sprayed condition (red line indicates the desired target hardness of 80 (HRA)).

Table 19 – Adhesion results of standard coating, conducted according to ASTM C-633.

Trial	Load (kN)	Stress (MPa)	Failure Type
1	34.71	68.50	Adhesive
2	34.32	67.73	Adhesive
3	34.35	67.79	Adhesive
Average	**34.34**	**67.76**	**Adhesive**
STD	0.02	0.03	N/A

Table 20 - Adhesion results of coatings deposited with one pre-heating cycles, conducted according to ASTM C-633.

Trial	Load (kN)	Stress (MPa)	Failure Type
1	32.67	64.48	Adhesive
2	33.24	65.60	Cohesive
3	34.76	68.60	Adhesive
Average	**34.00**	**67.10**	**Adhesive**
STD	0.76	1.50	N/A

Table 21- Adhesion results of coatings deposited with two pre-heating cycles, conducted according to ASTM C-633.

Trial	Load (kN)	Stress (MPa)	Failure Type
1	28.29	55.83	Cohesive
2	33.27	65.66	Adhesive
3	33.66	66.43	Adhesive
Average	**33.47**	**66.04**	**Adhesive**
STD	0.19	0.38	N/A

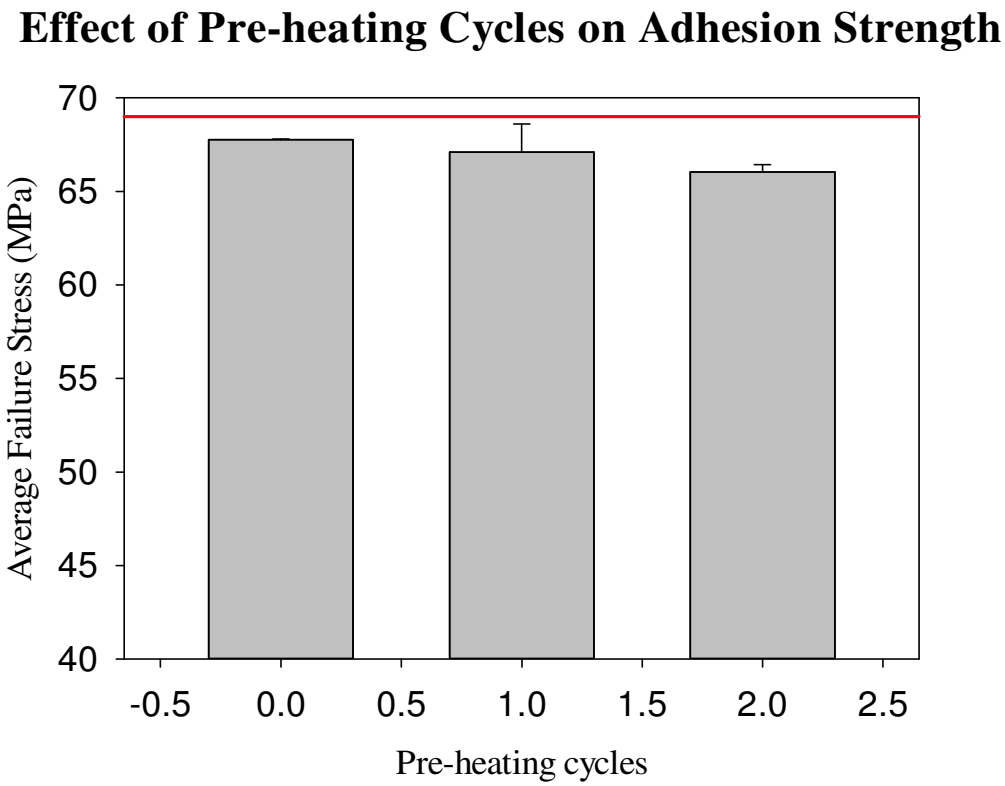

Figure 90 – Effect of pre-heating cycles on adhesion strength, conducted according to ASTM C-633 (red line indicates the desired target strength of 69 Mpa, which is the rated strength of FM 1000 adhesive).

Table 22 - Adhesion results of coatings deposited with a stand-off distance of six inches, conduced according to ASTM C-633.

Trial	Load (kN)	Stress (Mpa)	Failure Type
1	20.76	40.98	Cohesive
2	23.50	46.38	Cohesive
3	20.87	41.20	Cohesive
Average	**22.19**	**43.79**	**Cohesive**
STD	1.31	2.59	N/A

Table 23- Adhesion results of coatings deposited with a stand-off distance of eight inches, conduced according to ASTM C-633.

Trial	Load (kN)	Stress (MPa)	Failure Type
1	34.40	67.90	Adhesive
2	33.01	65.15	Adhesive
3	34.39	67.86	Adhesive
Average	**33.70**	**66.51**	**Adhesive**
STD	0.69	1.35	N/A

Table 24 - Adhesion results of coatings deposited with a stand-off distance of 12 inches, conduced according to ASTM C-633.

Trial	Load (kn)	Stress (MPa)	Failure Type
1	34.46	68.01	Adhesive
2	34.45	67.98	Cohesive
3	33.45	66.01	Adhesive
Average	**33.95**	**67.00**	**Adhesive**
STD	0.50	0.99	N/A

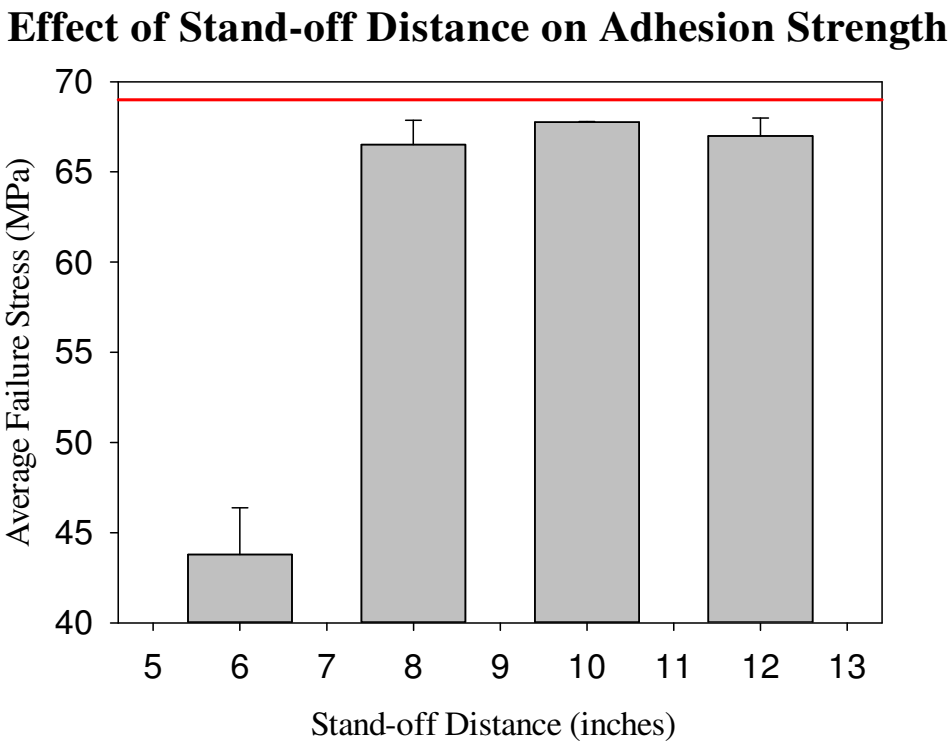

Figure 91 – Effect of stand-off distance on adhesion strength, conducted according to ASTM C-633 (the red line indicates the desired target strength of 69 Mpa, which is the rated strength of FM 1000 adhesive).

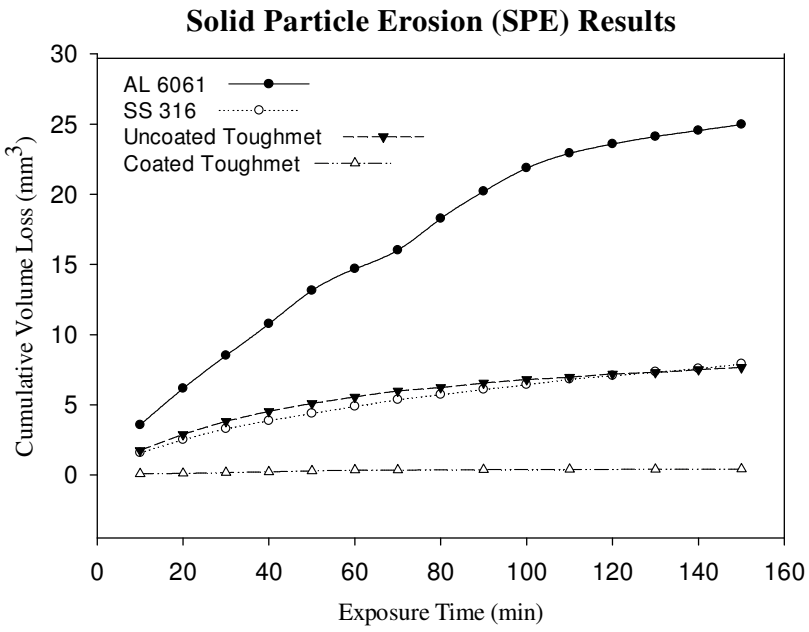

Figure 92 - SPE results of reference materials, uncoated toughmet, and coated toughmet in the as-sprayed condition, for a cumulative test duration of 150 minutes. The reference materials are conducted to calibrate the erosion tester as well as to develop a baseline for comparision between various erosion testers.

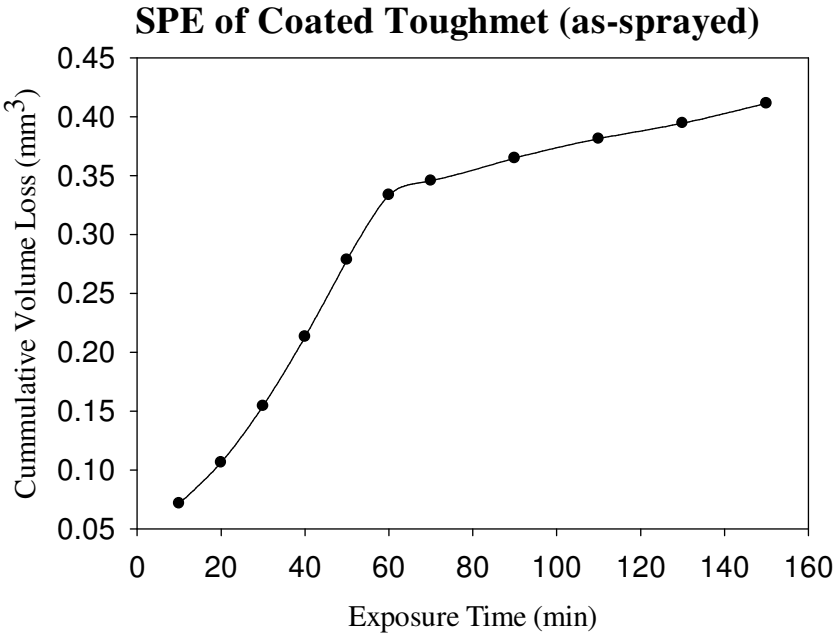

Figure 93 – SPE erosion results of standard coating in the as-sprayed condition, for a cumulative test duration of 150 minutes.

Table 25 – Erosion rates and minimum test duration of reference materials, uncoated toughmet, and coated toughmet in the as-sprayed condition.

Sample	AL 6061	SS 316	Uncoated Toughmet	Standard Coating (as-sprayed)
Maximum Erosion Rate (Q_e) (mm^3/min)	0.2031	0.0698	0.0835	0.0055
Terminal Erosion Rate (Q_{et}) (mm^3/min)	0.0506	0.0309	0.0198	0.0008
Minimum Test Duration (min)	30	40	40	50

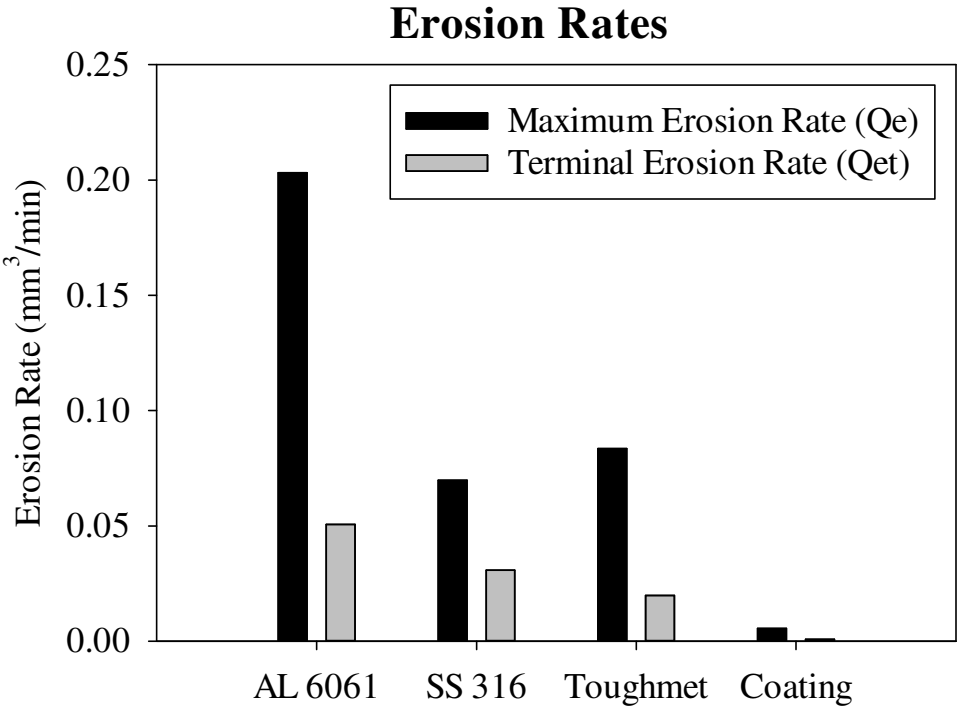

Figure 94 – Maximum erosion and terminal erosion rates of reference materials, uncoated toughmet, and coated toughmet in the as sprayed condition.

Table 26– Resistance to erosion normalized to uncoated toughmet of reference materials, uncoated toughmet, and coated toughmet in the as-sprayed condition.

Sample	AL 6061	SS 316	Uncoated Toughmet	Standard Coating (as-sprayed)
Normalized Maximum Erosion (S_e)	0.4111	1.1962	1	14.9107
Normalized Terminal Erosion (S_{et})	0.3913	0.6408	1	24.7500

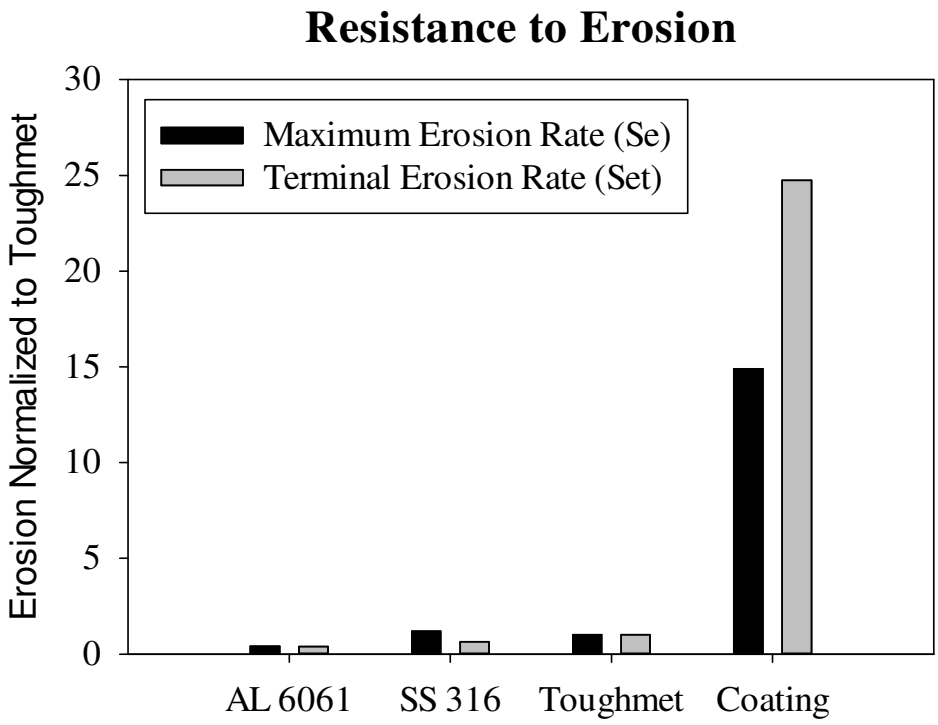

Figure 95– Maximum erosion and terminal erosion rates normalized to toughmet erosion rates of reference materials, uncoated toughmet, and coated toughmet in the as sprayed condition.

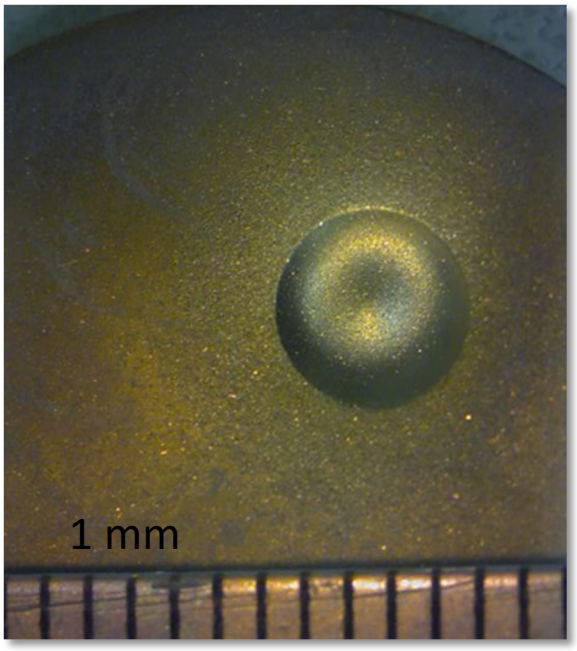

Figure 96 - Stereomicroscope image of uncoated toughmet wear scar after 150 minutes of exposure.

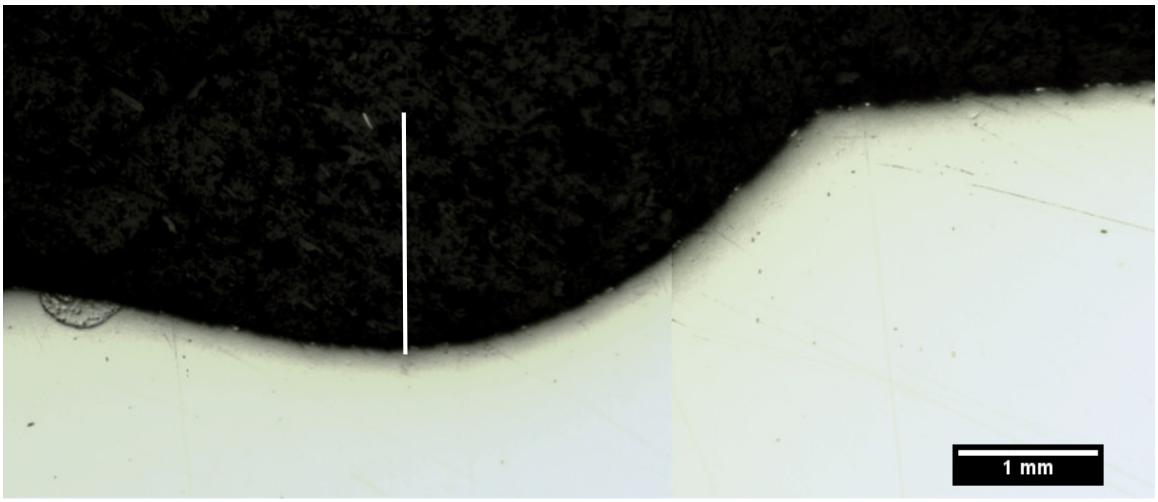

Figure 97 – Cross-section of erosion scar (right half) of uncoated toughmet after 150 minutes of exposure (maximum depth of 1.72 mm as indicated by vertical line).

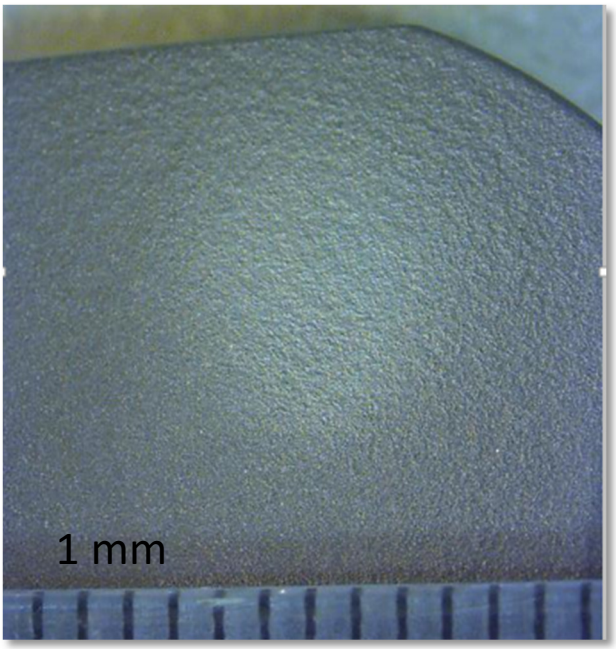

Figure 98- Stereomicroscope image of coated toughmet in the as-sprayed condition of wear scar after 150 minutes of exposure.

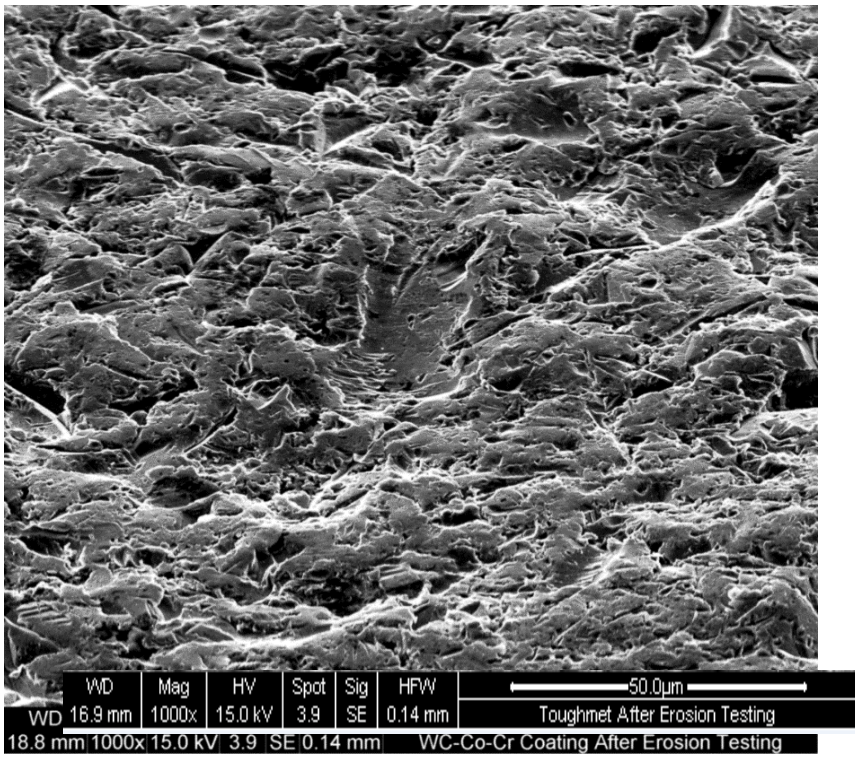

Figure 99 - SEM image of uncoated toughmet erosion scar after 150 minutes of exposure at 1000 X.

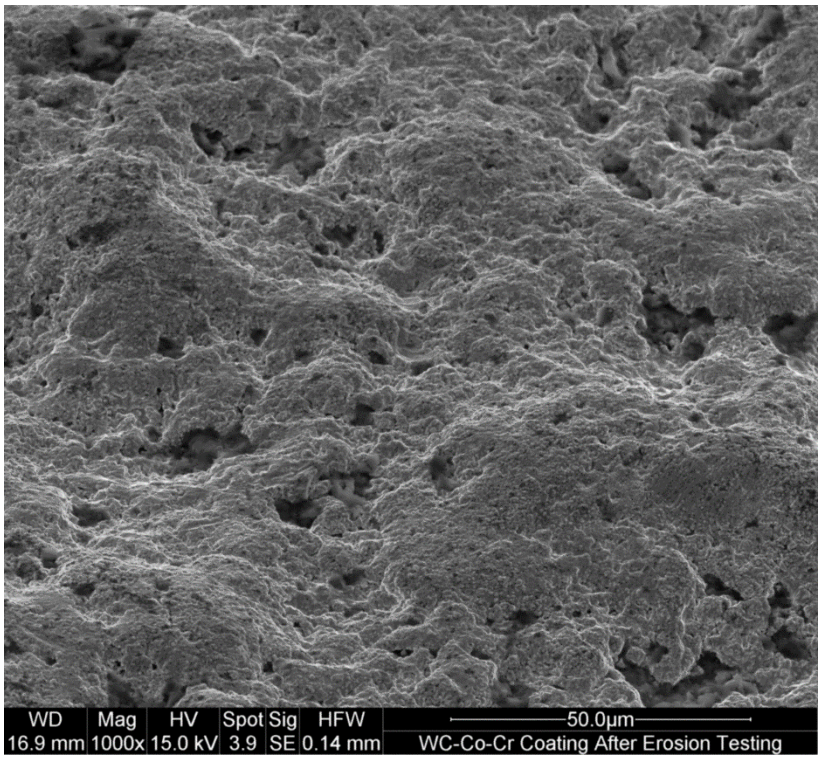

Figure 100 - SEM image of coated toughmet in the as-sprayed condition after 150 minutes of exposure at 1000 X.

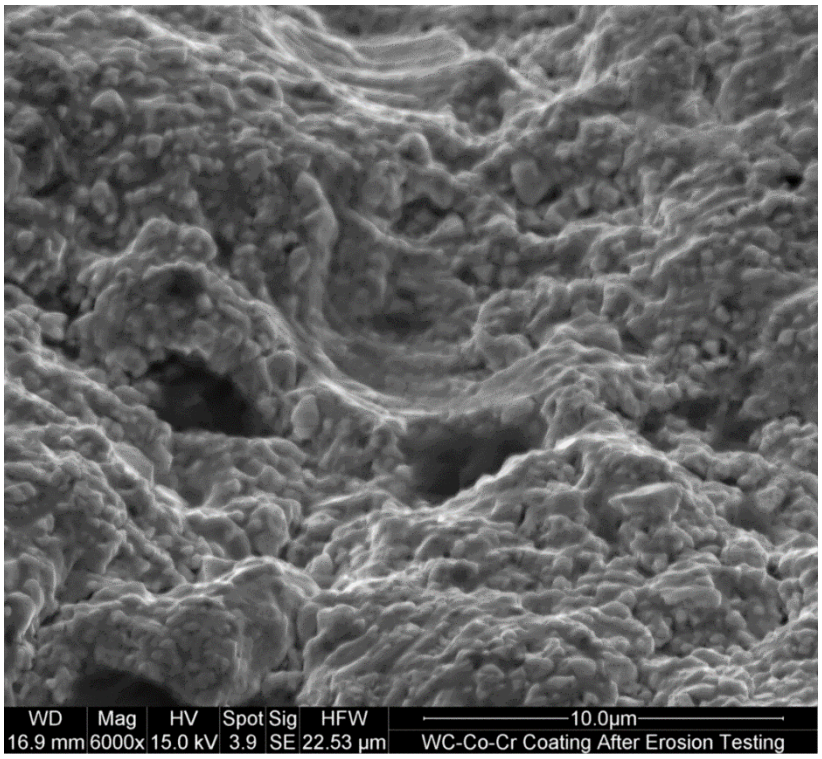

Figure 101 - SEM image of coated toughmet in the as-sprayed condition after 150 minutes of exposure at 6000 X.

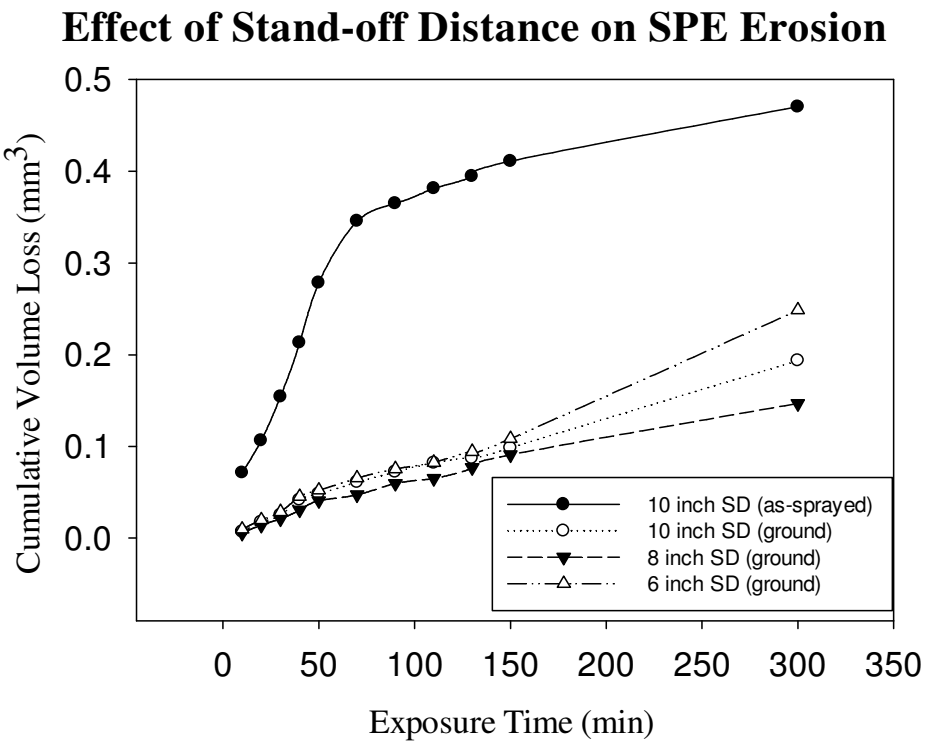

Figure 102 – Effect of stand-off distance on SPE, with a cumulative exposure duration of 300 minutes.

Table 27– Erosion rates and minimum test duration of coatings with modified stand-off distances.

Sample	10” SD (as-sprayed)	10” SD (ground)	8” SD (ground)	6” SD (ground)
Maximum Erosion Rate (Q_e) (mm^3/min)	0.0056	0.0006	0.0005	0.0008
Terminal Erosion Rate (Q_{et}) (mm^3/min)	0.0008	0.0006	0.0005	0.0008
Minimum Test Duration (min)	50	90	90	90

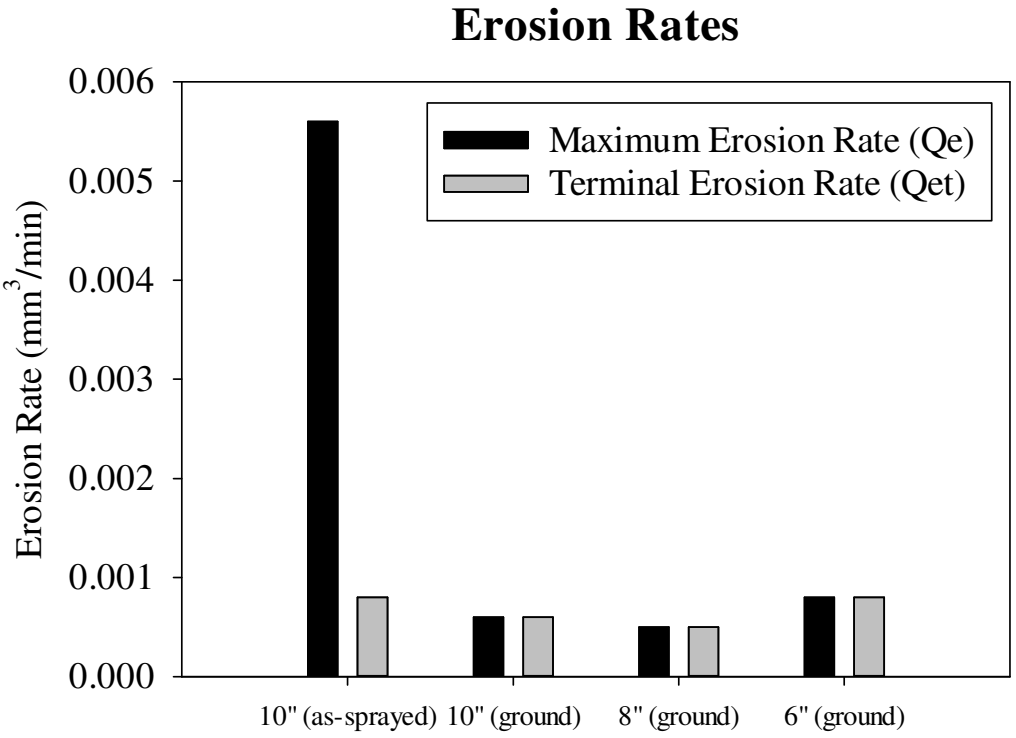

Figure 103 – Maximum erosion and terminal erosion rates of coatings with modified stand-off distance.

Table 28 – Resistance to erosion normalized to uncoated toughmet of coatings with modified stand-off distances.

Sample	10” SD (as-sprayed)	10” SD (ground)	8” SD (ground)	6” SD (ground)
Normalized Maximum Erosion (S_e)	14.9	139.2	167.0	104.4
Normalized Terminal Erosion (S_{et})	24.75	33.0	39.6	24.75

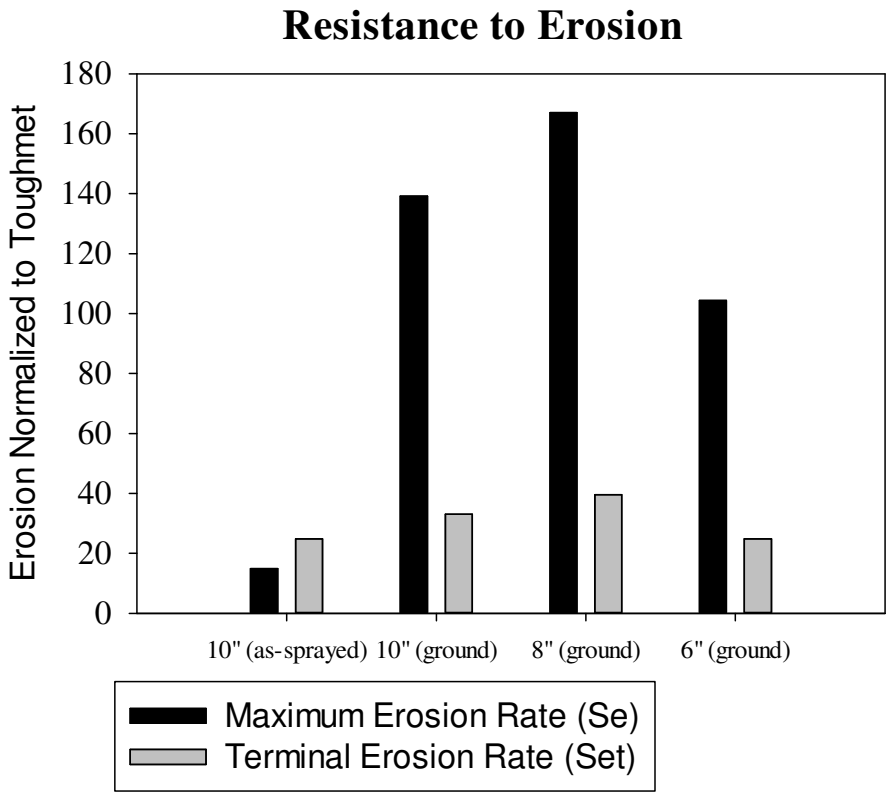

Figure 104– Maximum erosion and terminal erosion rates normalized to toughmet erosion rates of coatings with modified stand-off distances.

Chapter 5: Discussion

The following section discusses the results obtained during this research investigation, which are divided into four sections and presented in the order of completion.

The first section encompasses the results obtained during observation of the feedstock powder used to produce the coating, where the particle morphology, particle composition, and particle size distribution were studied. The second section includes the preliminary characterization of the standard coating and uncoated toughmet to develop the baseline for the deposition parameter optimization process. In the remaining sections, the effect of individual deposition parameters are evaluated relative to previously studied standard coating, in an effort to optimize the coating deposition parameters and thus the coating performance.

5.1 Feedstock Characterization

With the aim of confirming the composition and quality of the feedstock powder, Amperit 558 (WC-Co-Cr) agglomerated sintered feedstock powder produced by H.C. Starck was studied.

The first area of concern when evaluating feedstock powder is particle size range, since a wide size distribution results in uneven in-flight particle temperature and velocity. Thus a uniform particle size is desired to achieve consistent particle splats during coating deposition. From Figure 45, it was determined that approximately 70% of the feedstock particles had a diameter that ranged from 20 to 30 microns, and the sum of all particles had a diameter between 15-50 microns, which can be considered relatively uniform. This

relative uniformity ensures relatively even particle temperature and velocity during deposition, which permits consistent splat morphology and thus uniform coating deposition.

Feedstock composition plays an important role in the microstructure and mechanical properties of the deposited coatings. In WC-Cr-Co TS coatings, the tungsten carbide particles act as the wear resistant component of the coating, the cobalt serves as a binding agent to hold the WC particle in place, and the chromium improves the coating's resistance to corrosion. Therefore the feedstock composition was analyzed by constructing an EDS map of a random distribution of feedstock particles (Figure 47) that was developed from an SEM image (Figure 46) in order to determine the feedstock's elemental composition and distribution. Due to the space between particles, a carbon rich phase that represents the carbon tape used to secure the particle was visible in the EDS map (it appeared as oblong faded yellow regions); this phase was disregarded in the elemental and weight percentage analysis. Additionally, the x-ray emitter and detector were mounted at an angle, thus specific regions of some particle showed no composition due to the particle's spherical morphology.

The detectable X-ray diffractions were used to construct an elemental map of the Amperit 558 feedstock particle, and depict a relatively even distribution of elements across the entire map, as well as within each particle. The weight-based percentage of each element was then determined for each phase and multiplied by the percent of each phase to determine the overall weight percentage of each element (Figure 48). These calculations resulted in the following elemental composition: Tungsten (W) 80.53%, Carbon (C) 5.21%, Cobalt (Co) 7.77 %, Chromium (Cr) 3.34 %, Oxygen (O) 1.65%, and Iron (Fe) 1.47%. This

composition correlates relatively well to powder characteristics provided by the manufacture, except that this analysis resulted in a higher mass fraction of Oxygen (1.45%) and Iron (1.17%).

Furthermore, feedstock particle morphology and composition were studied using SEM and EDS equipment to confirm that a uniform distribution of elements was present within the feedstock particles. The feedstock contained three distinct particle morphologies, represented as a densely packed solid particle, porous solid particle, and porous hollow particle and shown in Figure 49, Figure 51, and Figure 53, respectively. Individual particles were found to have a relatively even distribution of W and Co, and smooth globular deposits of Cr, which was determined by conducting an EDS line scan on a densely packed solid particle, porous solid particle, and porous hollow particle ((Figure 50, Figure 52, and Figure 54). Each of these plots are represented on the corresponding SEM image and indicated by a red line across the particle. The densely packed solid particle contains multiple Cr spikes and small concentrations of Co. The porous solid and porous hollow particle contained Cr concentrations and large W concentrations. Additionally, each of these particles were found to have sharp angular tungsten carbide (WC) particles embedded in smooth deposits of Cr and Co. This confirms that the feedstock elemental composition and morphology are relatively uniform throughout the identified particles, indicating that the coatings deposited with Amperit 558 feedstock powder will exhibit a uniform elemental distribution.

5.2 Characterization of Standard Coating

The performance of the standard coating was evaluated to quantify the mechanical properties of the standard coating relative to the uncoated toughmet. It was also used to

develop a baseline for the microstructural and mechanical properties of the standard coating, which could then be compared to coatings with modified deposition parameters. These properties mainly consist of adhesion strength, porosity, density, hardness, and erosion resistance.

The first step of coating deposition is mechanically roughing of the substrate surface in order to promote coating adhesion by mechanically interlocking the deposited feedstock splats. It is crucial that the roughened surface is sufficiently rough so as to provide adequate interlocking, but not excessively rough to the point that it affects the final coating surface. Therefore, a mechanically roughened coupon and an as-sprayed sample were observed using an optical profilometer, which resulted in an average pre-spray treated roughness of 3.46 ± 0.24 (um) and an average as-sprayed surface roughness of 4.49 ± 0.63 (um; Table 8 and Table 15, respectively). This suggests that the current grit blasting procedure is not severe enough to affect the final surface roughness, which implies that a more aggressive surface roughening procedure could be implemented if necessary.

Additionally, the grit blasted surface contained Aluminum Oxide (Al_2O_3) particles (Figure 60), and particle composition was confirmed via an EDS point scan (Figure 61 and Figure 62). These particles are mechanically interlocked into the coating substrate, which can act as a stress riser at the coating interface, promoting coating delamination. As a result of the current roughening procedure, approximately six percent (by area) of the surface contained embedded blasting media (Figure 59). It is possible that these particles could reduce the adhesion strength of the coating. However, it was determined the adhesion strength of the standard coating was 67.76 ± 0.03 (MPa), where the failures of all trials were due to the adhesive rather than to a cohesive failure within the coatings. The measured

adhesion strength of the standard coating is similar to the rated strength of the FM1000 adhesive when new (69 MPa) [18]. This suggests that although grit blasting media is embedded in the substrate and coating interface, it is not sufficient to degrade the adhesion strength of the coating. Additionally, it should be noted that since no cohesive failure occurred, the true strength of the coating cannot be measured due to current limitations of available adhesives; however, this is considered a satisfactory result for a qualification test, as the strength of the bonding agent is greater than the minimum required adhesion strength [18].

An important aspect of TS coatings is the inflight particle velocity. During coating deposition the feedstock particles are thermally softened and rapidly accelerated towards the work piece, which allows the particles to efficiently flatten upon impact. This phenomenon must be well balanced in order to have adequate thermal softening without particle decarburization, in addition to sufficient particle velocity. When properly balanced, HVOF coatings exhibit minimal coating porosity, which indicates appropriate particle velocity and temperature during coating deposition. In the case of standard coating, the stand-off distance was set to 10 inches, resulting in a coating porosity of 0.423%, calculated from a processed image of the coating cross-section (Figure 71). Additionally, the coating density was measured to confirm the trends observed from the modified deposition parameters with varied coating porosity, where the standard coating density was measured to be 12.783 ± 0.0009 (g/cm^3).

As expected, the addition of the coating resulted in an increase of coating hardness over the uncoated toughmet of 24 %, where the substrate hardness was determined to be 64.33 ± 0.12 (HRA) and the standard coating hardness was 79.8 ± 0.51 (HRA; Table 16).

This is due to the hard WC particles suspended within the Co and Cr matrix, which allows the coating to be relatively hard while remaining ductile to a certain degree. Although WC is extremely hard (approximately 1600 HV) a pure WC coating would not be practical due to its inherent brittleness. Furthermore, the dwell time required for particles to approach 2,870°C (i.e., the melting temperature of WC) is not practical unless the particle diameter is severely reduced or the flame temperature is increased, which therefore increases substrate temperature but also eliminates substrate alloys with low melting temperatures. Therefore the combination of suspended WC particles within a Cr-Co matrix offers a necessary balance between application and hardness.

In order to determine the erosion resistance of uncoated and coated toughmet, solid particle erosion testing was conducted (cumulative exposure duration: 150 minutes) using a recirculating slurry erosion testing rig designed and fabricated specifically for this research project. Erosion testing was conducted on reference materials (Al 6061-T6 and stainless steel 316), uncoated toughmet incrementally polished to 1200 grit, and the standard coating applied to toughmet in the as-received condition. The cumulative volume loss versus exposure time of the tested materials is shown in Figure 92 and Figure 93, where all tested materials exhibited an initial rapid volume loss followed by stabilization into a steady-state volume loss. The reference materials and uncoated toughmet exhibited substantial initial volume loss via type one cutting that was caused by angular suspended particles impacting the sample surface (Figure 99). As testing continues, the type one cutting modifies the wear scar morphology from a circular exposure area into a conical exposure area, increasing the affected surface area and thus causing a reduction of

suspended particle impact density. This trend continues until the wear is fully developed, resulting in a terminal erosion rate.

In comparison, the standard coating displayed similar tendencies, but at a considerably reduced rate, due to the supported WC particles that prevented cutting damage from impacting particles due to their inherent hardness. Under SEM investigation the wear scar did not appear to be damaged, however smoothing of surface asperities is apparent (Figure 100). Upon further investigation, it was determined that the accelerated initial volume loss was due to the removal of surface asperities that de-bonded from the coating surface as entire splats, resulting in smooth conical features located on surface of the coating (Figure 101).

Moreover, erosion testing resulted in a sizable difference in the total volumetric loss after an exposure duration of 150 minutes, such that Al 6061-T6 exhibited the largest volumetric loss of 24.9699 mm^3, stainless steel 316 had a volumetric loss of 7.9191 mm^3, and uncoated toughmet had a total volumetric loss of 7.6602 mm^3. However, the coated toughmet in the as-sprayed condition demonstrated the best erosion resistance compared to the reference materials and the uncoated toughmet, with a total volumetric loss of only 0.4112 mm^3. Due to the minor relative volume loss observed in the as-sprayed coating, an individual graph of this plot was added to clearly represent the coating's behavior during erosion testing (Figure 93). Thus each material demonstrated a specific maximum erosion rate (Qe), terminal erosion rate (Qet), and minimum test duration (MTD), summarized in Table 25. Additionally, the erosion rates were normalized to uncoated toughmet (Table 26) by implementing Equation [7] where uncoated toughmet served as the reference material, which found that the standard coating exhibited a 14.91 fold improvement in Qe over the

uncoated toughmet and a Qet improvement of 24.75. Therefore, the presence of the standard coating resulted in a significant improvement with regards to erosion resistance over toughmet in the uncoated condition.

5.3 Effect of Pre-spray Heating Cycles

During the coating process, molten and or semi-molten particles are rapidly quenched and solidified upon impact with the substrate surface. The large temperature difference between the particles and substrate can cause significant thermal contraction, which can lead to the formation of inter-splat cracks and splat de-bonding.

With the aim of improving the microstructural and mechanical properties of the coating relative to the standard coating, pre-spray heating cycles were conducted, where the torch traversed the coupon surface with the feedstock flow turned off at a stand-off distance of 10 inches. Under these conditions the surface temperature stabilized at approximately 340°F after three complete cycles (Figure 55), indicating that pre-heating cycles in excess of three would have no beneficial effect on reducing the deposited particle temperature quenching rate at a stand-off distance of 10 inches.

The addition of a single pre-heating cycle was found to have a negative effect relative to the standard coating (which had zero pre-heating cycles). The most apparent change was the coating porosity, which spiked from 0.423% to 2.255% upon implementation of a single pre-heating cycle (Figure 76), likely due to insufficient cooling between deposition cycles, resulting in heated particles to be covered by successive deposition cycles, where the particles then contract upon cooling leaving a large network of pores within the coating. The increased porosity impacts various coating properties, such

as adhesion strength, hardness, and density. The embedded pores act as inconsistencies within the coating, which can serve as crack initiation sites during tensile loading, causing a cohesive failure during adhesion testing (Table 20), suggesting the maximum strength of the coating has been reached, unlike the standard coating. During hardness testing the embedded pores can potentially collapse, causing the indenter depth to slightly increase which would yield a comparatively lower hardness, which was the case for the single pre-spray heating cycle (Figure 88). Undoubtedly, an increase in coating porosity would cause a corresponding reduction in coating density (Figure 84), which was measured to confirm the porosity phenomenon.

Upon implementation of two pre-spray heating cycles similar microstructural and mechanical properties were observed, but to a lesser degree. The porosity fell 1.428% (Table 11) from one pre-spray heat treatment to 1.579%, however was still more than 3.5 fold larger than the standard coating. The resulting adhesion strength of the coating was comparable to that of one pre-heating cycle; however a single cohesive failure occurred once again (Table 21). This suggests the coating porosity has a significant impact on coating adhesion strength, where porosity in excess of 1.5% results in an approximate adhesion strength of 67 MPa and one of three failure occurring cohesively. Peculiarly, the coating hardness did not diminish as it had under previous conditions (Figure 88); the reduced porosity and increased temperature likely slightly increased the carbide content of the amorphous Co binder phase. As anticipated, the resulting porosity resulted in an increase in coating density to 12.66 (g/cm^3; Figure 84), behaving inversely to the coating porosity trend.

Ultimately, the enormous increase in coating porosity alone was sufficient to disqualify the coating from additional testing. Therefore, coatings deposited with pre-spray heating cycles were not selected for solid particle erosion testing.

5.4 Effect of Stand-off Distance

A modified stand-off distance was utilized to improve the microstructural and mechanical properties of the standard coating. The stand-off distance was altered in two inch increments from the standard (10”), resulting in stand-off distances of 12, 10, eight, and six inches. As the stand-off distance increases the particle dwell time increases, resulting in an increased inflight particle temperature. However this can also lead to reduced particle velocity, once the terminal velocity has been achieved. Alternatively, reducing the stand-off distance reduces the particle dwell time and thus the in-flight particle temperature. Therefore, an optimal stand-off distance exists for each individual feedstock powder; the point at which sufficient thermal softening occurs for particles that have an appropriate in-flight velocity upon impact in order to effectively mechanically interlock with the substrate and previously deposited splats.

During coating deposition it was determined the substrate surface temperature differed considerably by the stand-off distance, such that the temperature continually increased as the stand-off distance decreased (Figure 56). This increased temperature essentially heat- treated the previously deposited feedstock particles to produce a consistent decrease in coating hardness as the stand-off distance increased (Figure 89).

After increasing the stand-off distance to 12 inches, the coating porosity once again spiked above that of the standard coating (1.212%; Figure 83). This was confirmed by

calculating the coating density (Figure 85). It was caused by reduced particle velocity, which resulted in insufficient splat flattening and thus poor mechanical interlocking upon impact. Moreover, this spike in porosity initiated a cohesive failure during adhesion testing (Table 24), confirming that excessive porosity results in diminished adhesion strength (i.e., as identified when pre-heating cycles were implemented). Due to this excessive porosity, coatings with a stand-off distance of 12 inches were not selected for erosion resistance testing.

At the opposite end of the spectrum, a stand-off distance of six inches also resulted in an increase in coating porosity relative to the standard coating (0.716%). The decreased particle dwell time likely did not allow for the sufficient thermal softening that is required for effective splat flattening, thereby causing the majority of the porosity to develop near the coating and substrate interface. As deposition cycles progressed, the increased temperature due to the proximity of the torch flame counteracted this phenomenon, resulting in a denser coating near the surface (Figure 81). Moreover, as elaborated on in literature, as the particles impact previously deposited splats the particles encounter a harder surface relative to the substrate, which does not allow particle penetrating and thus causes the particles to effectively flatten, thus increasing the coating density as the deposition cycles increases [33].

Ultimately, the extensive network of pores near the substrate and coating interface caused insufficient mechanical interlocking, which diminished the coating adhesion strength and resulted in three cohesive failures that occurred at an average failure stress of 43.79 ± 2.59 (MPa; Table 22).

Finally, the stand-off distance of eight inches exhibited the first documented improvement in coating porosity within this research, to a mere 0.334%. This was due to the balance of particle thermal softening and in-flight particle velocity (Figure 83), and was once again confirmed via coating density, which resulted in the highest observed density coating of all stand-off distances (12.827 ± 0.004 [g/cm^3]; Figure 85). Moreover, the coating adhesion strength at a stand-off distance of eight inches was determined to be similar to the standard coating, with an average coating adhesion strength of 66.51 ± 1.35 (MPa), where all failure occurred adhesively (Table 23). Therefore, upon preliminary observation a stand-off distance of eight inches resulted in similar adhesion strength to the standard coating, a reduction in coating porosity of 0.089%, and an increase in coating hardness of 0.53 (HRA) relative to the standard coating.

The effect of stand-off distance on erosion resistance was evaluated for coatings with stand-off distances of 10 , eight, and six inches due to their inherent porosity, using the recirculating solid particle erosion testing rig that was fabricated for this research. To confirm that the removal of surface asperities resulted in an initial spike in volume loss, the samples were tested in the ground condition and compared to the as-sprayed condition under identical erosion conditions. Additionally, due to the superior erosion resistance of the coating, the test duration was extended to 300 minutes in order to confirm the terminal erosion rate. After the reduction of surface roughness via planer surface grinding, the coatings did not exhibit substantial initial volume loss, but instead demonstrated a linear terminal erosion rate throughout the duration of erosion testing (Figure 102). This resulted in a total volumetric loss of 0.4705 mm^3 after 300 minutes of exposure for the standard coating in the as-sprayed condition, and a total volumetric loss of 0.1938 mm^3 when the

identical coating was tested in the ground condition. The total volumetric loss decreased to 0.1468 mm^3 when the stand-off distance was decreased to eight inches. The increase in erosion resistance is likely due to improved splat cohesion and better mechanical interlocking, as suggested by the reduction in coating porosity. This trend was not continued when the stand-off distance was further decreased to six inches, which resulted in a total volumetric loss of 0.2488 mm^3; this increase in total volumetric loss was due to the reduction of splat cohesion, as confirmed by the cohesive failures that occurred during adhesion testing as well as the increased coating porosity. Therefore, the maximum erosion rate was reduced 9.33 fold when surface asperities were removed prior to SPE erosion testing, while the terminal erosion rate was only reduced by 33% in the case of the standard coating (Figure 103).

Finally, the maximum and terminal erosion rates were normalized to the uncoated toughmet using Equation [7], where uncoated toughmet was taken as the reference. This allowed the improvement in erosion resistance of the coating to be quantified relative to the substrate (for summaries please see Table 28, for representation please see Figure 104), and demonstrated that the improved splat cohesion due to the reduction of stand-of distance (eight inches) resulted in an improvement in maximum erosion resistance of 167.2 fold and increase of terminal erosion resistance of 39.6 times, relative to the uncoated toughmet.

In summary, the stand-off distance significantly affects the microstructural and mechanical properties of HVOF TS coatings, where an optimal stand-off distance of eight inches was determined when Amperit 558 feedstock powder was utilized.

Chapter 6: Conclusions

This chapter is a concise restatement of the significant conclusions resulting from this research, as well as recommendations for future work which could further benefit Sharkskin's coating performance.

- Implementation of the HVOF TS coating using the standard depositions parameters resulted in significant improvements in mechanical properties, such as a 24% increase in hardness and 14.91 (maximum) and 24.75 (terminal) fold improvement in erosion resistance relative to the substrate in the uncoated condition.
- Modifying the substrate temperature prior to coating deposition by implementing pre-spray heating cycles resulted in a marginal improvement on coating hardness (two pre-spray heating cycles), and similar adhesion strength values with cohesive failures. Moreover, the coating porosity was substantially increased while the coating density was diminished when pre-spray heating cycles were implemented. Therefore it was determined that the effect of pre-spray heating cycles had a negative effect on the microstructural and mechanical properties of the coating relative to the coating deposited using zero pre-spray heating cycles.
- The coating porosity had a significant impact on coating adhesion strength, where porosity in excess of 1.2 % resulted in an approximate adhesion strength of 67 MPa with one of three failures occurring cohesively.
- Modifying the stand-off distance had a significant impact on the microstructural and mechanical properties of the tested coating, where a stand-off distance of 12 inches was determined to have insufficient particle velocity to effectively flatten

particle splats resulting in undesirable coating porosity. Additionally, a stand-of distance of six inches did not provide a sufficient dwell time to achieve suitable thermal softening required for mechanical interlocking, which resulted in increased coating porosity and cohesive failure during adhesion testing.

- An optimized stand-off distance of eight inches was achieved stemming similar adhesion strength, an increase in hardness of 0.53 (HRA), a reduction of coating porosity of 0.089%, and a reduction in volumetric loss of 75.7% after 300 minutes of SPE exposure.

Chapter 7: Recommendations

While it is evident this study obtained the goal of characterizing the standard coating and optimizing the deposition parameters to improve the microstructural and mechanical properties of the HVOF coating, opportunities for future work still exist. Therefore the following recommendations are made for the continuation of HVOF TS coating optimization research.

- Characterization of remaining feedstock powders currently being deposited at Sharkskin's facility.
- Implementation of a high pressure water-jet system to induce surface roughening without residual particle embedment and investigation of adhesion strength upon implementation of the process.
- Investigation on the effect of substrate alloy on adhesion strength to determine the possible substrates SharkSkin can deposit their coatings onto effectively.
- Further investigation of deposition parameter optimization, to further improve the coatings microstructural and mechanical properties.
- Investigation of coating fracture toughness of coatings with modified stand-off distance by way of the wedge test.
- Investigation of polarization curves measurements of uncoated and coated toughmet obtained from polarization corrosion testing.
- Additional erosion trials with exaggerated exposure durations to fully penetrate the deposited coating.

References

[1] M. Oksa, E. Turunen, T. Suhonen, T. Varis, and S.-P. Hannula, "Optimization and Characterization of High Velocity Oxy-fuel Sprayed Coatings: Techniques, Materials, and Applications," *Coatings*, vol. 1, no. 2, pp. 17–52, Sep. 2011.

[2] P. Suegama, C. . Fugivara, A. . Benedetti, J. . Guilemany, J. Fernández, and J. Delgado, "The influence of gun transverse speed on electrochemical behaviour of thermally sprayed Cr3C2–NiCr coatings in 0.5 M H2SO4 solution," *Electrochim. Acta*, vol. 49, no. 4, pp. 627–634, Feb. 2004.

[3] R. Wood, "Tribology of thermal sprayed WC–Co coatings," *Int. J. Refract. Met. Hard Mater.*, vol. 28, no. 1, pp. 82–94, Jan. 2010.

[4] W. Lih, S. Yang, C. Su, S. Huang, I. Hsu, and M. . Leu, "Effects of process parameters on molten particle speed and surface temperature and the properties of HVOF CrC/NiCr coatings," *Surf. Coatings Technol.*, vol. 133–134, pp. 54–60, Nov. 2000.

[5] W. Raymond and J. Ratka, "Copper Spinodal Alloys," *Adv. Mater. Process.*

[6] H. Lovelock, "Powder/Processing/Structure Relationships in WC-Co Thermal Spray Coatings : A Review of the Published Literature," *ASM Int.*, vol. 7, no. September, pp. 357–373, 1998.

[7] H. Exner, "Physical and chemical nature of cemented carbides," *Int. Met. Rev.*, vol. 24, no. 4, pp. 149–173, 1979.

[8] W. Jarosinski, "Characterization of Tungsten Carbide Cobalt Powders and HVOF Coatings, Thermal Spray: Research, Design, and Applications," *ASM Int.*, pp. 153–157, 1993.

[9] S. Rangaswamy, "Metallurgical Characterization of WC-Co Coatings, Advances in Thermal Spraying," *Pergamon Press*, pp. 101–110, 1986.

[10] M. Dorfman, "A Technical Assessment of High Velocity Oxygen-Fuel versus High Energy Plasma Tungsten Carbide-Cobalt Coatings for Wear Resistance," *Weld. Inst.*, pp. 108.1–102.12, 1989.

[11] D. Crawmer and J. Krebsbach, "Coating Development for HVOF Process Using Design of Experiments, Thermal Spray: In- ternational Advances in Coatings Technology," *ASM Int.*, pp. 127–136, 1992.

[12] L. Chang, A. Ohmori, and Y. Harada, "Effect of powder structure on the structure of thermally sprayed WC-Co coatings," *J. Mater. Sci.*, vol. 31, no. 3, pp. 785–794, 1996.

[13] Y. Qiao, Y. Liu, and T. E. Fischer, “Sliding and Abrasive Wear Resistance of Thermal-Sprayed WC-CO Coatings,” *ASM Int.*, vol. 10, no. March 2001, pp. 118–125, 2004.

[14] P. Fauchais, G. Montavon, and G. Bertrand, “From Powders to Thermally Sprayed Coatings,” *J. Therm. Spray Technol.*, vol. 19, no. 1–2, pp. 56–80, Dec. 2009.

[15] E. Lugscheider, C. Herbst, and L. Zhao, “Parameter studies on high-velocity oxy-fuel spraying of MCrAlY coatings,” *Surf. Coatings Technol.*, vol. 108–109, pp. 16–23, Oct. 1998.

[16] R. Paredes, S. Amico, and A. D’Oliveira, “The effect of roughness and pre-heating of the substrate on the morphology of aluminium coatings deposited by thermal spraying,” *Surf. Coatings Technol.*, vol. 200, no. 9, pp. 3049–3055, Feb. 2006.

[17] Y. Wang, C. Li, and A. Ohmori, “Influence of substrate roughness on the bonding mechanisms of high velocity oxy-fuel sprayed coatings,” *Thin Solid Films*, vol. 485, no. 1–2, pp. 141–147, Aug. 2005.

[18] ASTM, “ASTM - C633 - 13 Standard Test Method for Adhesion or Cohesion Strength of Thermal Spray Coatings,” 2014.

[19] J. Knapp and T. Taylor, “Waterjet roughened surface analysis and bond strength,” *Surf. Coatings Technol.*, vol. 86–87, pp. 22–27, Dec. 1996.

[20] L. Pawlowski, *The Science and Engineering of Thermal Spray Coatings*, Second. West Sussex, England: Wiley, 2008.

[21] J. Picas, M. Punset, M. Baile, E. Martín, and A. Forn, “Effect of oxygen/fuel ratio on the in-flight particle parameters and properties of HVOF WC-CoCr coatings,” *Surf. Coatings Technol.*, vol. 205, pp. S364–S368, Jul. 2011.

[22] E. Turunen, T. Varis, S. Hannula, A. Vaidya, A. Kulkarni, J. Gutleber, S. Sampath, and H. Herman, “On the role of particle state and deposition procedure on mechanical, tribological and dielectric response of high velocity oxy-fuel sprayed alumina coatings,” *Mater. Sci. Eng. A*, vol. 415, no. 1–2, pp. 1–11, Jan. 2006.

[23] J. Guilemany, J. Paco, J. Nutting, and J. Miguel, “Characterization of the W2C Phase Formed during the High Velocity Oxygen Fuel Spraying of a WC 12 Pct Co Powder,” *Metall. Mater. Trans.*, vol. 30, no. August, pp. 1–9, 1999.

[24] M. Rayes, H. Abdo, and K. Khalil, “Erosion - Corrosion of Cermet Coating,” *Int. J. Electrochem. Sci.*, vol. 8, pp. 1117–1137, 2013.

[25] S. Sampath, V. Srinivasan, A. Valarezo, A. Vaidya, and T. Streibl, “Sensing, Control, and In Situ Measurement of Coating Properties: An Integrated Approach

Toward Establishing Process-Property Correlations," vol. 18, no. June, pp. 243–255, 2009.

[26] W. Zhang and S. Sampath, "A Universal Method for Representation of In-Flight Particle Characteristics in Thermal Spray Processes," *J. Therm. Spray Technol.*, vol. 18, no. 1, pp. 23–34, Oct. 2008.

[27] R. Neiser, M. Smith, and R. Dykhuizen, "Oxidation in Wire HVOF Sprayed Steel," *J. Therm. Spray Technol.*, vol. 7, no. 4, pp. 537–545, Dec. 1998.

[28] C. Li and W. Li, "Effect of sprayed powder particle size on the oxidation behavior of MCrAlY materials during high velocity oxygen-fuel deposition," *Surf. Coatings Technol.*, vol. 162, pp. 31–41, 2002.

[29] H. Xiong, L. Zheng, L. Li, and A. Vaidya, "Melting and oxidation behavior of in-flight particles in plasma spray process," *Int. J. Heat Mass Transf.*, vol. 48, no. 25–26, pp. 5121–5133, Dec. 2005.

[30] M. Planche, B. Normand, H. Liao, G. Rannou, and C. Coddet, "Influence of HVOF spraying parameters on in-flight characteristics of Inconel 718 particles and correlation with the electrochemical behaviour of the coating," *Surf. Coatings Technol.*, vol. 157, no. 2–3, pp. 247–256, Aug. 2002.

[31] A. Valarezo, W. Choi, W. Chi, A. Gouldstone, and S. Sampath, "Process Control and Characterization of NiCr Coatings by HVOF-DJ2700 System: A Process Map Approach," *J. Therm. Spray Technol.*, vol. 19, no. 5, pp. 852–865, Apr. 2010.

[32] J. Stokes and L. Looney, "Residual stress in HVOF thermally sprayed thick deposits," *Surf. Coatings Technol.*, vol. 177–178, pp. 18–23, Jan. 2004.

[33] G. Bolelli, L. Lusvarghi, and M. Barletta, "HVOF-sprayed WC–CoCr coatings on Al alloy: Effect of the coating thickness on the tribological properties," *Wear*, vol. 267, no. 5–8, pp. 944–953, Jun. 2009.

[34] D. Stewart, P. Shipway, and D. McCartney, "Influence of heat treatment on the abrasive wear behaviour of HVOF sprayed WC–Co coatings," *Surf. Coatings Technol.*, vol. 105, no. 1–2, pp. 13–24, Jun. 1998.

[35] J. Nerz, B. Kushner, and A. Rotolico, "Microstructural Evaluation of Tungsten Carbide-Cobalt Coatings," *Therm. Spray Technol.*, vol. 1, no. March, pp. 155–160, 1992.

[36] S. Khameneh and M. Sohi, "Effect of heat treatment on wear behavior of HVOF thermally sprayed WC-Co coatings," *Wear*, vol. 260, no. 11–12, pp. 1203–1208, Jun. 2006.

[37] B. Mann and V. Arya, “Abrasive and erosive wear characteristics of plasma nitriding and HVOF coatings: their application in hydro turbines,” *Wear*, vol. 249, no. 5–6, pp. 354–360, Jun. 2001.

[38] T. Kosel, “Solid Particle Erosion,” *ASM Handbook, Frict. Lubr. Wear Technol.*, vol. 18, pp. 199–213, 1992.

[39] I. M. Hutchings, “Wear by Hard Particles,” in *Tribology: friction and wear of engineering materials*, 1992.

[40] J. Hansen, “Relative Erosion Resistance of Several Materials,” *Erosion, Prev. Useful Appl. A Symp.*, pp. 148–162, 1979.

[41] A. Karimi, “Microstructure and hydroabrasive wear behaviour of high velocity oxy-fuel thermally sprayed WC-Co(Cr) coatings,” *Surf. Coatings Technol.*, vol. 57, no. 1, pp. 81–89, 1993.

[42] J. Murthy, “Effect of Grinding on the Erosion Behaviour of a WC–Co–Cr Coating Deposited by HVOF and Detonation Gun Spray Processes,” *Wear*, vol. 249, pp. 592–600, 2001.

[43] D. Stewart, P. Shipway, and D. McCartney, “Microstructural evolution in thermally sprayed WC–Co coatings: comparison between nanocomposite and conventional starting powders,” *Acta Mater.*, vol. 48, no. 7, pp. 1593–1604, Apr. 2000.

[44] A. Sian Ming Ang and C. Berndt, “A review of testing methods for thermal spray coatings,” *Int. Mater. Rev.*, vol. 59, no. 4, pp. 179–223, 2014.

[45] C. Cheatham and S. Symong, “Effect of Magnetic Interference on Directional Surveys in Horizontal Wells,” *Soc. Pet. Eng.*, pp. 101–111, 1992.

[46] M. Sayyadnejad, H. Ghaffarian, and M. Saeidi, “Removal of hydrogen sulfide by zinc oxide nanoparticles in drilling fluid,” *Int. J. Environ. Sci. Technol.*, vol. 5, no. 4, pp. 565–569, 2008.

[47] ASTM, “ASTM E18 - Standard Test Methods for Rockwell Hardness of Metallic Materials,” 2013.

[48] ASTM, “ASTM G73 - Standard Test Method for Liquid Impingement Erosion Using Rotating Apparatus,” 2012.

[49] ASTM, “ASTM G76 - Standard Test Method for Conducting Erosion Tests by Solid Particle Impingement Using Gas Jets,” 2012.

[50] R. Juan, R. Laguna-Camacho, M. Vite-Torres, E. Gallardo-Hernandez, and E. Vero-Cardenas, “Solid Particle Erosion on Different Metallic Materials,” pp. 63–78, 2013.

[51] C. Hector and K. Wong, “Impact angle, particle energy and mass loss in erosion by dilute slurries,” vol. 186187, pp. 454–464, 1995.

[52] H. Grewal, A. Agrawal, and H. Singh, “Design and Development of High-Velocity Slurry Erosion Test Rig Using CFD,” *J. Mater. Eng. Perform.*, vol. 22, no. 1, pp. 152–161, Apr. 2012.

[53] “Engineered Performance Coatings.” [Online]. Available: http://www.ep-coatings.co.uk/processes/hvof/. [Accessed: 10-Jan-2014].

[54] W. Fang, T. Cho, J. Yoon, K. Song, S. Hur, S. Youn, and H. Chun, “Processing optimization, surface properties and wear behavior of HVOF spraying WC–CrC–Ni coating,” *J. Mater. Process. Technol.*, vol. 209, no. 7, pp. 3561–3567, Apr. 2009.

[55] R. Wood, “The sand erosion performance of coatings,” *Mater. Des.*, vol. 20, pp. 179–191, 1999.

[56] F. Marcancola and T. Pontes, “Harsh Downhole Conditions Drive Testing Tool Inovations,” in *Offshore West Africa Conference*, 2013, pp. 1–13.

[57] ASTM, “ASTM E-2109 Standard Test Methods for Determining Area Percentage Porosity in Thermal Sprayed Coatings,” 2014.

[58] ASTM, “ASTM B962-15 Standard Test Methods for Density of Compacted or Sintered Powder Metallurgy (PM) Products Using Archimedes’ Principle,” 2015.

[59] ASTM, “ASTM E1920 - Standard Guide for Metallographic Preparation of Thermal Sprayed Coatings,” 2014.

[60] D. Sheffer, “SharkSkin Coatings and Surface Techniques,” 2013. [Online]. Available: http://sharkcoatings.com. [Accessed: 16-Jun-2015].

Appendix: Recirculating SPE Machine Operating Manual

Machine Limitations and Adjustments

Pump: dual diaphragm pneumatic pump

- Capable of pumping slurry with solid particles up to 1/16”
- Maximum air supply pressure of 90 (psi)
- Maximum slurry reservoir volume of 20 (L)

Nozzle assembly:

- Capable of accepting any standard nozzle with ½” male pipe thread
- Capable of adjusting the stand-off distance from 1” to 1 ½”, by adjusting nozzle assembly mounting bolts

Slurry Operating Pressure: adjustment

- Modifying the pump air supply, by adjusting the regulator.
- Modifying the position of the bypass valve.
- Changing the nozzle orifice diameter.

Erosion Tester Design Considerations

ASTM G73 [48] & G76 [49] were used as a general guide for erosion testing and data acquisition, some of the design considerations are as follows.

- Acceleration to orifice diameter should be greater or equal to 25:1

- Erosion of the nozzle during service shall be monitored and shall not exceed 10% increase from the initial diameter
- Abrasive particles should have angular morphology and be discarded after each trial
- The test time shall be 10 minutes to achieve steady state conditions
- The test temperature shall be normal ambient value (typically between 18°C – 25°C)
- Three samples will be tested for each material
- Each sample will be cleaned and weighed initially and after each successive SPE exposure

General Operating Procedure

Note: Prior to conducting any tests the erosion tester should be thoroughly purged of any residual contaminants via flushing the system with water.

1. Remove nozzles from nozzle assembly (Figure 1)

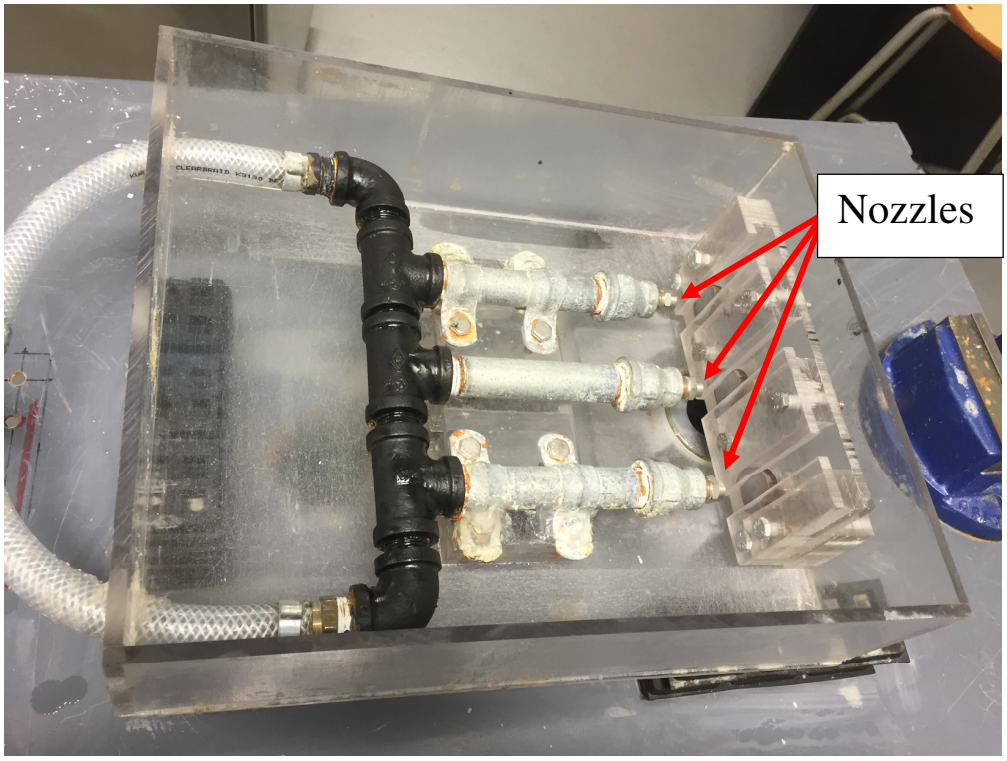

Figure 1 – Nozzle assembly.

2. Close air valve to ensure the pump does not operate when the air supply line is connected (Figure 2).
3. Connect air supply line to compressed air supply line in the lab (Figure 2).

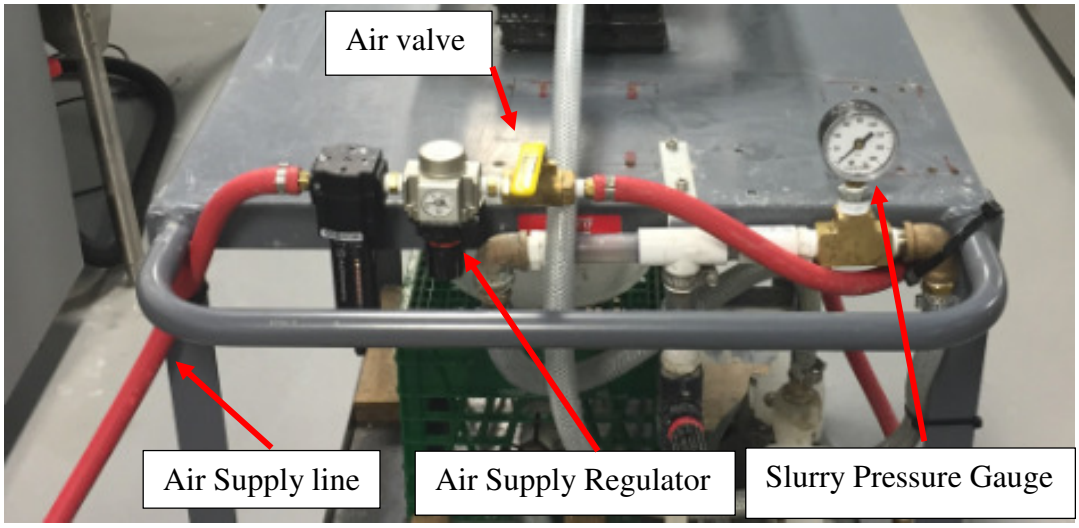

Figure 2 – Pumping assembly.

4. Adjust air supply regulator to approximatly 10 (psi) (Figure 2).
5. Add tap water to nozzle assembly reseviour (Figure 1), until slurry reseeviour is almost full (located directly below nozzle assembly reseviour).
6. Open air supply vlave and allow water to flush the system for approximatly five minutes.
7. Close air valve and remove pump oulet line by loosening hose clamp.
8. Add spare line (located in the cabinet two) to pump exhaust, tighten hose clamp, and place other end of line into lab sink.
9. Open air vlave and pump water into the sink until slurry reserviour is empty, then close air valve and reattatch original pump outlet line.

Note: now that the erosion tester is purged, you are ready to begin test setup.

10. Add dessired slurry solution to the desired volume (less than four gallons) and open air valve to circulate slurry, then slowly add erosion particles to nozzle assembly reseviour to throughly mix.
11. While solution is mixing, mount your weighed erosion samples into the sample holder and tighen the set screw located behind each sample (Figure 3).
12. Close air valve and move any residual erosion particles down the nozzle assembly reseviour drain.
13. Reinstall nozzles into nozzle assembly.
14. Install the sample holder infront of the nozzle assembly and gently tighen the four bolts to secure its position.
15. Install lid ontop of nozzle assembly reserviour.

16. Increase air supply pressure to desired pressure by adjusting air supply regulator (**do not exceed 90 (psi)**).

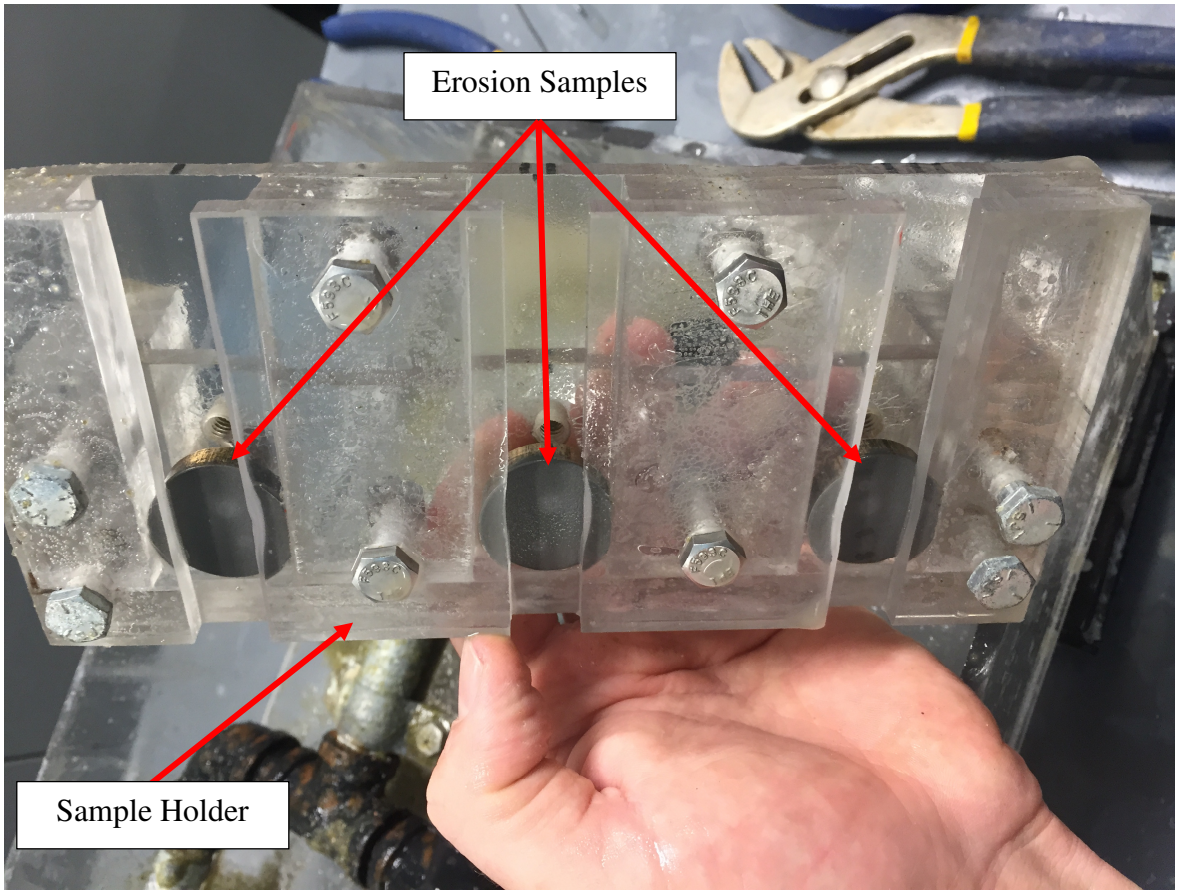

Figure 3 – Sample holder assembly

Note: You are now ready to begin erosion testing.

17. Open air supply valve to begin SPE testing.

Note: During erosion testing the slurry pressure and nozzle outlet should be closely monitored, as erosion particles can periodically clog the nozzle orifice, causing an increase in slurry pressure. Should a nozzle clog close the air valve immediately, remove the lid, remove the clogged nozzle, then remove the clog, reinstall the nozzle/ lid, and continue erosion testing.

18. Upon completion of your desired erosion duration, close the air valve, remove the lid, uninstall the sample holder, and remove the erosion samples for cleaning and weighing.
19. In-between each exposure duration any residual erosion particles should be moved into the drain to ensure complete recirculation upon each exposure duration.
20. Once the samples have been cleaned and weighed, reinstall into the sample holder in the same location and install sample holder onto nozzle assembly reservoir.
21. Install lid and open air valve to begin the next erosion exposure time interval.
22. Repeat this process until the desired exposure duration has been reached.
23. Upon completion of erosion tester the slurry should be immediately removed from the slurry reservoir and the erosion tester should be purged with water to remove and erosion particles from settling within the slurry pumping assembly.

Vita Auctoris

NAME: Chris Imeson

PLACE OF BIRTH: Windsor, Canada

YEAR OF BIRTH: 1990

EDUCATION: University of Windsor, B.Sc., Windsor, ON, 2013